Functional Nanostructured Metal Oxide Hybrid Materials Based on M13 Phages

Von der Fakultät Chemie der Universität Stuttgart
zur Erlangung der Würde eines Doktors der
Naturwissenschaft (Dr. rer. nat.) genehmigte Abhandlung

vorgelegt von

Stefan Kilper

aus Leonberg

Hauptberichter:	Prof. Dr. J. Bill
Mitberichter:	Prof. Dr. S. Schmauder
Prüfungsvorsitzender:	Prof. Dr. P. Fischer

Tag der mündlichen Prüfung: 09.07.2019

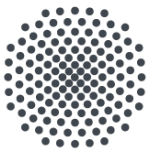

Universität Stuttgart

Institut für Materialwissenschaft der Universität Stuttgart

2019

Contents

Declaration of Authorship / Erklärung über die Eigenständigkeit der Dissertation

Ich versichere, dass ich die vorliegende Arbeit mit dem Titel “Functional Nanostructured Metal Oxide Hybrid Materials Based on M13 Phages” selbständig verfasst und keine anderen als die angegebenen Quellen und Hilfsmittel benutzt habe; aus fremden Quellen entnommene Passagen und Gedanken sind als solche kenntlich gemacht.

Declaration of Authorship

I hereby certify that the dissertation entitled “Functional Nanostructured Metal Oxide Hybrid Materials Based on M13 Phages” is entirely my own work except where otherwise indicated. Passages and ideas from other sources have been clearly indicated.

Name/Name: _____

Unterschrift/Signed: _____

Datum/Date: _____

Publication of the individual chapters in scientific journals

The present thesis has a cumulative structure, this means the chapters are papers which have been published in scientific journals.

Chapter 2: Peptide controlled shaping of biomineralized tin(II) oxide into flower-like particles

Stefan Kilper, Timotheus Jahnke, Katharina Wiegers, Vera Grohe, Zaklina Burghard, Joachim Bill and Dirk Rothenstein, Materials 2019, 12, 904. https://doi.org/10.3390/ma12060904

(S.K. synthesized and characterized the SnO particles. S.K., K.W. and V.G. performed the phage display and binding assay, S.K. and T.J. planned the experiments supervised by D.R., Z.B. and J.B.)

Chapter 3: Macroscopic properties of biomimetic ceramics are governed by the molecular recognition at the bioorganic-inorganic interface

Stefan Kilper, Sandra J. Facey, Zaklina Burghard, Bernhard Hauer, Dirk Rothenstein, and Joachim Bill, Adv. Funct. Mater. 2018, 28, 1705842. https://doi.org/10.1002/adfm.201705842

(S.K. prepared the multilayer assemblies, performed the materials characterization and analyzed and discussed the data supervised by D.R. and J.B., S.J.F performed the genetic modification and preparation of the M13 phages. Z.B. contributed to the data analysis and discussion of the mechanical properties. XRD measurements were performed by Maritta Dudek (Max Planck IS, Stuttgart)

Chapter 4: Genetically Induced In situ-Poling for Piezo-Active Biohybrid Nanowires

Stefan Kilper, Timotheus Jahnke, Marc Aulich, Zaklina Burghard, Dirk Rothenstein, and Joachim Bill, Adv. Mater. 2019, 31, 1805597. https://doi.org/10.1002/adma.201805597

(S.K. prepared the ZnO/M13 hybrid wires, performed the materials characterization and analyzed and discussed the data supervised by D.R. D.R. performed the genetic modification and preparation of M13 phage. M.A. performed the zeta potential measurements and the related data analysis supervised by D.R.. Efi Hadjixenophontos (IMW, University of Stuttgart) prepared the TEM-lamella with FIB. S.K. and T.J. preformed the TEM analysis and discussed in detail the PFM characterization method and data analysis supervised by D.R., Z.B. and J.B.)

Further non-related publications

To complete the publication list these are my further contributions. The publications are not content of this thesis.

- Jahnke, Timotheus; Knoeller, Andrea; Kilper, Stefan; Rothenstein, Dirk; Widenmeyer, Marc; Burghard, Zaklina; Bill, Joachim, Coalescence in Hybrid Materials – The Key to High Capacity Electrodes. ACS Applied Energy Materials 2018.
- Knöller, Andrea; Kilper, Stefan; Diem, Achim M; Widenmeyer, Marc; Runčevski, Tomče; Dinnebier, Robert E; Bill, Joachim; Burghard, Zaklina , Ultrahigh damping capacities in lightweight structural materials, Nano letters,18,4,2519-2524,2018,ACS Publications
- Xiao, Xingxing; Widenmeyer, Marc; Xie, Wenjie; Zou, Tianhua; Yoon, Songhak; Scavini, Marco; Checchia, Stefano; Zhong, Zhicheng; Hansmann, Philipp; Kilper, Stefan; Andrei Kovalevskye and Anke Weidenkaff, Tailoring the structure and thermoelectric properties of $BaTiO_3$ via Eu^{2+} substitution, Physical Chemistry Chemical Physics,19,21,13469-13480,2017, Royal Society of Chemistry
- Moghimian, Pouya; Kilper, Stefan; Srot, Vesna; Rothenstein, Dirk; Facey, Sandra J.; Hauer, Bernhard; Bill, Joachim; van Aken, Peter A., Phage-assisted assembly of organic–inorganic hybrid bilayers, International Journal of Materials Research,107,4,295-299,2016, Carl Hanser Verlag

List of Abbreviations and Symbols

Au	Gold
B_{hkl}	Full width half maximum of the x-ray reflex
BSA	Bovine serum albumin
$CaCO_3$	Calcium carbonate
CBD	Chemical bath deposition
CVD	Chemical vapor deposition
ddH_2O/Milli-Q H_2O	Double-distilled water
D_{hkl}	Average crystallite size determined by x-ray diffraction
DNA	Deoxyribonucleic acid
E. coli	*Escherichia coli* bacteria
E_c	Young's modulus of a thin film
E_s	Young's modulus of the substrate
EtOH	Ethanol
FTIR	Fourier-transform infrared spectroscopy
iPCR	Inverse polymerase chain reaction
Ir	Iridium
K_c	Fracture toughness of a thin film
K_s	Fracture toughness of the substrate
LB medium	Luria-Bertani medium
M13 phage	M13 bacteriophage
MeOH	Methanol
NEB	New England Biolabs
NH_3	Ammonia
NMR	Nuclear magnetic resonance
PD	Phage display
PFM	Piezo force microscopy
PPLN	Periodically poled Lithium niobate
PVD	Physical vapor deposition
PVP	Polyvinylpyrrolidone
SEM	Scanning electron microscope
Si-wafer	Silicon wafer
SnO	Tin(II) oxide
TBST0.1	Tris-buffered saline + 0.1 % Tween-20

TBST0.5	Tris-buffered saline + 0.5 % Tween-20
TEAOH	Tetraethylammonium hydroxide
TEM	Transmission electron microscope
Tris-HCl	Tris-(hydroxymethyl)-aminomethane hydrochloride
V_{ac}	AC electric field
XRD	X-ray diffraction
$ZnAc_2$	Zinc acetate
ZnO	Zinc oxide
θ	Incident angle
λ	Wavelength
$\nu_{c/s}$	Poisson's ratio
ν_{asym}	Asymmetric stretching in infrared spectroscopy
ν_{sym}	Symmetric stretching in infrared spectroscopy
ξ	Degree of unipolarity
Δz_{ω}	First harmonic signal of the vertical piezoelectric response

1 General Introduction

Diverse physicochemical properties such as piezoelectricity, thermoelectricity or electrical conductivity make functional metal oxides highly interesting for applications in modern micro-electronic devices and as host materials for energy storage. However, conventional production processes for such materials are often connected with high energy consumption and the need for elaborated equipment.[1]

Driven by the progressive miniaturization, particularly in semiconductor industry, new materials and approaches for the fabrication of nanostructured electronic and electromechanical components for the integration into smartphones, computers or automotive applications are highly needed. Since 2007, scientists and representatives of the leading semiconductor companies consider in the international technology roadmap for semiconductors the use of biological and bioinspired structures and design principles for pushing the limits of existing semiconductors and microelectronic devises.[1] The perfectly optimized functionality of natural hybrid materials of organic and inorganic phases and its soft synthesis conditions (green synthesis) inspired researchers all over the world. However, biological molecules, for example polysaccharides, peptides or proteins, are still underused as building blocks in modern electronic applications.[1, 2] To exploit the full potential of such natural building blocks for technical applications, detailed investigations to understand biological materials and synthesis strategies are needed. In the last decades, many studies on different biological materials, such as bone and nacre, revealed new and sometimes unexpected properties of these materials.[3] Despite structural and functional differences of biological materials they possess common building principles, such as an organic matrix in which inorganic particles are embedded, nano-sized organic and inorganic building blocks and a hierarchical structural design up to the macroscopic size range. These basic building principles are well displayed in the nacre shell of red abalone (*Haliotis rufescens*) (Figure 1).

On the macroscopic level, many mollusk shells follow the geometric shape of the logarithmic spiral, which is a mechanically particularly stable design (Figure 1 A).[4] The mechanically stable materials and structure of the shell function to protect the soft parts of the animal and are evolutionary optimized. In addition, several micro and nano sized design features enhance the

mechanical performance of nacre. One of the most prominent micro sized features are the hexagonal shaped aragonite platelets arranged in multilayers, which are embedded in an organic matrix consisting of proteins and polysaccharides (chitin fibers) (Figure 1 B and C). The

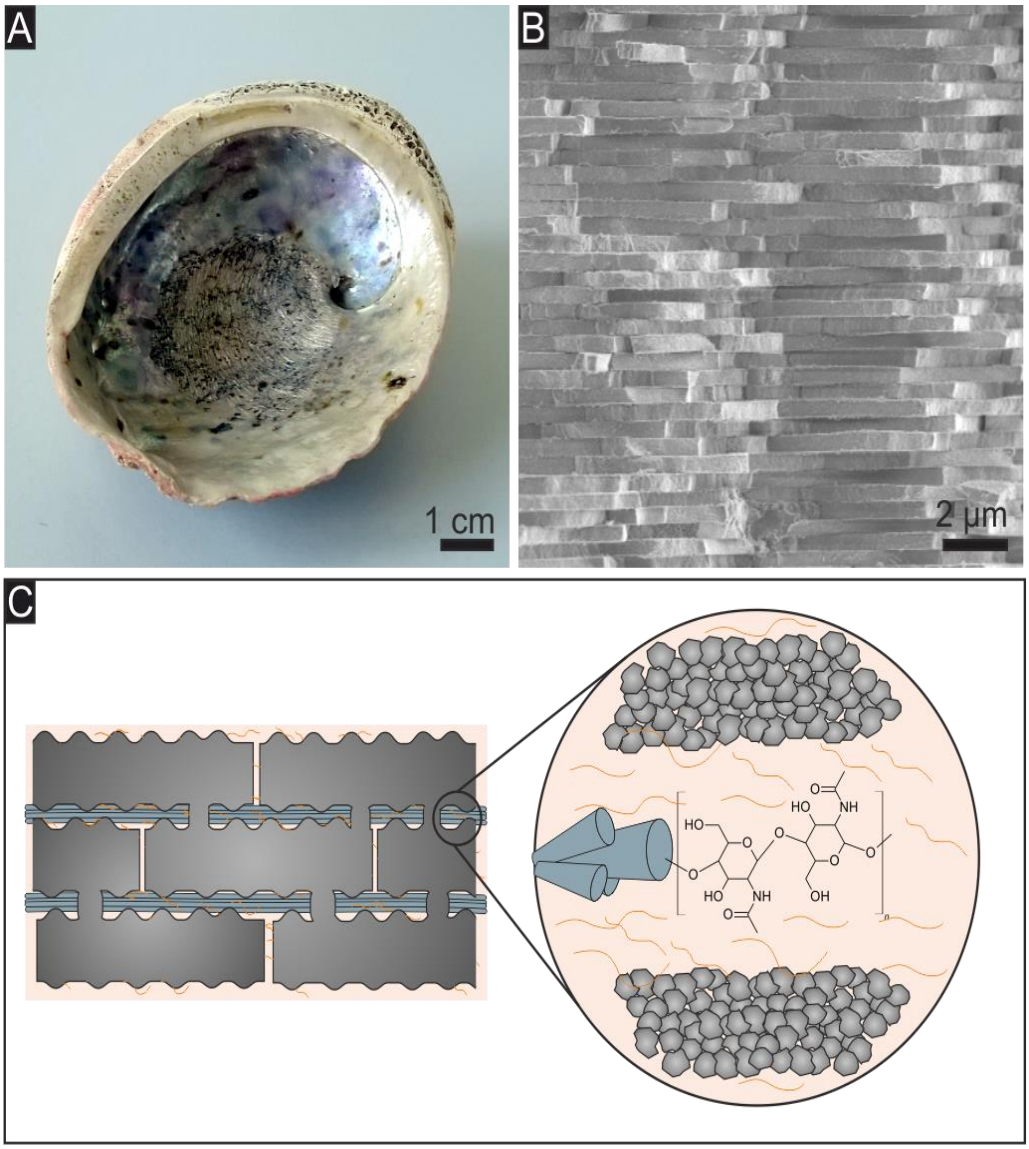

Figure 1. Basic building principles of natural hybrid materials shown on the example of mother of pearl. A) Red abalone shell (*Haliotis rufescens*), with the iridescence nacre layer at the inside of the shell. B) SEM cross section image of nacre. C) Schematic depiction of the nacre architecture. The aragonite platelets (grey) are connected by mineral bridges. The platelets consist of nanoparticles and a small content of organic molecules. Between the aragonite layers, the organic phase is formed by chitin fibers (blue) and different proteins (light orange).

unique design and materials combination lead up to 30 times higher fracture toughness of this hybrid material than for pure calcium carbonate ($CaCO_3$, aragonite), which is the main component (95 wt%) of nacre.[4] The organic matrix is a key feature of biohybrid materials. It

directly influences the physical properties of the materials and facilitate the formation of specific materials and structures in a so-called templated synthesis process.[5]

A template is defined as a pattern or mold, which is used to determine the shape of the material. In general, templated materials synthesis consists of three successive steps (I) template fabrication, (II) template directed synthesis of the target material and (III) the removal of the template[5] latter is not necessary in case of biohybrid materials. Natural templates, such as peptides and proteins, are designed for a defined interaction with the inorganic material. In vitro studies of proteins extracted from abalone shells showed its control over the nucleation, the growth, the morphology and the phase of mineralized $CaCO_3$ crystals.[6]

Here , peptides and proteins are highly interesting templates, because they possess a high specificity and a defined 3D shape, which is up to now, not achieved by synthetic macromolecules, such as polymers and polyelectrolytes. Several approaches demonstrated the use of proteins from different organisms for the control of particle/material formation of technical relevant metals[7] or semiconductors.[8] However, these templates lack the specific interactions found in biological systems, resulting in only a limited control of the synthesized hybrid materials. Technically relevant inorganic materials are not found in living nature and thus no specific biotemplates can be extracted from organisms. Therefore, methods for the identification of artificial peptides, which specifically interact with technical relevant inorganic materials, so-called inorganic binding peptides, are needed.[9]

Combinatorial display techniques, where artificially constructed peptides are presented at the surface of bacteria (bacterial surface display), M13 bacteriophages (phage display), yeast cells (yeast surface display) or ribosomes (ribosome display) are powerful techniques for the selection of inorganic binding peptides.[9] In 1985, the phage display (PD) technique was first used by G.P. Smith to probe specific peptide-peptide interaction.[10] Since then, several studies showed that the technique can be used to identify peptides, specifically interacting with technical materials like gold (Au),[11] zinc oxide (ZnO),[12] zirconia (ZrO_2)[13] or titania (TiO_2).[9]

In **Chapter 2** the phage display technique was used to identify inorganic binding peptides which bind to the surface of tin(II) oxide (SnO) particles. These findings were used to synthesize artificial short peptides with graduated interaction strengths towards the SnO particle surface. These peptides were applied in mineralization experiments to control SnO particle morphologies in a low temperature hydrothermal synthesis. A direct relation between

the interaction strength of the peptides and the aspect ratio of the synthesized cross- and flower-like SnO particles was found. The research aimed on the control of the morphology of individual metal oxide particles, but most applications in semiconductor industries rely on arranged nanostructures or thin films.[1]

In order to integrate inorganic binding peptides into hybrid materials with defined nano- and microstructural arrangements it is necessary to arrange these peptides into a distinct 2D and 3D array, e.g. in nacre first chitin fibers are formed which are then surrounded by glycoproteins.[14] Here virus particles such as M13 phages are interesting because they consist of large, ordered assemblies of proteins. The M13 bacteriophage (M13 phage) is a filamentous virus with a length of around 900 nm and a diameter of 6-7 nm.[11] M13 phages belong to a group of filamentous bacterial viruses (M12, M13 and M20) which were first described by Hofschneider in 1963, here the “M” in the name stands for Munich as place of discovery.[15] The protein surface of the M13 phage consists of five different coat proteins (p3, p6, p7, p8 and p9). 2700 copies of the major coat protein p8 form the major part of the M13 phage surface. This protein coat covers a circular single stranded DNA.[11]

Studies demonstrated the potential of surface modified M13 phages for applications in medicine[16] or materials synthesis.[17] In general, there are two routes for the surface modification: (I) by chemical methods or (II) by genetic engineering of the M13 phage DNA. Chemical methods enable the attachment of a nearly unlimited number of different molecules, enzymes and polymers but still lack in site selectivity and conversion efficiency as usually only up to 80% of the M13 surface proteins were modified.[18] Here, genetic engineering enables the surface modification by exchange or addition of amino acids to the surface coat proteins with a conversion efficiency of 100 % and precise site selectivity.[19] Furthermore, not only individual amino acids can be added to the coat protein but also short inorganic binding peptides, with this, M13 phage clones with site selective high binding affinities towards inorganic surfaces can be constructed.[11]

In order to integrate these genetically modified M13 phages in semiconductor applications methods such as dip coating[20] or convective assembly[21] to fabricate ordered arrays and template layers, consisting of a large number of viral particles for the deposition of metal oxides (Figure 2).

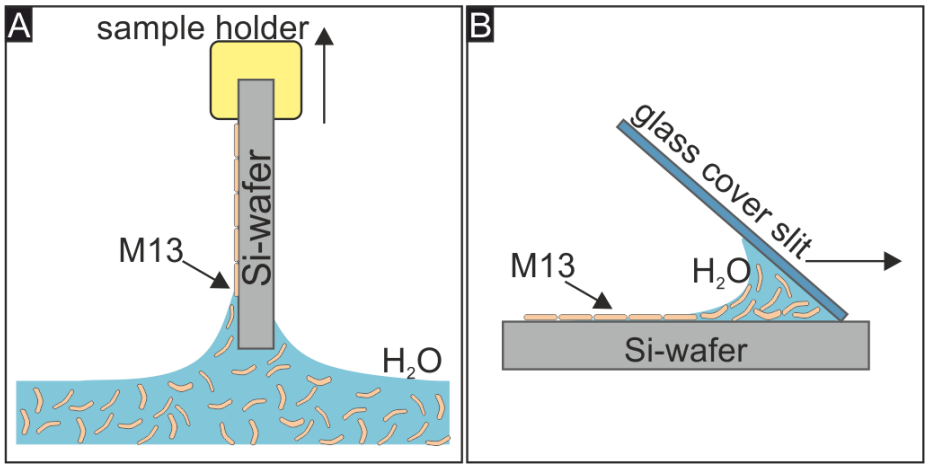

Figure 2. Schematic depiction of A) the dip coating process to produce homogenous M13 phage layers and B) a convective assembly process. The small volume of required M13 phage solution is beneficial compared to dip coating.

In addition, this enables the fabrication of multilayer structures with alternating organic and inorganic layers resembling the microstructure of nacre. The combination of a specific organic-inorganic interaction, conveyed by the inorganic-binding peptide, and the macroscopic structure of nacre, mechanical resistance of such hybrid material systems was enhanced, which is demonstrated in **Chapter 3**.

In a layer-by-layer process, multilayer structures were synthesized consisting of nanocrystalline layers of the metal oxide zinc oxide (ZnO) with intercalating M13 phage layers. Like the natural role model nacre, these multilayers had a high mechanical stability namely high Young's modulus, hardness and fracture toughness. Furthermore, the direct impact of the M13 phage surface modification on the mechanical properties of the multilayers was demonstrated. By expression of a ZnO binding peptide the Young's modulus and hardness were increased, whereas a slightly weaker binding peptide lead to the improvement of the fracture toughness compared to multilayers with unmodified wild type M13 phages with no specific interaction towards ZnO.

Up to here, only the surface properties of proteins for the interaction with an inorganic phase have been focused, but a key feature of peptides and proteins is the highly reproducible self-assembly into stable three-dimensional shapes (tertiary structures). The major coat protein p8 of M13 phages consists of 50 amino acids residues which form a stable protein tertiary structure with electrical dipole properties.[22] Recent studies on bone[23] regeneration bring the influence of piezoelectricity on the mineralization of hydroxyapatite in the focus of scientists. Collagen, which is the main organic component of bones, shows a polar uniaxial alignment of molecular dipoles resulting in its piezoelectric properties.[24] In *in-vitro* experiments the highest mineralization rates were observed on strained collagen fibrils indicating a direct link of high piezoelectric response and hydroxyapatite deposition.

In **Chapter 4** of this thesis it is shown, that structure and arrangement of the major coat protein p8 in the protein coat of M13 phages also lead to a polar alignment of intrinsic dipoles of ZnO nanocrystals. Therefore, M13 phages are used as model organism to investigate the influence of such dipole fields on the deposition of polar metal oxides e.g. ZnO. The effect of a varying dipole strength was investigated by generation of genetically modified M13 phages.

The bioinspired fabrication processes and materials design principles enable a better understanding of important parameters to promote highly specific organic-inorganic

interactions for improvement of existing and the creation of novel hybrid materials. Here, M13 phages are a suitable platform for the generation of different physicochemical properties in a highly defined structure. This enables a direct comparison of different hybrid materials with varying organic-inorganic interactions, but same biotemplate. Thus, this approach allows the investigation of interfaces and intermolecular interactions in hybrid materials and their influence on the macroscopic materials properties.

1.1 References

[1] M. Bathe, L. A. Chrisey, D. J. C. Herr, Q. Lin, D. Rasic, A. T. Woolley, R. M. Zadegan, V. V. Zhirnov, Nano Futures 2019, 3, 012001.

[2] M. A. Meyers, P. Y. Chen, A. Y. M. Lin, Y. Seki, Progress in Materials Science 2008, 53, 1; C. A. Mirkin, T. A. Taton, Nature 2000, 405, 626.

[3] J. Aizenberg, P. Fratzl, Advanced Materials 2009, 21, 387.

[4] M. A. Meyers, J. McKittrick, P.-Y. Chen, Science 2013, 339, 773.

[5] Y. Liu, J. Goebl, Y. Yin, Chemical Society Reviews 2013, 42, 2610.

[6] A. M. Belcher, X. H. Wu, R. J. Christensen, P. K. Hansma, G. D. Stucky, D. E. Morse, Nature 1996, 381, 56; I. W. Kim, S. Collino, D. E. Morse, J. S. Evans, Crystal Growth & Design 2006, 6, 1078; G. Fu, S. Valiyaveettil, B. Wopenka, D. E. Morse, Biomacromolecules 2005, 6, 1289.

[7] C. Hart, N. Abuladel, M. Bee, M. C. Kreider, A. C. Cvitan, M. M. Esson, A. Farag, T. Ibeh, E. N. Kalivas, D.-M. Larco, A. Walker Long, L. Lymperopoulos, Z. Mendel, N. Miles, C. M. Zareba, J. C. Schwabacher, H. Slucher, J. Vinals, J. M. Heddleston, W. Li, D. M. Fox, M. R. Hartings, Dalton Transactions 2017, 46, 16465.

[8] H. Uchiyama, S. Nakanishi, H. Kozuka, CrystEngComm 2015, 17, 628; J. M. Galloway, S. S. Staniland, Journal of Materials Chemistry 2012, 22, 12423.

[9] V. Thota, C. C. Perry, Recent Patents on Nanotechnology 2017, 11, 168.

[10] G. Smith, Science 1985, 228, 1315.

[11] D. Rothenstein, S. J. Facey, M. Ploss, P. Hans, M. Melcher, V. Srot, P. A. v. Aken, B. Hauer, J. Bill, Bioinspired, Biomimetic and Nanobiomaterials 2013, 2, 173.

[12] D. Rothenstein, B. Claasen, B. Omiecienski, P. Lammel, J. Bill, Journal of the American Chemical Society 2012, 134, 12547.

[13] D. Rothenstein, D. Shopova-Gospodinova, G. Bakradze, L. P. H. Jeurgens, J. Bill, CrystEngComm 2015, 17, 1783.

[14] J. H. E. Cartwright, A. G. Checa, Journal of The Royal Society Interface 2007, 4, 491.

[15] P. H. Hofschneider, Zeitschrift für Naturforschung B 1963, 18, 203.

[16] W.-J. Chung, D.-Y. Lee, S. Y. Yoo, International journal of nanomedicine 2014, 9, 5825.

[17] K. J. Koudelka, M. Manchester, Current Opinion in Chemical Biology 2010, 14, 810.

[18] J. M. L. Bernard, M. B. Francis, Frontiers in Microbiology 2014, 5.

[19] M. P. Kieny, R. Lathe, J. P. Lecocq, Gene 1983, 26, 91.

[20] W.-J. Chung, J.-W. Oh, K. Kwak, B. Y. Lee, J. Meyer, E. Wang, A. Hexemer, S.-W. Lee, Nature 2011, 478, 364.

[21] J. Rong, Z. Niu, L. A. Lee, Q. Wang, Current Opinion in Colloid & Interface Science 2011, 16, 441.

[22] B. Y. Lee, J. Zhang, C. Zueger, W.-J. Chung, S. Y. Yoo, E. Wang, J. Meyer, R. Ramesh, S.-W. Lee, Nature nanotechnology 2012, 7, 351.

[23] A. Ferreira, G. González, R. González-Paz, J. Feijoo, J. Lira-Olivares, K. Noris-Suárez, Acta Microscopica 2009, 18; A. M. Ferreira, P. Gentile, V. Chiono, G. Ciardelli, Acta Biomater 2012, 8, 3191; A. C. Ahn, A. J. Grodzinsky, Medical Engineering & Physics 2009, 31, 733.

[24] A. A. Marino, J. A. Spadaro, E. Fukada, L. D. Kahn, R. O. Becker, Calcified Tissue International 1980, 31, 257; K. Noris-Suárez, J. Lira-Olivares, A. M. Ferreira, J. L. Feijoo, N. Suárez, M. C. Hernández, E. Barrios, Biomacromolecules 2007, 8, 941.

2 Peptide controlled shaping of biomineralized tin(II) oxide into flower-like particles

(reprinted with permission of MDPI 2019)

Stefan Kilper, Timotheus Jahnke, Katharina Wiegers, Vera Grohe, Zaklina Burghard, Joachim Bill and Dirk Rothenstein

Abstract

The size and morphology of metal oxide particles have a large impact on the physicochemical properties of these materials, e.g. the aspect ratio of particles affects their catalytic activity. Bioinspired synthesis routes give the opportunity to control precisely the structure and aspect ratio of the metal oxide particles by bioorganic molecules, such as peptides. This study focusses on the identification of tin(II) oxide (tin monoxide, SnO) binding peptides and their effect on the synthesis of crystalline SnO microstructures. The phage display technique was used to identify the 7-mer peptide SnBP01 (LPPWKLK), which shows a high binding affinity towards crystalline SnO. It was found that the derivatives of the SnBP01 peptide, varying in the peptide length and thus the interaction, significantly affect the aspect ratio and the size dimension of mineralized SnO particles resulting in flower-like morphology. Furthermore, the important role of the N-terminal leucine residue in the peptide for the strong organic-inorganic interaction was revealed by FTIR investigations. This bioinspired approach shows a facile procedure for the detailed investigation of peptide to metal oxide interactions as well as an easy way for the controlled synthesis of tin(II) oxide particles with different morphologies.

2.1 Introduction

Environmental issues are in the focus of society and politics. To face these questions materials with tailored morphologies for e.g. high functionality in alternative energy storage and generation are needed. Tetragonal tin(II) oxide (tin monoxide, SnO) is due to its excellent electrical, physicochemical and optical properties highly interesting for applications as p-type semiconductor [1], electrode material for lithium-ion-batteries [2] or as catalyst [3] for various organic reactions e.g. the trans-/esterification for the synthesis of bio-diesel. As the shape and size of a material strongly influence its physicochemical properties [4, 5], a number of different micro- and nanostructures such as SnO nanowires [6], nanosheets [7], micro-crosses [8] or micro-flowers [5] have been recently published. Gas phase and solution based methods such as chemical vapor deposition (CVD) [9] or hydrothermal synthesis [10, 11] have been established. In these processes, the reaction is controlled mainly by temperature, pressure, pH value or concentration of the reactants.

A high degree of control in the synthesis of inorganic materials is accomplished in the natural process of biomineralization. Because of that, this process is attractive as a model for the targeted development of nanostructures or hierarchical structured assemblies in technical processes. Biomineralization is the formation of inorganic materials by living organisms, giving the opportunity to control the phase and morphology of the hybrid materials by bioorganic molecules, such as proteins [12]. The control over the synthesis is based, inter alia, on the specific interaction between the organic and inorganic phase. However, nature's toolbox on inorganic-binding peptides is limited mainly to materials with restricted technical importance. Therefore, methods such as the phage display (PD) technique are essential for the identification of peptides specifically interacting with technical relevant metals, such as semiconductors or insulators like gold (Au) [13], zinc oxide (ZnO) [14], zirconia (ZrO_2) [15] or titania (TiO_2) [16]. Even though, SnO is a material with a high technical potential, there are no specifically binding peptides identified up to now. Only peptides interacting with tin(IV) dioxide (SnO_2) were reported [17].

Here, we present the identification of the 7-mer SnO-binding peptide SnBP01 (sequence: LPPWKLK) identified by the phage display technique. The peptides affinity to polycrystalline SnO was determined with a phage-based binding assay. The binding assay showed that genetically modified M13 phages, expressing SnBP01 fused to the N-terminus of the minor coat protein pIII, had a ~60 times higher binding affinity to SnO than the non-modified M13

wild type (wt) phages. On the molecular level, the N-terminal leucine (L) residues of SnBP1 was determined as one of the interaction sites of the peptide and the SnO. In a hydrothermal SnO synthesis approach the peptide SnBP01 and variants of it (SnBP01-1: LPPW or SnBP01-2: WKLK) controlled the aspect ratio of the emerging particles. Due to the influence of the peptide and its derivatives on the synthesis, the aspect ratio of the cross-like SnO structures further increased and formed flower-like particles. This allows for the synthesis of micrometer-sided SnO particles with a high aspect ratio.

2.2 Experimental Section

Phage Display

A 7-mer random peptide library (New England Biolabs Inc., USA) was used in the phage display (PD) technique to identify SnO binding peptides. The random combinatorial library of peptides is fused to the N-terminus of the minor coat protein pIII of the M13 phage. 10 µl of the phage peptide library contain around 100 copies of each 7-mer peptide. The PD technique was conducted following the manufacturer's manual [18]. Polycrystalline SnO powder (Tin(II) oxide 99.9% - 100 Mesh Powder, Alfa Aesar, USA) with an average particle size of ~20 µm was used as a substrate for the PD experiments. The powder was cleaned by suspending 5 g SnO in Milli-Q H_2O followed by 10 min centrifugation at 3220 g. Subsequently removal of the supernatant followed by resuspension in EtOH and again centrifugation was performed. After three times repetition of the procedure, the powder was dried at 80°C. For each biopanning procedure 20 mg of the SnO powder were equilibrated for 10 min in 1 ml TBST0.1 in an ultrasonic bath. After centrifugation at 10621 g for 2 min followed by removal of the supernatant, the SnO powder was resuspended in 200 µl TBST0.1. 10 µl of the phage peptide library (~ $1.2 \cdot 10^{11}$ phages) were added for 1 h under light agitation at 20°C. To remove unbound and weakly bound phages the SnO powder was washed 10 times with 1 ml TBST0.5. For this, first the powder was sedimented by centrifugation at 10621 g for 2 min. Subsequently the supernatant was removed and the powder resuspended in 1 ml TBST0.5 by gentle vortexing followed by another centrifugation step. Bound phages were eluted by 1 ml of 0.2 M Glycine-HCl (pH 2.2) supplemented with 1 mg/ml BSA. After 10 min of gently mixing, the powder is sedimented by centrifugation and the supernatant is transferred to a new 1.5 ml tube and neutralized by adding 150 µl of 1 M Tris-HCl (pH 9.1). The obtained M13 phages were amplified in *E. coli* ER2738 according to manufacturer's recommendations. Briefly 200 µl *E. coli* overnight culture are suspended in 20 ml LB media in a 250 ml Erlenmeyer flask and ~1 ml of the obtained M13 phage eluate were added and incubated for 4.5 h at 37°C under vigorous mixing. The M13 phage were purified by addition of PEG/NaCl and subsequent centrifugation steps. To enrich the obtained peptide pool the complete biopanning procedure was repeated 5 times by application of at least ~ $1.2 \cdot 10^9$ amplified M13 phages. The enrichment was monitored by DNA sequencing of 30 for the 4th and 5th round, respectively, randomly selected M13 phage clones.

Binding Strength Assay

The binding strength of a single peptide sequence was evaluated following a procedure according to Rothenstein *et al.* [14] Briefly, a M13 phage clone expressing only one peptide sequence fused to its minor coat protein (pIII) was amplified and the purified M13 phages were suspended in 100 µl TBS. The phage titer was determined in two independent experiment sets. A defined amount ($2.0 \cdot 10^9$ phages) of a M13 phage clone, expressing a binding peptide, or M13 wt phage, as reference, were incubated for 60 minutes at room temperature with 20 mg SnO particles. Unbound and weakly bound phages were removed from the SnO substrate by washing 10 times with 1 ml TBST0.5. The bound phages were eluted from the substrate by addition of 1 ml of 0.2 M Glycine-HCl (pH 2.2) supplemented with 1 mg/ml BSA. The titer of the eluted phages was determined according to manufacturer's manual (New England Biolabs, Inc.). Briefly, constant amounts of *E. coli* bacteria were incubated with dilutions of the phages and plated on LB medium. The plates were incubated over night at 37 °C. The plaque forming units (pfu) on each plate were counted. To calculate the phage titer the number of pfu were multiplied with the dilution factor and the volume of phages. The binding strength, which directly correlates to the phage titer, was determined by 3 agar plates from two independent experiments and normalized to M13 wt phage titer (M13 wt titer = 1).

Mineralization of tin(II) oxide microstructures

For the synthesis of SnO particles in the presence of the identified binding peptide sequence (peptide01 (SnBP01): LPPWKLK) and its derivatives (peptide01-1 (SnBP01-1): LPPW and peptide01-2 (SnBP01-2): WKLK) stock solutions of 0.2 M $SnCl_2 \cdot 2H_2O$ (ACS reagent 98%, Sigma-Aldrich, Germany) and 8 mM peptide were prepared in Milli-Q H_2O.

The peptide SnBP01 (7-mer peptide) and the peptide segments SnBP01-1 and SnBP01-2 (both 4-mer peptides) were purchased from a commercial manufacturer (EMC microcollections, Tübingen, Germany). Since in the C-termini of the peptides are blocked when expressed in the phage, the C-termini of the synthesized peptides were inactivated by amidation [19]. The N-terminal amide groups were not blocked.

The synthesis of the SnO reference structures was performed according to a modified reaction route inspired by Iqbal *et al.*[11] For the reference reaction 1 ml of mineralization solution was prepared with a final concentration of 30 mM $SnCl_2 \cdot 2H_2O$ and 2.6 M NH_3 (aq) (28%, VLSI Selectipur, BASF, Germany). For the peptide mediated synthesis first $SnCl_2 \cdot 2H_2O$, then 1mM

peptide and finally NH_3 (aq) were mixed. The synthesis of SnO particles was performed in 1.5 ml reaction tubes at 60 °C for 24 h. The SnO particles were identified as black particles precipitating at the bottom of the reaction tube. The white-yellow supernatant was removed with a pipette and the SnO particles were washed in 10 ml Milli-Q H_2O and subsequently in 10 ml ethanol. Finally, the particles were dispersed in Milli-Q H_2O and dried at room temperature.

Structural analysis

Structural characterization of the SnO powder samples was performed with scanning electron microscopy (Zeiss Gemini) at 1.5 kV. A small amount of SnO powder was given onto a SEM sample holder equipped with a conductive carbon adhesive tab. Excess powder was removed by gentle shaking. For the phase analysis of the synthesized particles powder x-ray diffraction pattern were obtained using a Rigaku SmartLab 3 kW X-ray diffraction system equipped with a copper-anode. Due to the small amounts, the samples where measured on an amorphous silicon plate, to avoid any reflexes of the sample holder. Therefore, a small pile of the synthesized powder was put in the center of the silicon plate, which causes an additional texturation of the measured x-ray data because the anisotropic particle shape and thereof a non-completely random distribution of the particle orientations.

FTIR

The FTIR spectra of the synthesized SnO particles were recorded using a Bruker Tensor II spectrometer equipped with an ATR sensor (spectral resolution of ± 2 cm^{-1}). The data analysis was performed with the OPUS software. The samples for FTIR spectroscopy were only washed with Milli-Q H_2O, in order to avoid denaturation of the surface attached peptides.

2.3 Results and Discussion

Phage Display

For the identification of SnO-binding peptides, a random 7-mer peptide library, displaying ~ 10^9 different amino acid sequences was used. The selection process by phage display comprised four to five biopanning rounds, each with four subsequent steps (I) binding of the phages to the substrate, (II) washing to remove weakly bound phage clones, (III) elution of the bound phages by pH shift of the solution and (IV) amplification of the binding phage clones in *Escherichia coli* (*E. coli)* bacteria (Figure S1).[18] As inorganic target, commercially available SnO powder with an average particle size of ~20 µm was used (Figure S2). In total, 50 clones were isolated from the random peptide library: 27 clones after the 4th and 23 clones after the 5th biopanning round. From the 50 phage clones 13 different peptide sequences were identified. The most enriched peptide was peptide SnBP01 with the amino acids sequence LPPWKLK. Moreover, 12 additional SnO-interacting peptides were selected from the peptide library, however in much less abundance (Table 1).

In order to specify the interaction sites in the peptide, i.e. to identify the interacting amino acid residues, the frequency of single amino acids in the isolated peptides were compared to the amino acid frequency in the native peptide library (Table 2). The enrichment or depletion of an amino acid is a first indication, if these amino acids might play a role in the organic inorganic interaction. For this, the multiplication factor was calculated, which is the quotient of the frequency of an amino acid in the confined peptide pool and the initial frequency of the amino acid in the native peptide library.[14]

Amino acids with a multiplication factor of more than 1.25 are defined to be enriched, between 0.75 and 1.25 the amino acids occur in similar frequencies and below 0.75 the amino acids are depleted. The most enriched amino acid was the basic histidine (H), which occurs 3.11 times more often than in the original library. The basic amino acids arginine (R) and lysine (K) were also enriched by the factor of 1.54 and 1.53, respectively. Beside the positively charged amino acids, the non-polar amino acid leucine (L) had a multiplication factor of 1.60. Contrasting the enrichment of positively charged amino acids, all negatively charged amino acids, aspartic acid (D) and glutamic acid (E), were depleted.

Table 1. Peptides Binding to SnO after the 4th and 5th biopanning round

No.	Peptide sequence	Frequency 4th round	Frequency 5th round	Isoelectic point (pI)[a]	Charge, pH 7.5 (a.u.)[b]
01	LPPWKLK	11/27	17/23	10.00	1.8
02	WSLSELH	4/27	2/23	5.5	-1.1
03	IGASVHR	1/27	0/23	10.00	0.9
04	AHHLKVS	1/27	0/23	9.06	0.9
05	NHPLYNR	1/27	0/23	9.06	0.8
06	ALEHTSR	1/27	0/23	7.19	-0.1
07	HPAIRPP	1/27	0/23	10.00	0.9
08	LHRHANL	2/27	1/23	10.00	0.9
09	SSNQFHQ	1/27	1/23	7.19	-0.1
10	KVPGHQQ	1/27	0/23	9.06	0.8
11	TLAPRTA	1/27	0/23	10.00	0.8
12	VGKTHAD	0/27	1/23	7.19	-0.2
13	FPLHELR	0/27	1/23	7.19	-0.1

* Note: [a]the isoelectric point (pI) and [b]the charge (a.u.) at pH 7.5 of the unfolded peptide was calculated with Protein Calculator v3.4 (http://protcalc.sourceforge.net)

Table 2. Amino Acid frequencies in SnO-binding peptides compared to the native peptide library

Amino acid	Multiplication factor*	Type	
H	3.11	basic	enriched
L	1.60	nonpolar	
R	1.54	basic	
K	1.53	basic	
A	1.20	nonpolar	not affected
Q	1.20	polar	
W	1.15	aromatic	
P	1.11	nonpolar	
N	1.01	polar	
F	0.93	aromatic	
S	0.91	polar	
I	0.82	nonpolar	
E	0.74	acidic	depleted
V	0.74	nonpolar	
G	0.72	nonpolar	
T	0.38	polar	
Y	0.20	aromatic	
D	0.19	acidic	
C	0	polar	
M	0	polar	

*Quotient of the amino acids in the identified peptides and the native peptide library (New England Biolabs). The multiplication factor is a measure of enrichment and depletion of amino acid residues. Peptides with a multiplication factor of more than 1.25 are defined to be enriched, between 0.75 and 1.25 the amino acids occur in similar frequencies and below 0.75 the amino acids are depleted.[14]

The isoelectric point of SnO is between pH 5.2 and pH 6.6[20], hence the SnO particles are negatively charged at pH 7.5 where the phage display was performed. Therefore, the enrichment of the positively charged amino acids in addition to the depletion of negatively amino acids in the selected peptides indicates that electrostatic interactions are one of the major driving forces for the peptide-SnO binding.

Binding Assay

The binding behavior of the identified peptide sequences was investigated for the three most abundant peptides (SnBP01: LPPWKLK, peptide02 (SnBP02): WSLSELH and peptide08 (SnBP08): LHRHANL). In addition, the peptide12 (SnBP12): VGKTHAD and peptide13 (SnBP13): FPLHELR, which were selected due to possible binding motif consisting of charged-uncharged-charged amino acid sequence[21]. In order to determine the binding strength M13 phage clones expressing only one of the selected peptides were bound to equal amounts of the SnO powder at pH 7.5 (Figure S1). Subsequently the particles were washed by vigorously mixing to remove the weakly bound phages. This washing step was repeated ten times, then the phage were eluted and the phage titer was determined. The titer provided a direct measure of the interaction since it correlates to the binding strength of the eluted peptide. The phage titer of M13 wild type (wt) phage was used as reference for the normalization of the binding values[14] (Figure 1). The binding affinity of the M13 phage clone expressing the peptide SnBP01 was found to be ~60 times higher than for the M13 wt phage. Here, a direct correlation of the peptide frequency in the phage display and the binding strength could be shown. All other peptides in the binding assay did not show a drastic increase of the binding affinity.

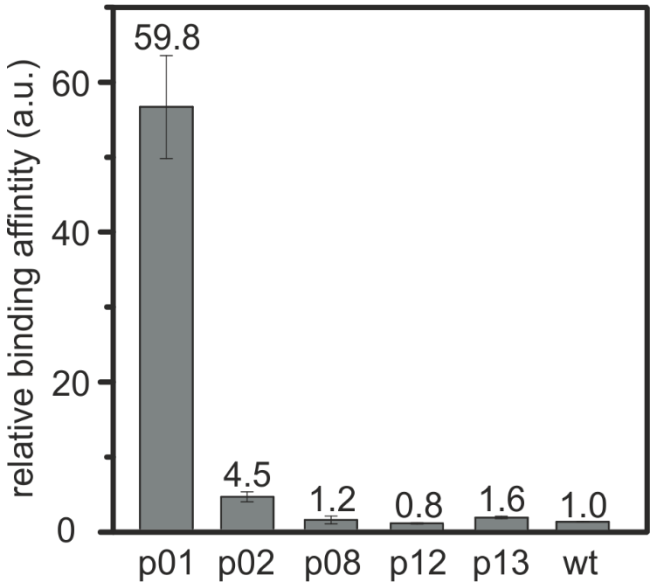

Figure 1. Relative binding strength of the M13 phage clones towards crystalline SnO powder with an average particle size of ~ 20 µm. The phage clones presenting SnBP01 show a much higher binding affinity towards the SnO surface compared to the other selected peptides or unspecific binding M13 wt phages.

Mineralization of tin(II) oxide microstructures

The influence of the binding peptide SnBP01 on the mineralization of tin(II) oxide microstructures was investigated. Therefore, the SnO synthesis procedure of Iqbal *et al.* [11] was modified for moderate synthesis temperatures (60 °C) to prevent denaturation of the peptides. First, $SnCl_2 \cdot 2H_2O$ was dissolved in ddH_2O and NH_3 (aq) was added, causing the precipitation of tin hydroxide [22, 23]. During this process, the pH of the solution increased to 10.8. After 24 h incubation at 60°C, black particles became visible. These particles exhibited cross-like SnO structures with a platelet aspect ratio of ~5.2 (Figure 2 A, Figure S3 and Table 3). The cross-like SnO particles were formed by twinned platelets with the crystallographic surface planes {001} and {110}, where the larger surface is usually assigned to the {001} planes, which have the lowest surface energy [11]. The platelet aspect ratio is defined as the quotient of the thickness (Figure 2 E) and the length (Figure 2 F) of one individual platelet. Furthermore, to investigate the influence of the SnO-binding peptide on the observed SnO morphology, the 7 amino acid long SnBP01 peptide (LPPWKLK) as well as the N-terminal, SnBP01-1 (LPPW), and C-terminal part SnBP01-2 (WKLK) (Figure S4) were applied in mineralization reactions. The peptides were purchased from a commercial manufacturer (EMC microcollections, Tübingen, Germany). In the phage display approach, the peptide library is fused with the peptides C-termini to the minor coat protein p3. Therefore, the C-terminal carboxy group of the peptide cannot contribute to the binding. Only the N-terminal amide group is freely accessible for interactions. Therefore, the C-terminus of the synthesized peptides was blocked by amidation [19] and the N-terminus was not blocked. It was found that the morphology of the synthesized SnO particles was strongly influenced by the addition of the peptides. The experiments were performed in triplicate and the measurement of the particle dimensions (i.e. thickness and length) are based on are based on minimum six measurement values. In particular, the addition of peptide segment SnBP01-2 (WKLK) significantly increased the aspect ratio of the cross-like SnO platelets to 25.0 (Figure 2 B, F, E, Figure S5 and Table 3) compared to 5.2 of the reference sample without peptide. The aspect ratio was further increased to 183.5 by the peptide segment SnBP01-1 (Figure 2 C, F, E, Figure S6 and Table 3). The major changes in particle morphology showed the full peptide SnBP01 (LPPWKLK), causing flower like structures with platelet aspect ratio 364.5 (Figure 2 D, F, E, Figure S7 and Table 3). It is noteworthy, that the pH of the mineralization solution was preserved during the synthesis. Moreover, the peptides (each at 1 mM) did not have a

significant influence on the pH value of the reaction, thus a pH-induced effect of the morphology changes can be excluded.

Table 3. Thickness, length and aspect ratio of the synthesized SnO structures

Sample	Thickness (µm)*	Length (µm)*	Aspect ratio (length/thickness)
Reference	11.67 ± 0.55	61.10 ± 12.00	5.2
WKLK	5.13 ± 0.36	128.10 ±17.53	25.0
LPPW	0.93 ± 0.16	171.16 ± 22.80	183.5
LPPWKLK	0.51 ± 0.13	184.83 ± 22.95**	364.6

*The measurement of the thickness and length of SnO platelets are based on minimum 6 measurements values.
**The length of these particles is based on the longest continuous platelet of a particle.

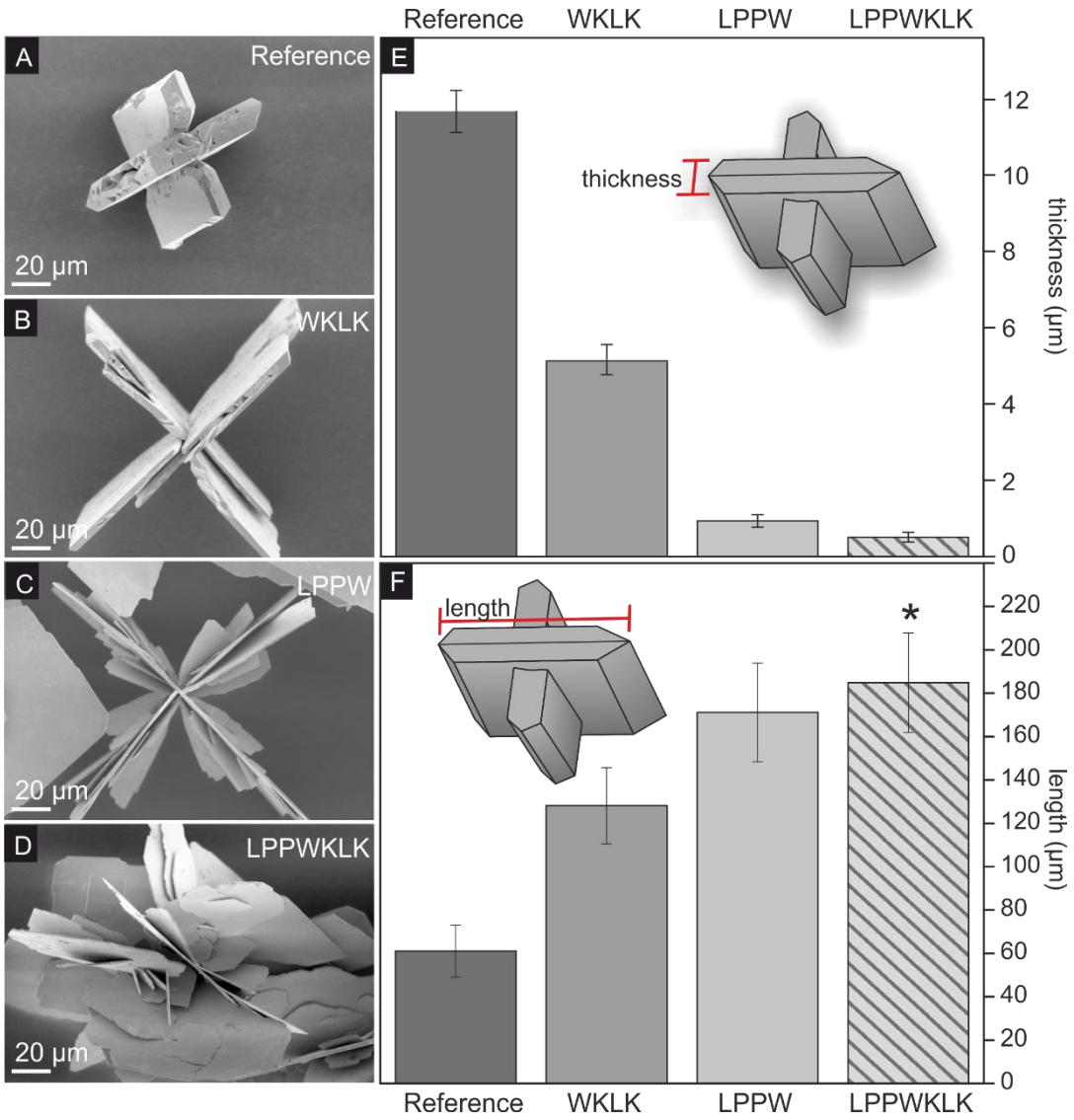

Figure 2. Results of the SnO microstructure synthesis in presence of the peptide SnBP01 and the peptide segments p-01-1 and SnBP01-2. SEM images of the different SnO morphologies synthesized with A) no peptide, B) SnBP01-2, C) SnBP01-1 and D) SnBP01. The corresponding platelet-thickness of the structures is shown in (E) and the platelet length (F). *Due to the irregular structure of the flower-like SnO particles always the longest.

The powder x-ray measurements of the SnO mineralized in the presence and absence a peptide additives showed for all samples tetragonal SnO (Figure 3 A). The strong c-axis texturation is most probably caused by the platelet shape, preventing a random particle orientation of the powder sample. The large influence of the peptides on the platelet thickness indicate that there is a preferential attachment of the peptides on the {001} planes, which leads to a strong reduction of the growth rate in the [001] direction.

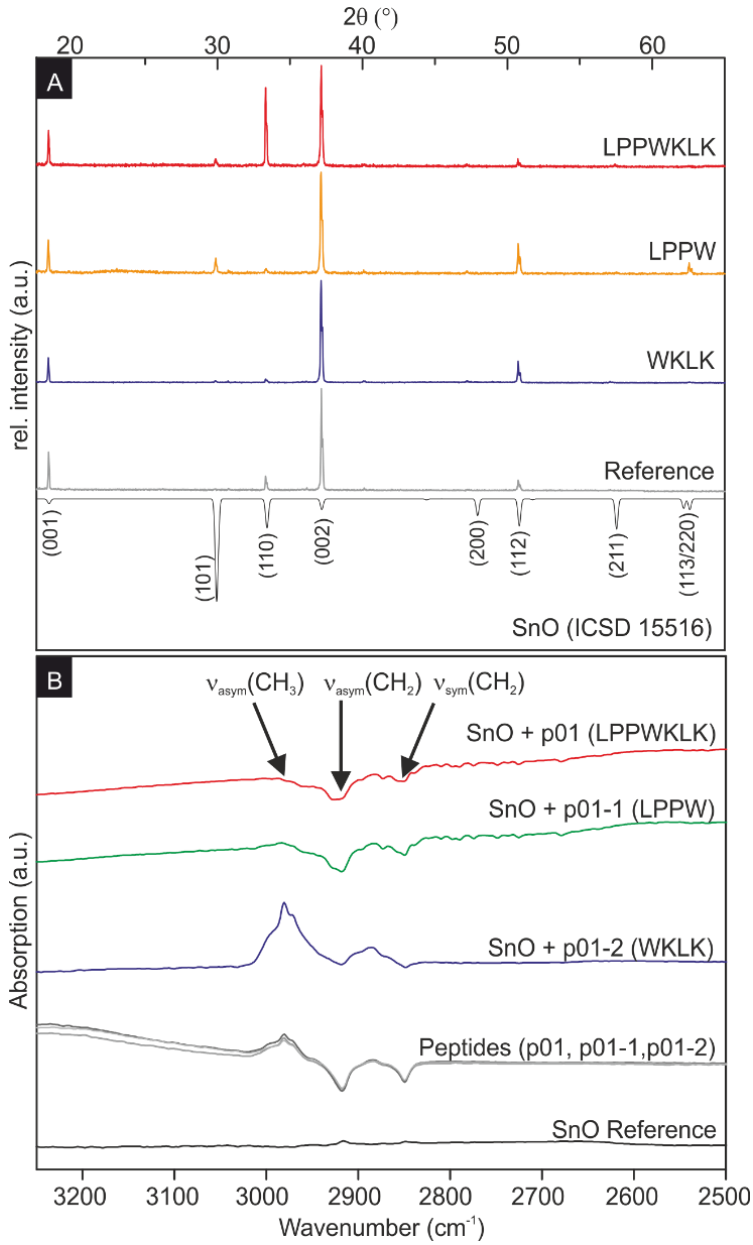

Figure 3. A) Powder x-ray diffraction data The powder x-ray data of crystalline SnO (ICSD 15516)[24] served as reference. The strong texturation of the measured x-ray spectra is caused by the platelet shape and sample preparation for the measurement. B) FTIR spectra of the SnO Reference without peptides (black), the three peptides (SnBP01, SnBP01-1, SnBP01-2) in solution (grey curves), the SnO structures with SnBP01-2 (WKLK) (blue), the SnO structures with SnBP01-1 (LPPW) (green) and the SnO structures with SnBP01 (LPPWKLK) (red).

Accordingly, it is concluded that the addition of peptides enhanced the anisotropic growth of SnO particles. This effect might be attributed either to the concentration of the additives or the strength of the organic-inorganic interaction. Since the molar concentration of all three peptides SnBP01, SnBP01-1, SnBP01-2 was constant (1 mM) the influence on the growth can be excluded. With respect to the interaction strength between the peptides and the SnO particles, the peptide SnBP01 and its subunit SnBP01-1 lead to an enhanced anisotropic growth compared to the subunit SnBP01-2. It is noteworthy, that the peptide segment SnBP01-2 showed a minor effect on the SnO mineralization, although it contains two lysine (K) residues for potential electrostatic interactions with the SnO surface. However, the high pH of the mineralization solution (pH > 11) might lead to uncharged lysine residues, since the pK_a value of lysine is 10.8 [25]. Therefore, electrostatic interactions between lysine and SnO may not be favored. Concluding, that the various morphologies induced by the three peptides are most probably a result of the interaction strength between peptide and inorganic phase. For non-specific interacting additives, like polyvinyl pyrrolidone (PVP) and gelatin, SnO morphologies were only manipulated by the different additive concentrations [23, 26].

For the investigation of the binding on the molecular level of the peptide to SnO, Fourier-transform infrared spectroscopy (FTIR) studies were performed. Infrared spectroscopy allows the direct and label-free determination of binding events between peptides and inorganic substrates [27, 28]. Due to the presence of ammonia in the synthesis, the signals of nitrogen containing functional groups were observed in all IR spectra from 4000 cm^{-1} to 500 cm^{-1} in all samples (including the SnO reference sample without peptide) (data not shown). Therefore, the FTIR measurements were focused on the spectral range between 3250 cm^{-1} to 2500 cm^{-1} (Figure 3) to monitor signals of the CH_2 and CH_3 groups of the peptides [27]. Moreover, the synthesized SnO did not possess IR activity in this spectral range (Figure 3B black curve). In solution, the three peptides only (SnBP01, SnBP01-1 and SnBP01-2) display the symmetric (ν_{sym}) and asymmetric (ν_{asym}) stretching of CH_2 at 2850 cm^{-1} and 2917 cm^{-1} as well as ν_{asym} of CH_3-groups at 2980 cm^{-1}, respectively (Figure 3 B, grey curves). These signals were also detected in the spectra of SnO particles, which were synthesized in the presence of the peptides. Most interesting, in case of SnBP01 and SnBP01-1 the relative intensity of ν_{asym} (CH_3) is strongly reduced while the relative intensities of ν_{sym} and ν_{asym} (CH_2) were not affected. This can be understood from the fact that from all the investigated amino acids, solely leucine (L) has a CH_3 group. The signal reduction can be attributed to an interaction [29] of a functional

group with an SnO particle. Therefore, the binding can be assigned to only the N-terminal leucine with the SnO surface. The signal intensity of the leucine residue of the peptide SnBP01-2, which is internally located, did not change in binding. However, not only the position of leucine at the N-terminus accounts for the binding. Obviously, also the neighboring amino acids influence the interaction, since peptide 08 (LHRHANL), which had an N-terminal leucine did not show an enhanced binding. One can speculate that in the SnBP01 and SnBP01-1, the leucine (L) is followed by two proline (P) residues (Figure S7). Proline has a unique influence on the conformation of a peptide restricting the free rotation of preceding amino acid residues [30] and might therefore advantageously expose leucine. It can be deduced that the main interaction of the peptides SnBP01 and SnBP01-1 with the SnO surface is mediated by the N-terminal leucine residue, which might be accessible due to the conformational restrictions caused by the neighboring proline residues.

2.4 Conclusions

The bioinspired synthesis route is appealing due to the generation of bioorganic templates with specific structural and chemical interfaces for the controlled deposition of inorganic components. In particular, inorganic-binding peptides play an important role in the control of the crystal formation. Here, the tin(II) oxide (SnO) binding peptide SnBP01 with the amino acid sequence LPPWKLK was identified by phage display and applied in the morphology control during the material synthesis. The peptide SnBP01, genetically engineered on M13 phages, conveyed a ~ 60 times higher binding strength towards SnO compared to unmodified M13 wt phages. The specific interaction allows for the modification of the SnO morphology in the used synthesis approach. The peptide SnBP01 increased the aspect ratio of the mineralized SnO platelets and changed the morphology from cross-like to flower-like structures. The interaction of the organic and inorganic phase was ascribed to the N-terminal leucine residue of the SnBP01 peptide, as well as a shortened derivative of this peptide. Moreover, by the comparison with other selected peptides it was observed that the neighboring proline residues of the leucine enhance the binding capability, probably due to their influence on the peptide conformation. This study shows that inorganic-binding peptides control the aspect ratio and morphology of mineralized inorganic particles mainly by its specific interaction and not its concentration. This bioinspired approach has also a broad impact for controlling and shaping the morphology and structure of other technological relevant oxides, for applications were a high surface area is required.

2.5 Supporting Information

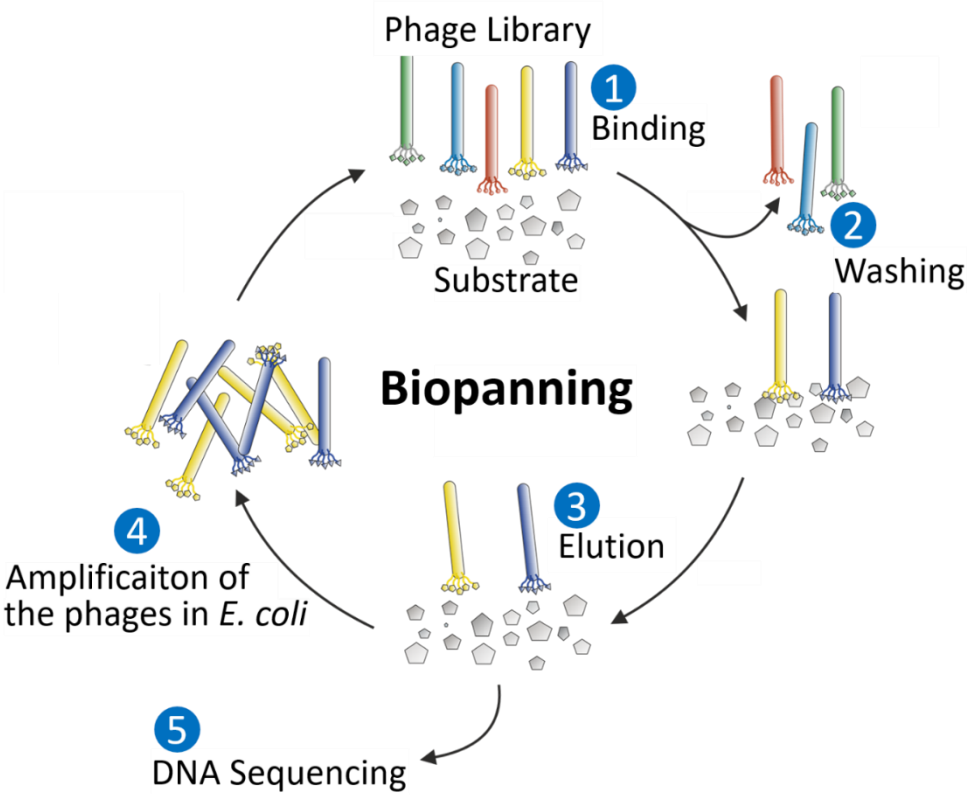

Figure S1. Principle of the phage display strategy for the isolation of SnO-binding peptides. Genetically engineered M13 phages express a peptide library as fusion protein with the pIII minor coat protein (Phage library). The phage-expressed peptide library is incubated with the inorganic target substrate (1). Non-binding phages are eliminated from the peptide pool by washing with appropriate buffers systems (2). Strongly bound phages are eluted by a pH shift (3). To increase the binding specificity of the peptides the eluted phages are amplified in *E. coli* (4) and the steps 1 to 3 are repeated, this procedure is called biopanning. The binding peptides are identified by DNA sequencing of the corresponding DNA section.

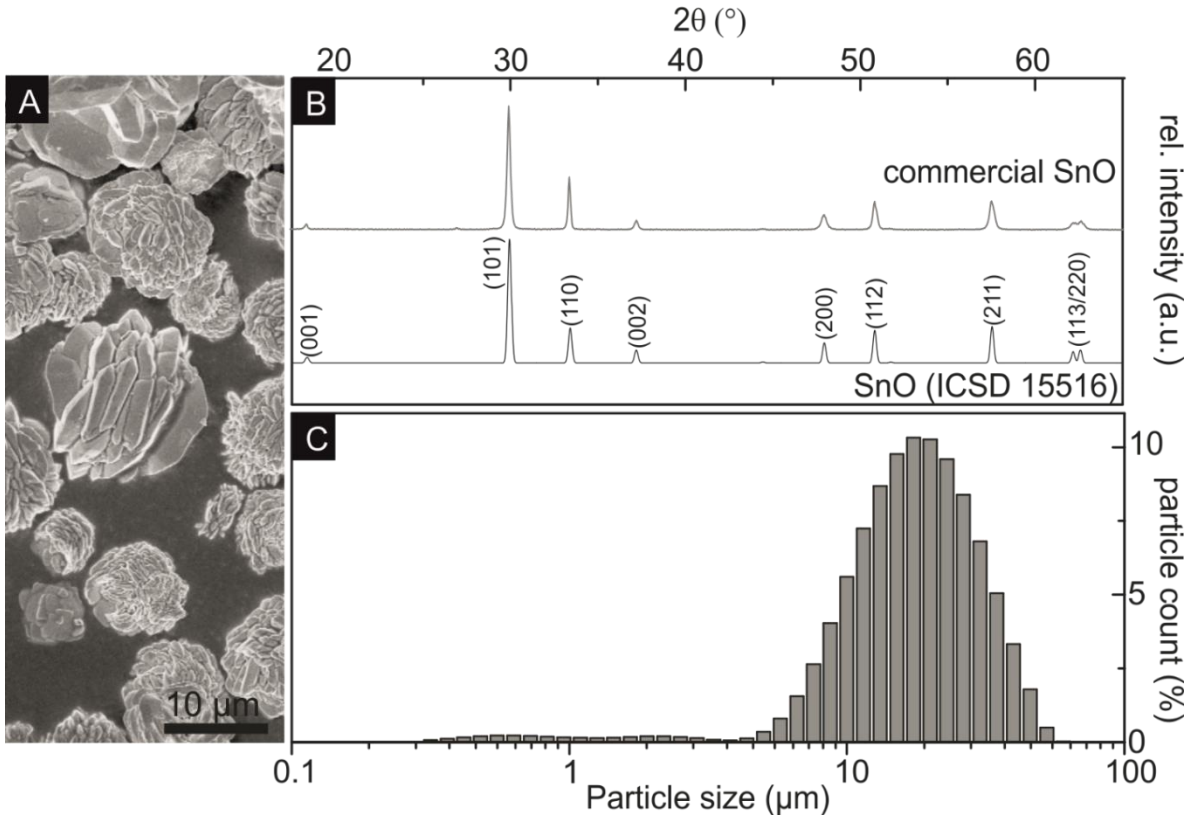

Figure S2. Structural characterization of the commercial SnO powder. A) SEM image of the +commercial SnO particles used for PD and Binding Assay. (B) Powder x-ray diffractogram of the commercial SnO powder. The powder x-ray data of the crystalline SnO (ICSD 15516)[24] used as reference. C) Particle size distribution. The particle size distribution was measured using a Mastersizer 2000 APA5005 (Malvern Instruments GmbH, Germany).

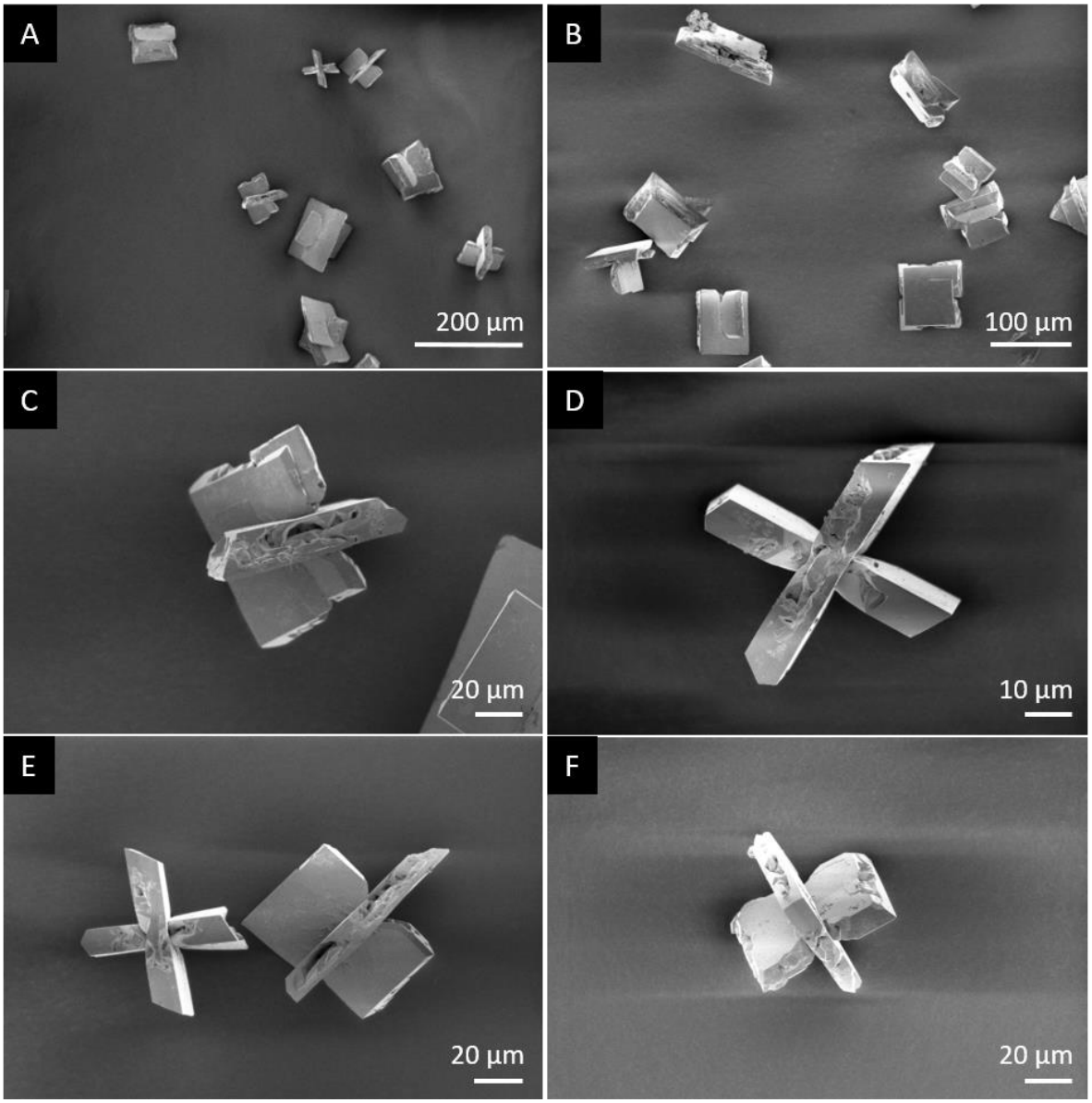

Figure S3. Synthesis of SnO microstructures in the absence of peptide additives. Overview micrographs (A, B) and single SnO microstructures form different experiments (C - F) under the same reaction conditions.

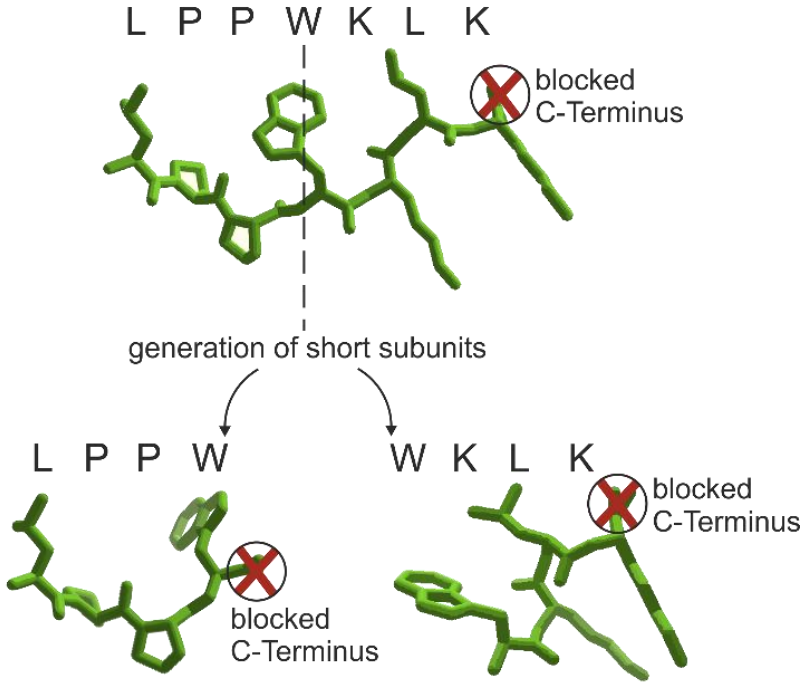

Figure S4. Schematic description of the construction of three solid state synthesized peptides based on the sequence of SnBP01 for the mineralization study of tin(II) oxide microstructures. Peptide SnBP01 (LPPWKLK), peptide SnBP01-1 (LPPW) and peptide SnBP01-2(WKLK). In phage display the peptides are connected by the C-Terminus to the minor coat protein p3, therefore the C-terminus of the synthezised peptides was inactivated by amidation. Structure created with Arguslab (http://www.arguslab.com) and refined with Foldit (https://fold.it/portal/).

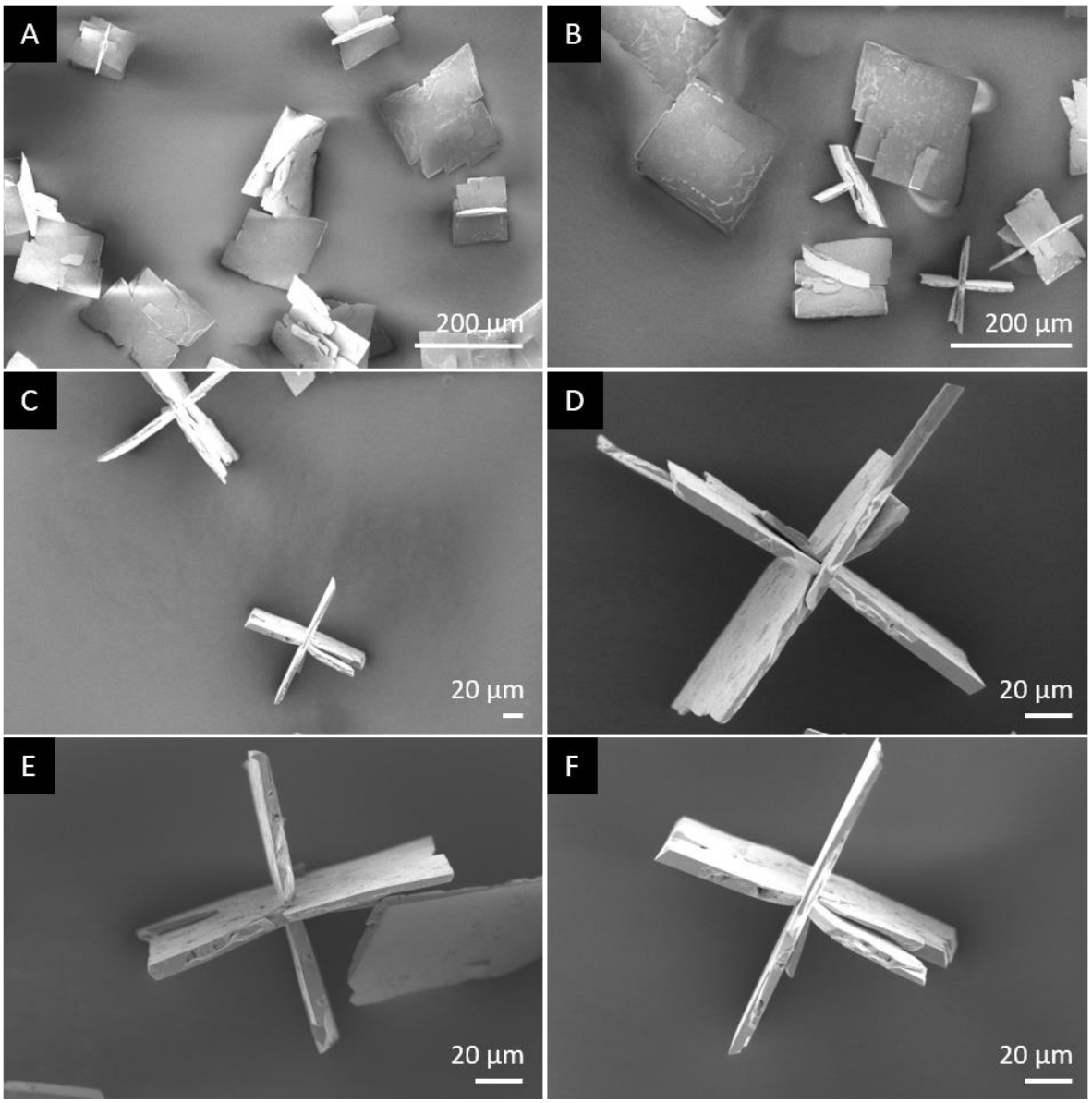

Figure S5. Synthesis of SnO microstructures in the presence of peptide segment SnBP01-2 (WKLK). SnO microstructures were mineralized in the presence of 1 nM peptide. Overview micrographs (A, B) and single SnO microstructures form different experiments (C - F) under the same reaction conditions.

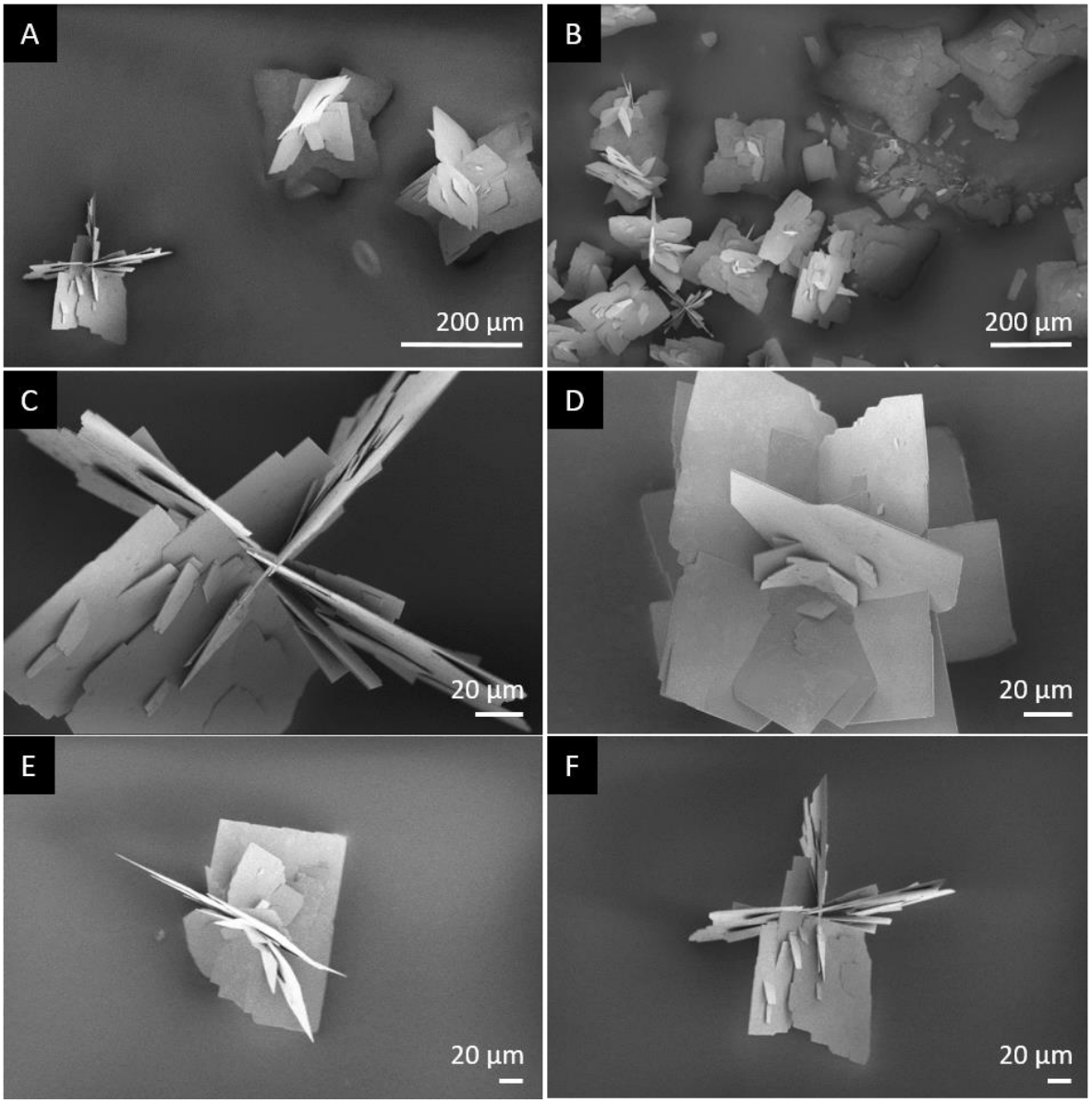

Figure S6. Synthesis of SnO microstructures in the presence of peptide segment SnBP01-1 (LPPW). SnO microstructures were mineralized in the presence of 1 nM peptide. Overview micrographs (A, B) and single SnO microstructures form different experiments (C - F) under the same reaction conditions.

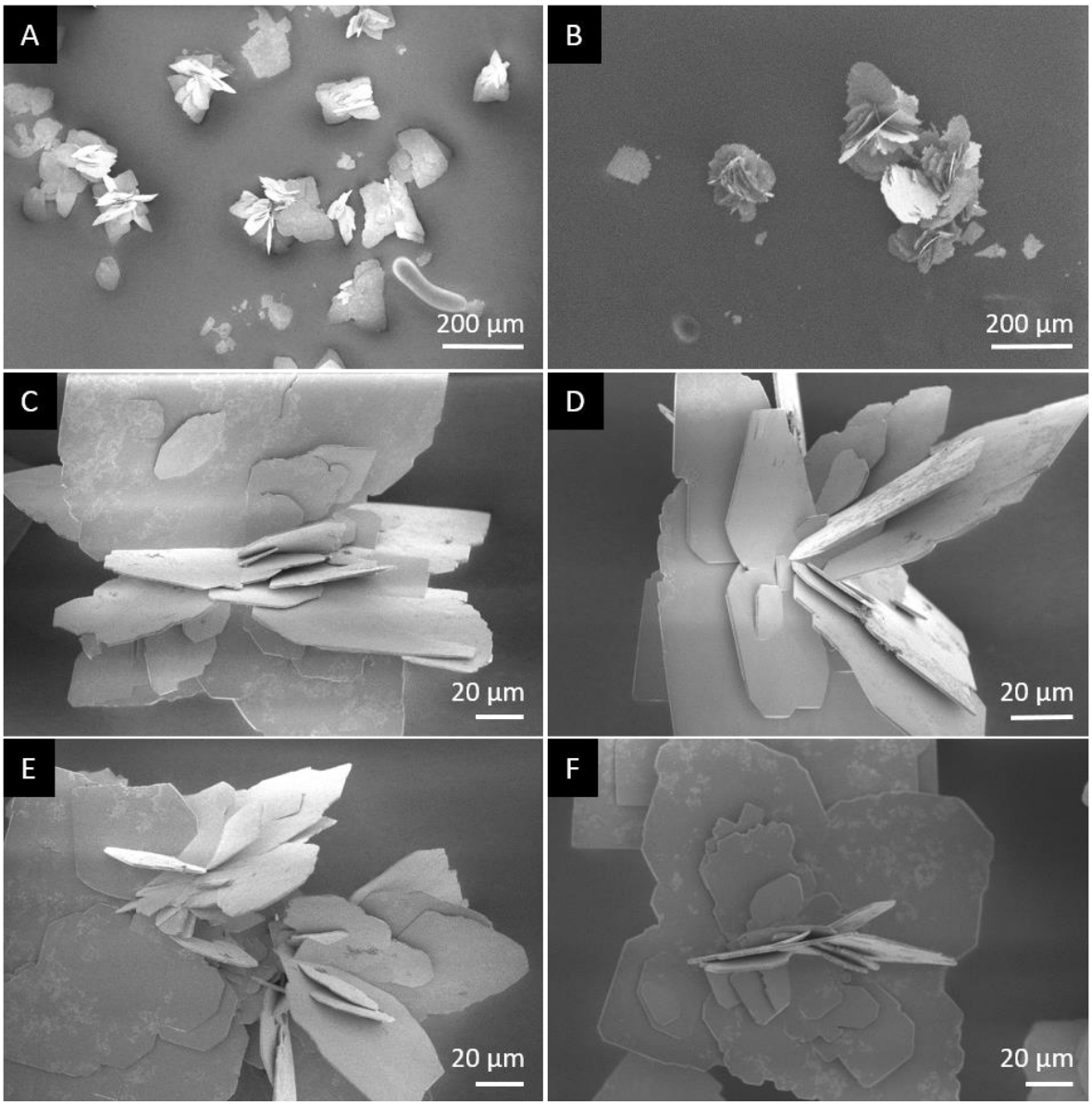

Figure S7. Synthesis of SnO microstructures in the presence of peptide segment SnBP01 (LPPWKLK). SnO microstructures were mineralized in the presence of 1 nM peptide. Overview micrographs (A, B) and single SnO microstructures form different experiments (C - F) under the same reaction conditions.

2.6 Acknowledgements

The authors especially want to thank Kevin Hildenbrand, Jonathan Link, Alexandros Georgiadis and Tamara Krauß (University of Stuttgart, Germany) for their experimental support. The authors are grateful to Dr. Ajay Vikram Singh of to the Department Sitti (MPI IS, Stuttgart) for the possibility to use the FTIR equipment and to the Department Sitti (MPI IS, Stuttgart) for the access to the SEM equipment. Financial support by the Vector Stiftung (Stuttgart, Germany) is highly appreciated.

2.7 References

[1] Y. Ogo, H. Hiramatsu, K. Nomura, H. Yanagi, T. Kamiya, M. Kimura, M. Hirano, H. Hosono, physica status solidi (a) 2009, 206, 2187.

[2] D. Aurbach, A. Nimberger, B. Markovsky, E. Levi, E. Sominski, A. Gedanken, Chemistry of Materials 2002, 14, 4155.

[3] M. J. da Silva, A. Lemos Cardoso, Journal of Catalysts 2013, 2013, 11; Z. Han, N. Guo, F. Li, W. Zhang, H. Zhao, Y. Qian, Materials Letters 2001, 48, 99.

[4] Y. Cheng, J. Huang, J. Li, L. Cao, H. Qi, IET Micro & Nano Letters 2018, 13, 257.

[5] Y. Liang, H. Zheng, B. Fang, Materials Letters 2013, 108, 235.

[6] K. Sakaushi, Y. Oaki, H. Uchiyama, E. Hosono, H. Zhou, H. Imai, Nanoscale 2010, 2, 2424.

[7] G. Sun, F. Qi, Y. Li, N. Wu, J. Cao, S. Zhang, X. Wang, G. Yi, H. Bala, Z. Zhang, Materials Letters 2014, 118, 69.

[8] X. Xu, M. Ge, K. Ståhl, J. Z. Jiang, Chemical Physics Letters 2009, 482, 287.

[9] B. Kumar, D.-H. Lee, S.-H. Kim, B. Yang, S. Maeng, S.-W. Kim, The Journal of Physical Chemistry C 2010, 114, 11050.

[10] Y. Cui, F. Wang, M. Z. Iqbal, Y. Li, A. M. Toufiq, Z. Wang, Z. Wang, S. Ali, Crystal Research and Technology 2015, 50, 210.

[11] M. Z. Iqbal, F. Wang, R. Hussain, M. Y. Rafique, S. Ali, I. Ali, Materials Focus 2014, 3, 92.

[12] S. Weiner, P. M. Dove, Reviews in Mineralogy and Geochemistry 2003, 54, 1.

[13] D. Rothenstein, S. J. Facey, M. Ploss, P. Hans, M. Melcher, V. Srot, P. A. v. Aken, B. Hauer, J. Bill, Bioinspired, Biomimetic and Nanobiomaterials 2013, 2, 173.

[14] D. Rothenstein, B. Claasen, B. Omiecienski, P. Lammel, J. Bill, Journal of the American Chemical Society 2012, 134, 12547.

[15] D. Rothenstein, D. Shopova-Gospodinova, G. Bakradze, L. P. H. Jeurgens, J. Bill, CrystEngComm 2015, 17, 1783.

[16] V. Thota, C. C. Perry, Recent Patents on Nanotechnology 2017, 11, 168.

[17] R. Naik, M. Stone, D. Carter, Google Patents, 2006; H. Nakazawa, Y. Seta, T. Hirose, Y. Masuda, M. Umetsu, Protein and Peptide Letters 2018, 25, 68.

[18] NEB, Vol. 2018, New England Biolabs GmbH, 2017.

[19] T. Togashi, N. Yokoo, M. Umetsu, S. Ohara, T. Naka, S. Takami, H. Abe, I. Kumagai, T. Adschiri, Journal of Bioscience and Bioengineering 2011, 111, 140.

[20] M. Kosmulski, *Surface charging and points of zero charge*, CRC press, 2009.

[21] M. L. Lemloh, K. Altintoprak, C. Wege, I. M. Weiss, D. Rothenstein, Materials 2017, 10.

[22] F. I. Pires, E. Joanni, R. Savu, M. A. Zaghete, E. Longo, J. A. Varela, Materials Letters 2008, 62, 239.

[23] H. Uchiyama, S. Nakanishi, H. Kozuka, CrystEngComm 2015, 17, 628.

[24] F. Izumi, Journal of Solid State Chemistry 1981, 38, 381.

[25] R. Wolfenden, L. Andersson, P. M. Cullis, C. C. B. Southgate, Biochemistry 1981, 20, 849.

[26] H. Wang, Y. Wang, J. Xu, H. Yang, C.-S. Lee, A. L. Rogach, Langmuir 2012, 28, 10597.

[27] I. A. Mudunkotuwa, A. A. Minshid, V. H. Grassian, Analyst 2014, 139, 870.

[28] C. Vreuls, A. Genin, G. Zocchi, F. Boschini, R. Cloots, B. Gilbert, J. Martial, C. Van De Weerdt, Journal of Materials Chemistry 2011, 21, 13841.

[29] J. Williams, S. Haq, R. Raval, Surface Science 1996, 368, 303.

[30] M. W. MacArthur, J. M. Thornton, Journal of Molecular Biology 1991, 218, 397.

3 Macroscopic properties of biomimetic ceramics are governed by the molecular recognition at the bioorganic-inorganic interface

Stefan Kilper, Sandra J. Facey, Zaklina Burghard, Bernhard Hauer,

Dirk Rothenstein, and Joachim Bill

Abstract

Bioinspired materials design aims for high-performing composite materials based on natural biomineralization processes and biomineral architectures. A key component to the research is the bioorganic-inorganic interface, one of the most crucial parameters for controlling the material properties. In this study, genetically engineered phages expressing an inorganic-binding peptide for the molecular recognition of a ceramic material was exploited to generate thin film multilayer assemblies, with the phage template as minority component. The bioorganic-inorganic interface in the ceramic (zinc oxide, ZnO) multilayer systems was strengthened by the ZnO-binding motif HSSHH of a peptide to increase Young´s modulus and hardness. Applying a point-mutated version of the peptide, DSSHH, which modulates the interface forces, showed an increased fracture toughness without deteriorating the Young´s modulus and the hardness. Molecular matching of the organic phase and its modulation in order to form a specific interface was shown to be important in controlling material properties like in natural biominerals. With this tool in hand, it is not only possible to imitate the structure of biominerals but also to genetically control the molecular recognition of bioorganic molecules to induce macroscopic effects in synthetic composite materials.

Kilper *et al.* Adv. Funct. Mater. 2018, 28, 1705842, Copyright © 2018 by John Wiley Sons, Inc.
Reprinted with permission of John Wiley & Sons, Inc.

3.1 Introduction

Bioorganic-inorganic composite materials distinguished in their physical and mechanical properties as well as in their architecture are omnipresent in living nature. The transfer of the efficiency from biominerals to high-performance synthetic composites is highly desired. The genetically controlled biomineralization process of organisms leads to the formation of composite biominerals consisting of a bioorganic and an inorganic phase. The superior material properties in such bio-hybrid materials originate from the intimate combination of the bioorganic and inorganic phases arranged in spatially defined architectures with the bioorganic molecules providing a well-defined interface. In general, biomineral properties depend to a large extend on the bioorganic-mineral interface,[1] i.e. the aptitude of biomolecules to interact with the inorganic phase. For example, strong atomic interactions at the bioorganic-inorganic interface imposed by the bioorganic phase may cause anisotropic lattice distortions that contribute to the mechanical properties.[2] Often, proteins are the active bioorganic molecules that control the interface forces, but polysaccharides or polyamines are also involved in mineralization processes.[3] On the molecular level, proteins incorporated in biominerals have a defined amino acid sequence and thus spatially arranged biochemical functionalities that together with the protein folding result in the molecular recognition of the inorganic phase in a quasi-key-lock principle, which may include a conformational change in the peptide upon binding to the inorganic substrate. Proteins thereby may interact with the mineral phase by electrostatic, polar, hydrophobic, and hydrophilic forces, respectively.[4, 5]

Examples of biomineralizing organisms can be found in all kingdoms of life showing evolutionary optimized synthesis strategies for the generation of bio-hybrid materials, providing among others efficient structural support (e.g. bones), orientation sensing (e.g. magnetosomes in bacteria) or protection (e.g. mollusc shells). Moreover, the bioorganic molecules guide the spatial arrangement of the inorganic phase and thus the architecture of the complete composite material influencing the effectiveness of material properties e.g. the mechanical performance. A common design principle found in mechanically stable biominerals is the alternating arrangement of bioorganic and inorganic layers; either in a planar arrangement (e.g. nacre)[6] or in a radially arranged multilayer system (e.g. sponge spicules) [7]. In sponge spicules, around a central proteinaceous axis, mineral nanoparticles and bioorganic molecules are arranged in concentric layers and in nacre the organic and inorganic

layers are arranged in a brick-and-mortar style, resulting in planar multilayer systems. Both systems apply common biological design themes and combine soft and stiff components in hierarchically arranged architectures. The inorganic component is present as nanometer sized platelets or grains and the soft organic phase as a minority component.[8] The fracture behavior of these architectures is based on toughening mechanisms, like crack deflection and crack bridging, along the organic-inorganic interfaces.[8, 9]

Ongoing research on biominerals opens up the opportunity to transfer the effectiveness from biological composites into man-made technical materials. However, technically relevant materials, such as metals and semiconductors e.g. zinc oxide (ZnO), are not mineralized as biomineral composites by any known organism. Therefore, research has focused on the generation of synthetic composite materials deduced from biominerals by combining polymers with inorganic materials. Layered assemblies of polymers or polyelectrolytes[10-12] and an inorganic phase were manufactured by applying techniques like freeze casting,[11] hot pressing[13] or 3D printing.[14, 15] Various polymers were applied to control the mineralization of inorganic materials. The water soluble polymer poly(sodium 4-styrenesulfonate) was shown to direct the ZnO synthesis by electrostatic interactions with the dipole moment of emerging ZnO nanoparticles.[16] In addition, the shape of mineralized ZnO nanoparticles was directed by the addition of positively and negatively charged polymers.[17]

Furthermore, proteins and peptides can be used in the mineralization of functional materials. Proteins, as bioorganic polymers, can be designed for the specific interaction with inorganic phases by the variation of the amino acid sequences. The physicochemical properties are genetically encoded and the proteins can be synthesized in biological systems with high accuracy. Moreover, the use of proteins and peptides allow the generation of large and complex functionalized template structures using genetic engineering of biological entities. To access inorganic-binding peptides, that show molecular recognition of non-biogenic ZnO, a pseudo random peptide library was screened by the phage display technique in previous work.[5, 18] This technique is based on a peptide library, consisting of $2.7*10^9$ different peptides, which are expressed as a fusion protein with the minor coat protein p3 in M13 phage clones, resulting in the presentation of one individual peptide per phage clone. The peptide library is incubated with a target substrate to allow the binding of the phage clones via the peptide to the substrate. Non-binding peptides are excluded from the peptide library while the specifically binding peptides are selected and the peptide sequences are analyzed. The

method allows the preselection of inorganic-binding peptides from a huge peptide pool and avoids the excessive testing of random peptide sequences in experiments. The ZnO-binding motif HSSHH was identified from a ZnO-binding peptide selected by phage display in a previous work.[5] Moreover, the affinity of amino acid residues can be deduced from the frequency of occurrence in the entity of the ZnO-binding peptides. The amino acid aspartate (D) was drastically reduced in ZnO-binding peptides (oxygen terminated surface of ZnO),[5] which indicates an adverse effect on the peptide-ZnO interaction. The inorganic-binding peptides allow the emulation of a proteinaceous interface with molecular recognition of ZnO. Using phages as a tool, it is possible to transfer the molecular building principles of biominerals to technical materials. However, the influence of a genetically encoded protein-based interfacial layer, interacting by principles of the molecular recognition with the inorganic phase, on material properties remains elusive.

In this study, the mechanical properties of a ZnO-based biomimetic composite material were adjusted by designing the bioorganic interface layer. For this, phage-templates showing molecular recognition of ZnO were genetically engineered (Supplementary **Table S1**) and multilayered composites were synthesized and analyzed by nanoindentation. The phage templates either express the ZnO-binding motif HSSHH[5] or a mutated version thereof (DSSHH) which harbors an aspartate residues (D), indicating an adverse effect on the ZnO interaction. Multilayer assemblies with 10 consecutive organic-inorganic layers were prepared by ZnO deposition on aligned phage templates under ambient conditions[19, 20] without affecting the phage integrity. The mechanical properties of the composites correlated with the genetic constitution of the phage templates. This report demonstrates that a specific bioorganic interface in biomimetic composite materials allows the genetic control of material properties like in natural biominerals.

3.2 Results and Discussion

Bioorganic/inorganic multilayer assemblies of phage-templated ZnO, which were structurally inspired by nacre, were synthesized in a layer-by-layer procedure (**Figure 1A**). To introduce a superordinate order of the phage templates and to obtain a homogenous template layer for the deposition of ZnO, which is only possible in the presence of the template layer, the phages were aligned by convective assembly on Si-wafer substrates. Since, the alignment of (biological) nanoparticles is influenced by factors like solvent properties (ionic strength and pH) and substrate surface properties[21] and also by the particle concentration, particle-

particle and particle-substrate interactions, the parameter for convective assembly were adjusted in order to homogenously cover a Si-wafer substrate with M13 phages (Supplementary **Figure S1**). The roughness of the template layer was measured by atomic

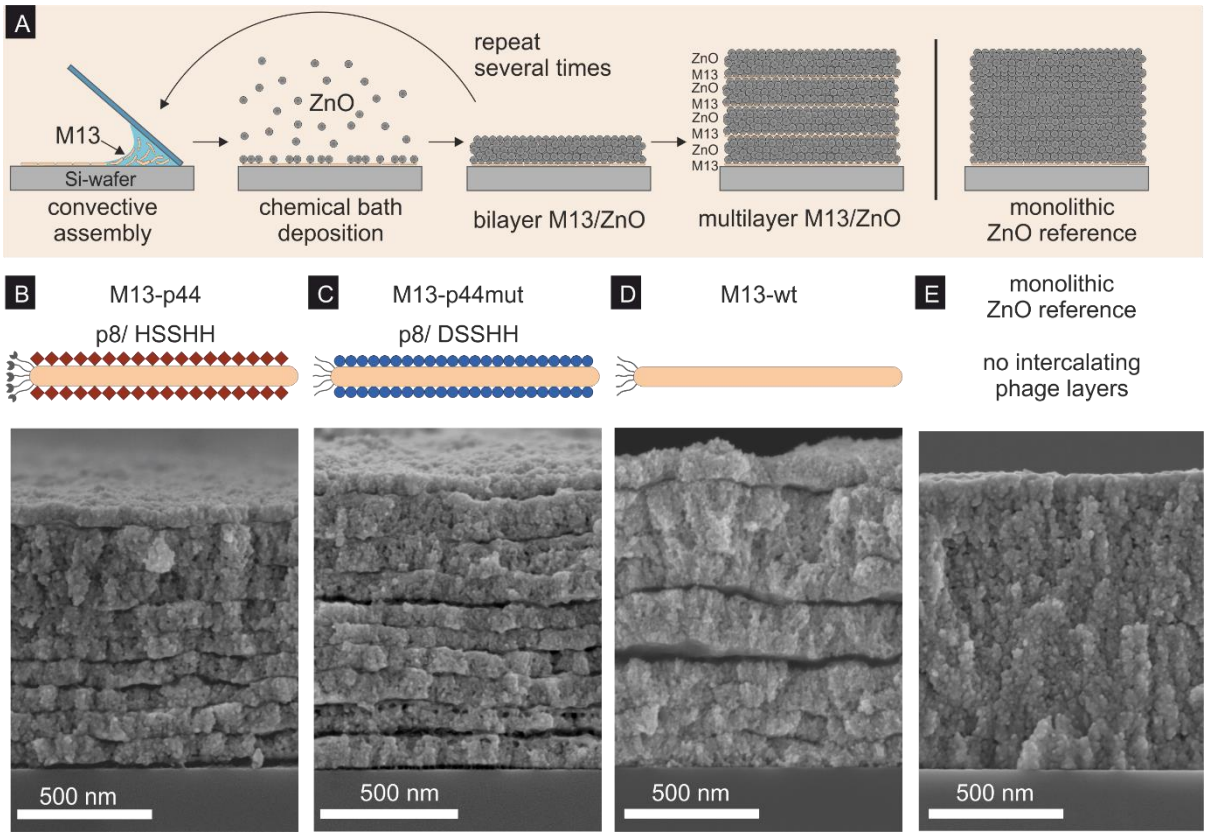

Figure 1. M13 phages as biotemplates for the generation of ZnO multilayer assemblies. A) Schematic representation of the multilayer synthesis. M13 phage templates were aligned by convective assembly and mineralized with ZnO nanoparticles by chemical bath deposition in a cyclical synthesis process. Schematic of phage templates and SEM-cross section of corresponding multilayers assemblies of B) M13-p44 phage, C) M13-p44mut phage, D) M13 wild type (wt) phage and E) monolithic ZnO references without intercalated M13 phage layers. Genetically modified M13 phage templates expressed either the ZnO-binding motif (M13-p44) or a mutated version (M13-p44mut), respectively. M13 wt phage with no functionalization were applied for referencing the influence of the genetic modification. All phage templates formed a dense layer on the Si substrate when aligned by convective assembly.

force microscopy (AFM) to ~ 4 nm root mean squared (rms) roughness (**Table 1**). The aligned M13 wild type (wt) phages, which are not genetically modified, were mineralized under mild reaction conditions in a chemical bath deposition (CBD) process without post-synthesis processing steps (e.g. annealing). The thermal stability of M13 bacteriophages in solution was reported to temperatures up to 85°C[22] allowing the ZnO deposition with this CBD process. The resulting nanocrystalline ZnO coating consisted of ZnO in the wurtzite structure with the

space group of $P6_3mc$. The crystallite size was calculated by applying the Scherrer equation to 14.5 nm ± 0.3 nm (Table 1). The analysis of the coherence length of D_{hkl} revealed identical values for D_{100} and D_{002} indicating equal dimensions of the crystallites in both dimensions. In a cyclical mineralization process, M13 wt phages and ZnO were deposited in multilayer assemblies with ten alternating phage-ZnO layers (Figure 1). The thickness of the multilayer assembly was 1.18 ± 0.044 µm with a roughness of 35.42 nm ± 1.62 nm rms (Table 1). The incorporation of phage templates in the multilayer assemblies was shown by TEM investigations in previous work.[23]

Table 1. Structural characterization of multilayer assemblies. Multilayer assemblies with ten M13/ZnO thin layers were synthesized. Film thickness was measured from SEM micrographs. The surface roughness of the multilayer assembly and the aligned phage template were determined by AFM. The crystallite sizes were calculated from XRD data.

Biotemplate	Film thickness (µm)	Multilayer roughness rms (nm)	Phage template roughness rms (nm)	Crystallite size (nm)
M13-p44	1.14 ± 0.136	27.93 ± 8.59	3.93 ± 1.7	14.57 ± 0.91
M13-p44mut	1.11 ± 0.195	21.68 ± 3.30	4.31 ± 0.2	14.22 ± 1.10
M13 wt	1.18 ± 0.038	35.42 ± 1.62	4.23 ± 1.5	14.68 ± 1.01

In order to enhance the hardness and the Young´s modulus of such multilayer assemblies the M13 wt phage template was modified for strong binding to ZnO based on the molecular recognition of the inorganic phase by a peptide (Figure 1B). Therefore, the phage template M13-p44 displaying the ZnO-binding motif HSSHH[5] was genetically engineered in a phage clone described earlier.[24] The binding motif was deduced from a peptide with a K_D of 260 nM for ZnO selected by phage display. NMR studies suggested that the ZnO-binding motif provides eleven possible interaction points to ZnO,[5] three sites per histidine and one per serine residue, respectively. The surface expression of the ZnO-binding peptide as N-terminal fusion to the p8 major coat protein of M13 enabled the spatially defined presentation in nanometer dimension, similar to the distance of ~3.2 and ~2.4 nm, respectively, of two neighboring p8 N-termini[25] resulting in a high functional density of approximately 130,000 peptides per μm^2. The aligned M13-p44 templates showed a similar roughness of ~ 4 nm rms like the M13 wt template (Table 1). Multilayer assemblies were synthesized with a similar roughness (27.93 nm ± 8.59 nm) and thickness (1.14 ± 0.136 µm) (Table 1).

For achieving an increase in fracture toughness, the interaction between the bioorganic and inorganic components was weakened in order to facilitate crack deflection and propagation at the bioorganic/inorganic interfaces. For that purpose, a second phage template, M13-p44mut, was established with a point-mutated version of the ZnO-binding motif (sequence DSSHH) (Figure 1C). The substitution of histidine by the negatively charged aspartate at position one resulted in a decrease of the possible interaction points to ZnO to nine, which was deduced from previous NMR studies.[5] Moreover, the amount of aspartate residues was drastically reduced in peptides binding to the oxygen-terminated side of (1000) ZnO, indicating an adverse effect on the peptide-ZnO interaction. The M13-p44mut template was aligned to smooth homogenous layers (~ 4 nm rms) and multilayer assemblies with a thickness of 1.11 ± 0.195 µm and a roughness of 21.68 nm ± 3.30 nm rms were prepared (Table 1).

The different phage templates did not affect the growth kinetics of ZnO. After one ZnO mineralization cycle the genetically engineered and wt phage templates showed the same height (Supplementary **Figure** S**2**, Supplementary **Table S2**). Moreover, the total thicknesses of the multilayer systems templated with different phage templates were also nearly identical (Table 1). This is also in accordance with the proposed ZnO growth mechanism,[19] where ZnO nanoparticles are formed in solution and deposit on template structures. Furthermore, all multilayer assemblies contained similar amounts of phage template (Supplementary **Table S3**) and showed a uniform roughness of the homogenously aligned phage templates (Supplementary **Figure S1**). Since the coat proteins of phage templates and thus the presented biochemical functionalities are arranged around the central DNA strand, the interaction with ZnO nanoparticles was not subjected to spatial limitations. Based on this structural uniformity of the three different phage types it was concluded that the biochemical functionalities per area in the multilayer assemblies do not differ significantly.

Mechanical properties

The Young's modulus and hardness were measured by continuous stiffness nanoindentation. In order to avoid surface and substrate effects on the mechanical measurements, the values were determined in a depth region of 10 % - 20 % of the total film thickness.[10]
The multilayer assembly templated on M13 wt, without molecular recognition of ZnO, and the M13-p44mut templated assembly, with the point-mutated ZnO-binding motif, had similar hardness and Young´s modulus values (**Table 2**).

Table 2. Mechanical properties of phage templated multilayer assemblies. The Young's modulus and hardness were measured by nanoindentation. For each phage type three independent samples were prepared. The fracture toughness was determined by the method of Xia *et al*.

Property	M13-p44	M13-p44mut	M13 wt
Young's modulus multilayer (GPa)	51.27 ± 2.59	42.00 ± 1.31	45.32 ± 2.52
Hardness multilayer (GPa)	2.63 ± 0.08	2.29 ± 0.08	2.31 ± 0.02
Fracture toughness multilayer ($\mathbf{MPa \cdot \sqrt{m}}$)	1.37 ± 0.23	2.29 ± 0.20	1.18 ± 0.26
Fracture toughness reference ($\mathbf{MPa \cdot \sqrt{m}}$)	< 0.83[a]	< 0.83[a]	< 0.83[a]

[a)] this value corresponds to the fracture toughness of the pure silicon substrate and is the highest value of the limit value approximation

The Young`s modulus was determined to be 45.32 ± 2.52 GPa and 42.00 ± 1.31 GPa and the hardness to be 2.31 ± 0.02 GPa and 2.29 ± 0.08 GPa for M13 wt and M13-p44mut, respectively. For the improvement of these mechanical properties, the adhesive forces between the ZnO layers had to be increased. The genetic introduction of the ZnO-binding motif into the M13-p44 template allowed for the molecular recognition of ZnO and thus resulted in a strong and specific interaction at the interface, which led to an enhancement of hardness and Young´s modulus. The hardness was increased by ~14 % and the Young's modulus by ~13 % compared to the M13 wt multilayer assemblies (**Figure 2**, Table 2). The Young's modulus and the hardness were improved only in multilayer assemblies templated with phages expressing the ZnO-binding motif (M13-p44). In contrast, phages expressing the mutated ZnO-binding motif (M13-p44mut) did not improve the mechanical properties of the composite. Therefore, we

conclude that the enhanced mechanical properties are not based solely on the composite architecture but mainly on the genetic constitution of the phage template, e.g. the molecular recognition of ZnO by the peptide. Two mechanisms might be accounted for the improvement

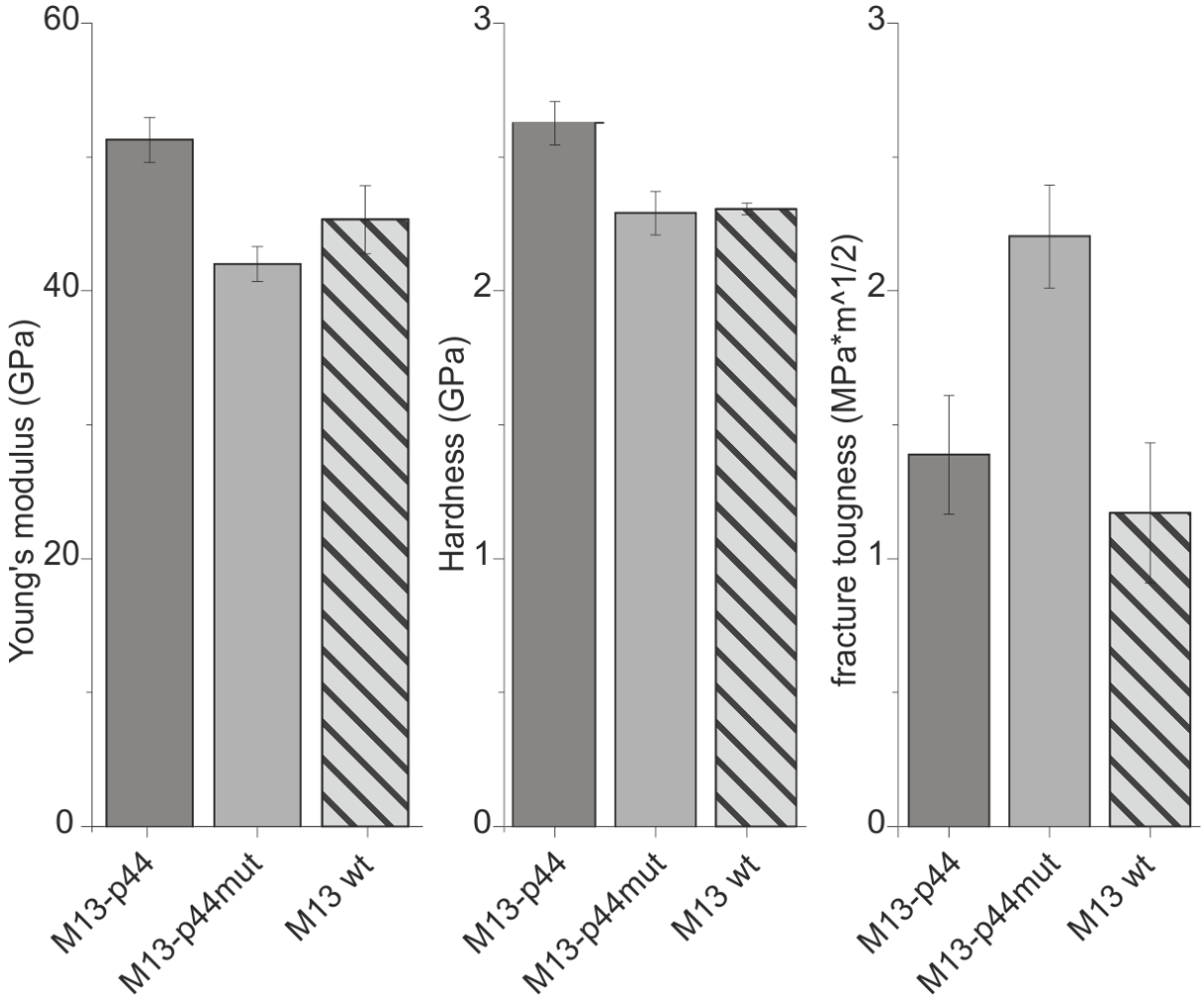

Figure 2. Mechanical properties of phage templated ZnO multilayer assemblies. The M13-p44 based multilayers showed the highest Young's modulus and hardness values compared to M13-p44mut and M13 wt multilayer assemblies. However, the fracture resistance of the M13-p44mut samples was the highest without a significant deterioration of its Young´s modulus and hardness, which in general, is a trade-off between these properties. The M13 wt samples showed the lowest fracture resistance.

of the mechanical performance of the multilayer system: (I) hardening according to different shear moduli of the multilayer constituents,[12, 26, 27] consequently additional external stress is needed to drive the deformation field across the interface, and (II) the hindrance of the propagation of the plastic deformation field associated with strong interactions at the interface.[27, 28] As the enhancement of Young´s modulus and hardness are connected directly with the ZnO-binding motif, the second mechanism might dominate the multilayer performance, concluding that a strong interfacial interaction is needed to improve hardness and Young's modulus. Supportive for this assumption is that the multilayer system based on phage harboring the mutated ZnO-binding motif do not show any increase in hardness and Young's modulus.

However, to strengthen the fracture toughness of a composite material, a moderate interaction of the bioorganic and the inorganic phase was favored for an efficient crack deflection mechanism. The crack lengths in the monolithic ZnO reference samples were longer than in the Si-wafer substrate (Supplementary **Figure S3**), indicating that there is no effective crack deflection mechanism in the absence of the bioorganic interlayers. A threshold value for the fracture toughness of monolithic ZnO samples was considered, assuming equal crack lengths in the substrate and the monolithic reference. The maximum threshold fracture toughness was calculated to be 0.83 $MPa \cdot m^{1/2}$, which is equal the fracture toughness of the Si-substrate.[10] In contrast, for all multilayer assemblies shorter cracks into the multilayer assemblies were observed than into the pure substrate (Supplementary Figure S3) indicating that all multilayer assemblies had an increased fracture toughness compared to monolithic ZnO references (Table 2). The M13-p44mut-templated multilayer assembly, with a reduced molecular recognition of ZnO, revealed the highest fracture toughness of 2.29 ± 0.20 $MPa \cdot m^{1/2}$, which was almost doubled compared to the M13-p44 and M13 wt multilayer systems, which had a fracture toughness of 1.37 ± 0.23 $MPa \cdot m^{1/2}$ (M13-p44) and 1.18 ± 0.26 $MPa \cdot m^{1/2}$ (M13 wt), respectively (Figure 2). This result is also supported by Mirkhalaf et al.[14] who modulated the toughness of borosilicate structures by infiltration with different polymeric materials, forming interfaces of different strength.

It is important to emphasize, although the fracture toughness was increased in the M13-p44mut multilayer system, the values for hardness and Young´s modulus did not significantly deteriorate. In general, the improvement of the fracture toughness is associated with the deterioration of the hardness and the Young´s modulus, which was also reported for nacre.[29]

In this artificial multilayer system however, the trade-off between the mechanical properties was suppressed by the choice of the genetically adapted bioorganic template.

3.3 Conclusion

Like in biological composite systems, the mechanical properties in the artificial ZnO multilayer system were controlled by the bioorganic phase. Since there are no ZnO-interacting proteins known to exist in organisms that can be directly applied in such systems, the ZnO-binding peptide was identified by the phage display method in order to design the bioorganic-inorganic interface for the control of the mechanical properties. In contrast to other polymer-inorganic hybrid materials, not only electrostatic interactions have been taken into account, but rather the precise control of the interface by genetic engineered phages.

Although, the organic component is the minor part of the synthetic composite material, it is the key for improving the materials properties. The amount and dimension of the various phage templates were constant in the multilayer assemblies. However, the surface properties of the phage templates were changed by the amino acid composition. Genetically engineered phage templates enhanced the mechanical properties compared to hybrid materials with improvement of the Young´s modulus and the hardness, while the point mutated ZnO-binding motif drastically increased the fracture toughness (**Figure 3**). More importantly, the increase of the fracture toughness did not result in a deterioration of the Young's modulus and the hardness, which in general can only be traded off against these properties.

The point-mutated ZnO-binding peptide demonstrated the significant influence of the interface established by the inorganic-binding peptides. The toughening mechanism of non-modified phage wt templates. The surface expressed ZnO-binding motif leads to the fracture toughness due to crack deflection was visualized in cross-sectional micrographs of multilayer assemblies (**Figure 4**). Depending on the interfacial interaction of the phage templates and ZnO, the crack propagation in the multilayer systems showed different degrees of crack deflection. The crack deflection mechanism was only seen in the phage-templated multilayer assemblies (Figure 4A - C), while monolithic ZnO samples did not have any indication of crack deflection (Figure 4D). A high binding strength of the biotemplate and ZnO realized with the M13-p44 phage (Figure 4A) leads to efficient crack deflection with a long crack path in the bioorganic layer. However, the most efficient fracture toughness mechanism, reflected by the longest crack path, was active when the cohesion of ZnO layers and the phage template was slightly reduced with the M13-p44mut carrying the mutated ZnO-binding motif (Figure 4B).

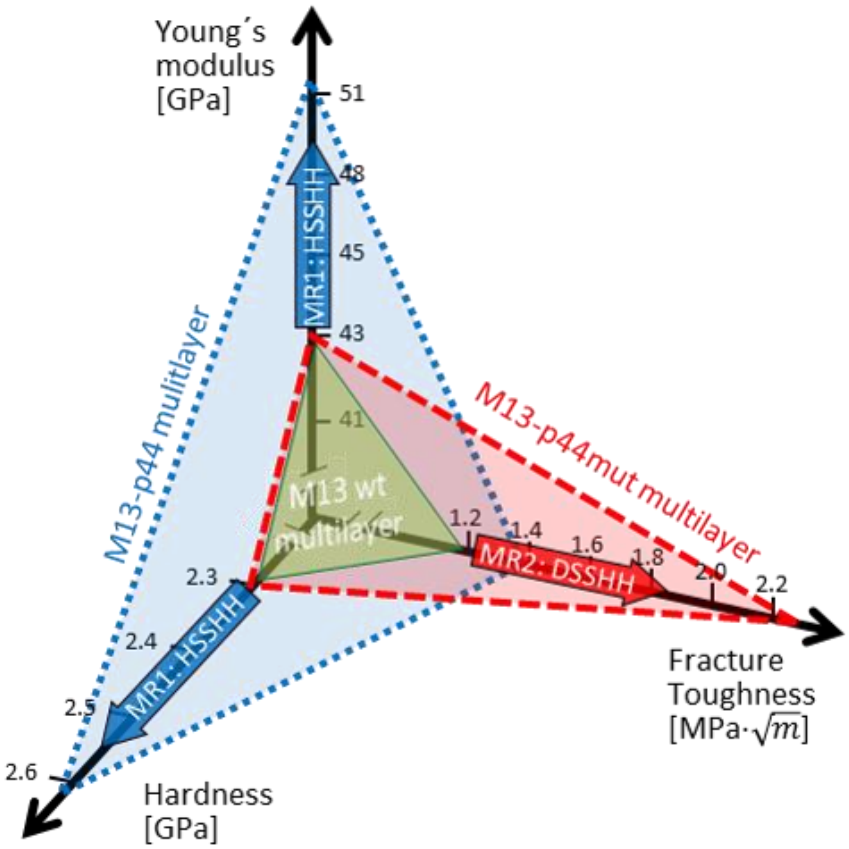

Figure 3. Tailoring the mechanical properties of phage-templated multilayer assemblies based on ceramic materials. Although, bioinspired composite materials show efficient mechanical performance (M13 wt multilayer, green triangle) the application of genetically engineered phages with intrinsic molecular recognition (MR) of the inorganic phase allows for the further improvement. The phage template M13-p44 expressing the ZnO-binding sequence HSSHH enhanced the hardness and the Young´s modulus (blue triangle), while the point-mutated version (MR2: DSSHH) increased the fracture toughness without deterioration of the hardness and Young´s modulus (red triangle).

Most important, the increase in fracture toughness in M13-p44mut assemblies was not a trade-off with the hardness and Young's modulus as these values did not significantly deteriorate. Whereas in M13 wt multilayer systems with an unspecific ZnO interaction the crack deflection was only poorly pronounced (Figure 4C). This multilayer system shows that the architecture of the bioorganic-inorganic assembly plays a crucial role for the mechanical properties (multilayered vs. monolithic ZnO). However, tailoring the interface by molecular recognition of the inorganic phase allows major improvements and the precise control of specific mechanical properties (hardness vs. fracture toughness). This approach can also be transferred to other bioinspired hybrid material systems to tailor material properties. Moreover, in relation to biological research, it might be useful to deduce the correlations of

the bioorganic-inorganic interactions at interfaces of these artificial systems to biominerals and their evolutionary formation and adaption.

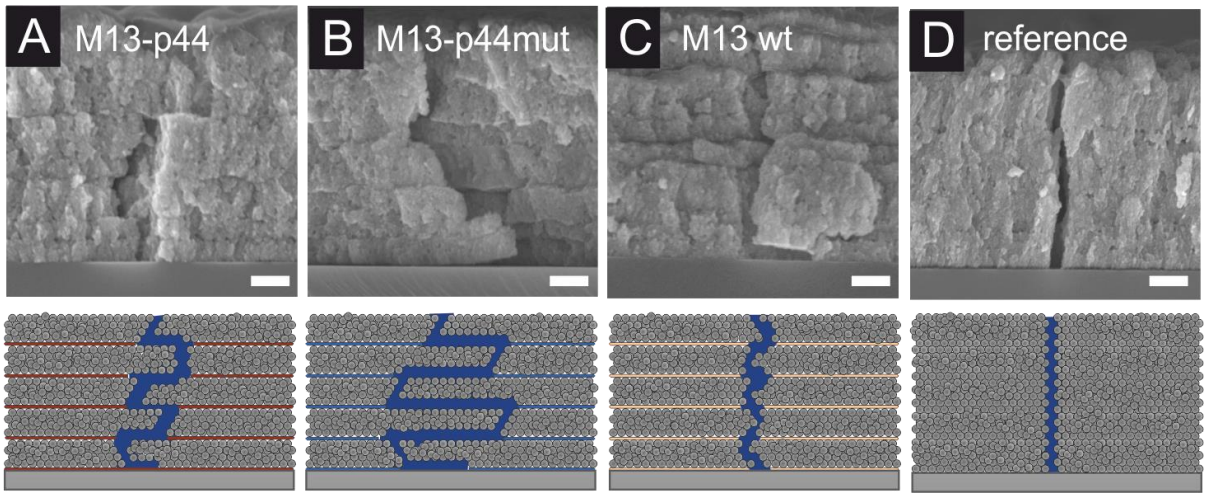

Figure 4. Fracture behavior in multilayer assemblies. Typical crack propagation in multilayer assemblies templated with A) M13-p44, B) M13-p44mut, C) M13 wt and monolithic reference samples D) missing a bioorganic interlayering. The M13-p44mut based multilayer revealed extensive crack deflection with the longest crack path vertical to the layered structure. This was followed by M13-p44. Samples based on M13 wt showed only minor crack deflection similar to the monolithic references, where almost no crack deflection was detectable. Scale bars: 200 nm.

3.4 Experimental Section

Genetically engineering of M13 bacteriophages

E. coli ER2738 and M13KE phage were purchased from New England Biolabs (NEB). The construction of the M13 p3-A3 phage displaying the gold-binding peptide A3 sequence AYSSGAPPMPPF[30] in p3 has been previously reported.[24] The inverse polymerase chain reaction (iPCR) method[31] was adapted to genetically engineer the M13-p44 phage by inserting the ZnO-binding motif (HSSHH) into the M13 p3-A3 phage major coat protein p8. Two partially complementary oligonucleotides were designed to insert HSSHH into the p8 coat proteins: 5'-CAT TCG TCG CAT CAT GGT GAG GGT GAC GAT CCC GCA AAA GCG GCC-3´ and 5´-ACC ATG ATG CGA CGA ATG AGC AGC GAA AGA CAG CAT CGG AAC GAG-3´. To generate the M13-p44 phage displaying the ZnO-binding motif (HSSHH) in p8 a PCR reaction was performed with the above oligonucleotides using the M13 p3-A3 phage[24] as a template. The obtained PCR product was gel extracted and amplified again using the same PCR parameters to increase the efficiency of mutagenesis. The obtained PCR product was purified on an agarose gel and re-circularized by ligation overnight at 16 °C using T4 DNA ligase (Thermo Scientific). The ligated DNA vector was then transfected into competent cells of *E. coli* ER2738 by heat-shock and plated onto LB agar plates containing IPTG and X-GAL after mixing with a top agar. Phage plaques were selected and analyzed by DNA sequencing.

M13-p44mut phage presenting a DSSHH motif at the N-terminus of every copy of p8 were constructed using iPCR as described above.

Phage amplification and purification

To amplify the phages for further experiments, the obtained phage stocks were used for infection of a 200-ml culture of *E. coli* ER2738 cells. Subsequently, the infected cells were grown overnight at 37°C and 180 rpm in 2xYT medium (pH 7.4). After the overnight culturing, *E. coli* cells were removed from the culture by centrifugation at 8000 rpm for 20 min. The supernatant was collected, and a 20% PEG 6000/2.5 M NaCl solution was added and incubated for 5 h at 4 °C to precipitate the phages. The phages were then centrifuged (8000 rpm, 20 min) and the pellet redissolved in 30 ml of 1x Tris buffered saline (TBS, pH 7.4). The phages were precipitated a second time to obtain higher purity. The precipitated phages were diluted to 1-5 x 10^{13} pfu/ml either in 5 mM Tris buffer (pH 8.0) or in 5 mM sodium phosphate buffer (pH 7.2) or in ddH_2O and stored at 4 °C after quantification by UV-Vis spectrometry.[32]

Si-wafer preparation

All films were deposited on p-doped silicon (001) wafer (Siltronic AG, Germany) cut to 10 x 10 mm^2 pieces. The substrates were cleaned in a sequential cleaning process with 10 min ultrasonication in ddH_2O, 10 min ethanol/acetone (1:1 v/v), 10 min oxygen plasma with 30 W (Plasma Prep2, Gala Instrumente, Germany) and finally 10 min ultrasonication in ddH_2O. Between the single cleaning steps, the samples were dried with nitrogen.

Template alignment with convective assembly

In order to generate a homogenous template layer convective assembly was performed. Briefly, a Si-wafer substrate was moved under a deposition plate with a constant velocity to homogenously align the phage in solution. The deposition plate was mounted horizontally with respect to the substrate under a certain angle (~ 33°). Due to hydrophilic interactions, the phage solution was withdrawn with the deposition plate resulting in a complete coverage of the substrate. In this report, a computer controlled dip coat engine (KSV Instruments, Finland) ensured continuous motion of the substrate at desired speed rates. All alignments were performed under controlled environmental conditions (23 °C ± 2 °C and 35 % ± 2 % relative humidity) applying 2.5 µl of M13 phage solution with concentrations between 1.2 to $2.0 \cdot 10^{13}$ pfu/ml per 10 mm x 10 mm. The traction speed of the substrate as well as the concentration and the pH of the phage solution were adjusted to achieve a homogenous alignment of M13 phage on the substrate (Supplementary **Table S4**). No salt precipitations were observed in any of the aligned samples.

Bioinspired zinc oxide (ZnO) mineralization

The mineralization of zinc oxide (ZnO) was performed according to Stitz *et al.*.[20] Briefly, stock solutions of 25.71 mM polyvinylpyrrolidone (PVP, Mw = 10,000 g·mol−1, LOT# BCBJ4889V, Sigma-Aldrich), 37.42 mM zinc acetate ($ZnAc_2$, $Zn(CH_3COO)_2 \cdot 2H_2O$, puriss p.a., ACS reagent, ≥99.0%, Sigma-Aldrich) and 75 mM tetraethylammonium hydroxide (TEAOH, 1.5 M in methanol, Sigma-Aldrich) in methanol (VLSI Grade, J. T. Baker) were prepared. The mineralization solution was prepared by mixing the stock solutions in a volume ratio of 1:1:1. First, $ZnAc_2$ and PVP were mixed followed by dropwise adding of TEAOH with a peristaltic pump (Ismatec ISM831A, Germany) at a flow rate of 1.047 ml/min under continuous stirring. The mineralization solution was prepared freshly before use. For the ZnO deposition, 20 µl of

ddH_2O were mixed with 980 µl of the mineralization solution in a glass vessel. The substrates were placed into the glass vessel and incubated in an oil bath at 60°C for 1.5 h. Afterwards the samples were washed extensively in methanol and dried with nitrogen. To increase the thickness of the ZnO-layer six cycles were carried out by using fresh solution and new vessels for each cycle.

Multilayer formation

Multilayer assemblies of alternating M13 phage and ZnO layers were generated with the described procedures for template alignment and mineralization consecutively until the desired number of layers was achieved, in general ten M13/ZnO double layers. To avoid additional water in the mineralization process, the samples were dried after convective assembly for a few hours at room temperature. Reference samples of monolithic ZnO films with the same layer thickness were produced. Therefore, the same number of ZnO deposition cycles was applied as for the multilayer formation.

Phage alignment

The alignment of the M13 phage on the Si-wafer was imaged with an atomic force microscope (AFM) (Digital Instruments MultiMode 8 with a NanoScope 5 controller, Bruker) operated in tapping mode. Typically, 3 µm x 3 µm areas at three different positions on the substrate were scanned.

Multilayer assemblies and reference ZnO layers

Cross-sectional analysis of the M13/ZnO multilayer assemblies was carried out with scanning electron microscopy (SEM, Zeiss Merlin) at an acceleration voltage of 3kV. Samples were sputtered with 0.3 nm iridium. The roughness of the organic template and the ZnO top layers were determined by AFM (Digital Instruments MultiMode 8 with a NanoScope 5 controller, Bruker). For each sample, 5 µm x 5 µm areas were scanned and the root-mean-squared roughness was determined (Nanoscope Analysis 1.5). The crystallographic analysis of ZnO was performed with a Θ-2Θ-diffracometer equipped with a cobalt-anode in the 2Θ range from 30° to 60°. To avoid strong Si reflexes samples were measured under a χ-angle of 10°. The average ZnO crystallite size was determined by XRD and calculated by applying the Scherrer equation:[33]

Equation 1: $D_{hkl} = \frac{K\lambda}{(B_{hkl}cos\theta)}$.

Where D_{hkl} ist the average crystallite size, K is the shape factor (0.89), λ is the K_α –wavelength of the x-ray source, B_{hkl} is the full width half maximum of the reflex and ϑ is the position of the reflex.

Mechanical properties of multilayer assemblies and reference ZnO layers

The mechanical performances of the multilayered and reference samples were tested by nanoindentation (Nanoindenter XP, Keysight) with a pyramidal Berkovich tip.[34] The nanoindentation was performed in continuous stiffness measurement mode using depth-controlled operation. The applied parameters for the nanoindentation experiment are listed in Supplementary **Table S5**. To avoid influences of the surface roughness and the substrate the nanoindentation data were evaluated in the contact depth range between 10 % and 20 % of the total assembly thickness.[10] For evaluation 75 indentation experiments on every sample were performed and only curves in accordance with the theory[35] have been chosen for calculation of the mean values.

The fracture behavior was evaluated by crack length analysis and SEM cross section images of fractured samples. A layer edge was etched with 0.5 M HCl in the thin films while the rest of the sample was protected by a photoresist. Several cracks at a substrate/sample interface were produced using a micro-hardness tester equipped with a Vickers-tip at three loads of 100 gf, 300gf and 500 gf. Minimum three crack pattern per sample and load were investigated. The fracture toughness was calculated according Xia et al.[36] with the premise that the crack in the thin film is shorter than in the pure substrate:

Equation 2: $K_c = \left\{ K_S^2 \left[1 + 0.45 \frac{(\phi b - a)}{t} \sqrt{\frac{E_c}{E_s} \frac{(1-\nu_s^2)}{(1-\nu_c^2)}} \right]^2 \right\}^{\frac{1}{2}}$

Where Kc is the fracture toughness of the coating, Ks is the fracture toughness of the substrate (silicon 0.83 $\mathrm{MPa} \cdot \sqrt{m}$),[10] ϕ is the slope of the plot a versus b for different loads, b is the crack length into pure substrate, a is the crack length in the film/substrate system, $E_{c/s}$ are the Young's moduli of the film and the substrate (163 GPa)[10] respectively, $\upsilon_{s/c}$ are the Poissons ratios of the film (0.25)[10] and the substrate (0.22),[10] respectively and t is the film thickness. The calculation of ϕ was based on the indents at 100 gf, 300 gf and 500 gf. While Kc was calculated based on the indents at 500 gf located at a distance s of ~ 30 µm from the multilayer edge. Due to the same structure of the templates and the same architecture of the multilayers,

e.g. the layer thickness, the structure, and the ZnO particle size, the intrinsic stress distribution for all multilayer samples was assumed similar. Therefore, the second term of the original method, which affects the absolute values of the fracture toughness, was neglected. However, the relative comparison between the multilayer assemblies is still valid.

3.5 Supporting Information

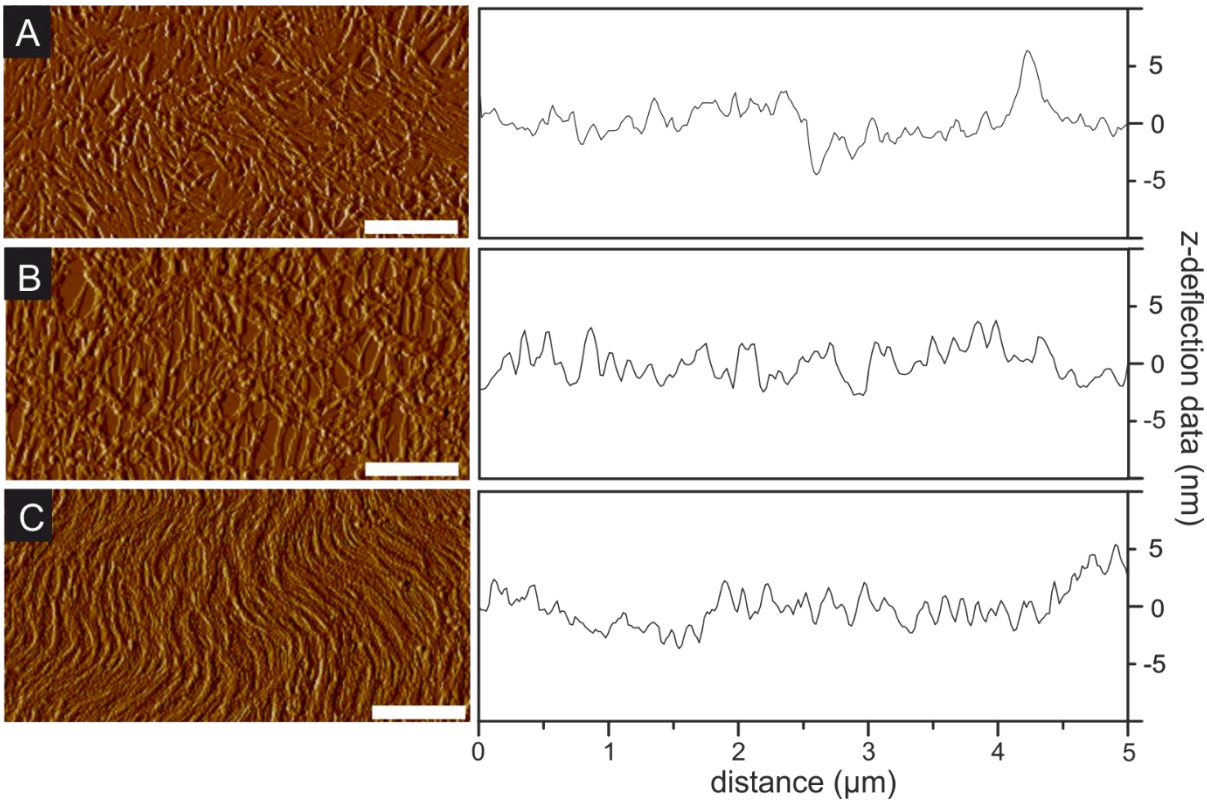

Figure S1. Alignment of M13 phage biotemplates on Si-wafer substrates for the generation of ZnO multilayer assemblies and corresponding z-deflection data. A) M13-p44 phage, B) M13-p44mut phage and C) M13 wild type (wt) phage. Scale bars: 1 µm.

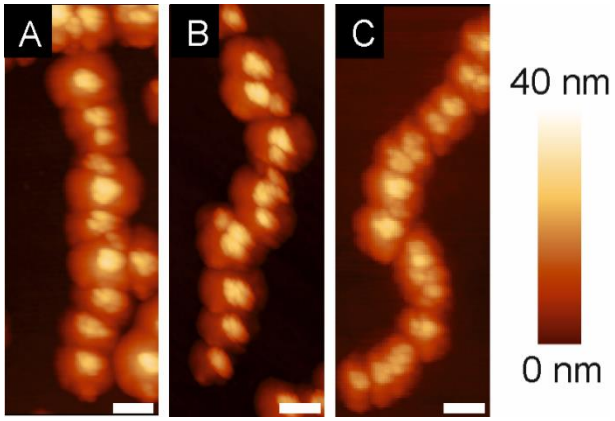

Figure S2. Influence of various M13 phage templates on coating thickness after one ZnO mineralization cycle measured by AFM. A) M13-p44, B) M13-p44mut and C) M13 wt. Scale bars: 100 nm.

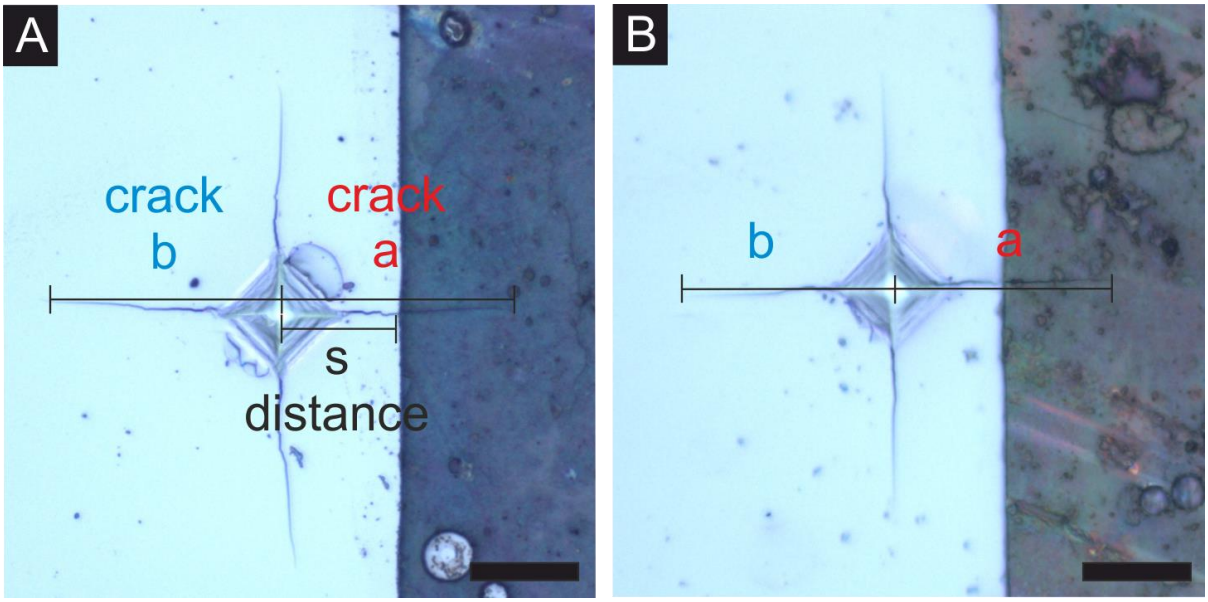

Figure S3. Comparison of the fracture behavior of multilayer assemblies and monolithic ZnO layers. Edges in multilayer assemblies and monolithic ZnO were prepared (dark area multilayer / ZnO, bright area Si-wafer substrate). A) The crack length “a” in the M13-p44 multilayer assembly is shorter than the crack “b” in the underlying Si-wafer substrate. B) The crack length “a” in the monolithic ZnO layer is longer than the crack “b” in the underlying Si-wafer substrate. Scale bars: 20 µm.

Table S1. Properties of the phage template surface with regard to the peptides fused to the major coat protein p8. The isoelectric point (pI) of M13 phage, which is ~ 4.2, was changed by the surface expression of the additional peptides. The pI of the peptides was calculated with Protein Calculator v3.4. Histidines (H) may carry a positive charge depending on the pH, therefore values are given only in brackets. Amino acids (AA) in the peptide sequences are depicted in single letters. The possible ZnO-interacting points were based on NMR studies reported in previous work.[5]

Biotemplate	Peptide	Positively charged AA	Negatively charged AA	Possible ZnO-interacting points	pI
M13-p44	HSSHH	(3)	0	11	7.56
M13-p44mut	DSSHH	(2)	1	9	6.48

Table S2. Influence of various M13 phage templates on coating thickness after one ZnO mineralization cycle. Deposition of ZnO was performed on single M13 phages immobilized on a Si wafer. The phage template did not influence the ZnO growth kinetics, which is reflected by the same hybrid height. The height was measured on 10 single phages by AFM.

Biotemplate	Thickness (nm)
M13-p44	26.9 ± 4.7
M13-p44mut	27.4 ± 4.5
M13 wt	27.2 ± 6.3

Table S3. The amount of the phage templates and the inorganic phase in the multilayer assemblies. Structural data were collected from three independent samples at five measuring points in SEM cross section samples. Hence, each thickness value is based on 15 measurements. By subtracting the single ZnO-layer thicknesses from the overall sample height the amount of the organic layer was determined.

Biotemplate	Film thickness (nm)	Single ZnO layer thickness (nm)	Calculated single M13 layer thickness (nm)	Calculated organic content based on thickness ratio (%)
M13-p44	1140 ± 136	107 ± 13	6.82 ± 0.17	5.98 ± 0.15
M13-p44mut	1110 ± 195	104 ± 19	6.40 ± 0.01	5.77 ± 0.01
M13 wt	1180 ± 38	110 ± 5	7.29 ± 0.62	6.17 ± 0.52

Table S4. Alignment parameters for convective assembly of the different types of M13 phage templates.

Biotemplate	Withdraw speed	solvent	concentration
M13-p44	0.9 mm/min	5 mM Tris buffer, pH 8.0	$1.2 \cdot 10^{13}$ pfu/ml
M13-p44mut	0.6 mm/min	5 mM Na-phosphate buffer, pH 7.25	$2.0 \cdot 10^{13}$ pfu/ml
M13 wt	1.2 mm/min	ddH_2O, pH 7.0	$2.0 \cdot 10^{13}$ pfu/ml

Table S5. Parameters for the continuous stiffness measurement of multilayer assemblies.

Variable name	Value
Surface approach velocity	15 nm/s
Surface approach distance	1000 nm
Surface approach detection stiffness	100 N/m
Strain rate	0.05 1/s
Harmonic displacement	2 nm
Frequency	45 Hz
Depth limit	350 nm – 500 nm
Surface stiffness	160 N/m
Poisson ratio	0.25 (assumption)
Distance between the indents (in x- and y-direction)	10 µm – 20 µm

3.6 Acknowledgements

The authors are grateful to the Nanostructuring Lab Weis (MPI FKF) for the possibility to use SEM equipment, the Department Mittemeijer (MPI IS) for access to Vickers micro-Indenter and light microscope, and the Department Spatz (MPI IS) for Nanoindenter and AFM equipment. The authors especially want to thank Maritta Dudek of the Department Mittemeijer (MPI IS) for performing the XRD-measurements. We also thank Jan Klenk and Tina Strobel (University of Stuttgart, Stuttgart, Germany) for preparing the phage solutions. Financial support by the Deutsche Forschungsgemeinschaft (DFG, SPP 1569) and the Baden-Württemberg (BW) Stiftung is highly appreciated.

3.7 References

[1] Carole C. Perry, Siddharth V. Patwardhan, O. Deschaume, Biochemical Society Transactions 2009, 37, 687.

[2] E. Zolotoyabko, Advanced Materials Interfaces 2017, 4, 1600189.

[3] J. L. Arias, M. S. Fernandez, Chem Rev 2008, 108, 4475; A. Rao, H. Cölfen, in *Biomineralization and Biomaterials*, (Ed: M.-P. Ginebra), Woodhead Publishing, Boston 2016, 51.

[4] S. V. Patwardhan, G. Patwardhan, C. C. Perry, J. Mater. Chem. 2007, 17, 2875.

[5] D. Rothenstein, B. Claasen, B. Omiecienski, P. Lammel, J. Bill, Journal of the American Chemical Society 2012, 134, 12547.

[6] M. A. Meyers, P. Y. Chen, A. Y. M. Lin, Y. Seki, Progress in Materials Science 2008, 53, 1.

[7] H. C. Schröder, F. Natalio, I. Shukoor, W. Tremel, U. Schlossmacher, X. H. Wang, W. E. G. Müller, J Struct Biol 2007, 159, 325; J. C. Weaver, L. I. Pietrasanta, N. Hedin, B. F. Chmelka, P. K. Hansma, D. E. Morse, J Struct Biol 2003, 144, 271; I. Sethmann, G. Wörheide, Micron 2008, 39, 209.

[8] U. G. K. Wegst, H. Bai, E. Saiz, A. P. Tomsia, R. O. Ritchie, Nat Mater 2015, 14, 23.

[9] W. E. G. Müller, H. C. Schröder, Z. Burghard, D. Pisignano, X. Wang, Chemistry – A European Journal 2013, 19, 5790.

[10] Z. Burghard, L. Zini, V. Srot, P. Bellina, P. A. van Aken, J. Bill, Nano Lett 2009, 9, 4103.

[11] M. E. Launey, E. Munch, D. H. Alsem, H. B. Barth, E. Saiz, A. P. Tomsia, R. O. Ritchie, Acta Materialia 2009, 57, 2919.

[12] P. Lipowsky, Ž. Burghard, L. P. H. Jeurgens, J. Bill, F. Aldinger, Nanotechnology 2007, 18, 345707.

[13] L. B. Mao, H. L. Gao, H. B. Yao, L. Liu, H. Cölfen, G. Liu, S. M. Chen, S. K. Li, Y. X. Yan, Y. Y. Liu, S. H. Yu, Science 2016, 354, 107.

[14] M. Mirkhalaf, A. K. Dastjerdi, F. Barthelat, Nat Commun 2014, 5.

[15] F. Libonati, M. J. Buehler, Adv Eng Mater 2017, 19.

[16] Z. Liu, X. D. Wen, X. L. Wu, Y. J. Gao, H. T. Chen, J. Zhu, P. K. Chu, Journal of the American Chemical Society 2009, 131, 9405.

[17] Y. Peng, A. W. Xu, B. Deng, M. Antonietti, H. Colfen, J Phys Chem B 2006, 110, 2988.

[18] C. K. Thai, H. X. Dai, M. S. R. Sastry, M. Sarikaya, D. T. Schwartz, F. Baneyx, Biotechnology and Bioengineering 2004, 87, 129; K. Kjaergaard, J. K. Sorensen, M. A. Schembri, P. Klemm, Appl Environ Microb 2000, 66, 10; M. M. Tomczak, M. K. Gupta, L. F. Drummy, S. M. Rozenzhak, R. R. Naik, Acta Biomater 2009, 5, 876; M. Umetsu, M. Mizuta, K. Tsumoto, S. Ohara, S. Takami, H. Watanabe, I. Kumagai, T. Adschiri, Advanced Materials 2005, 17, 2571.

[19] P. Lipowsky, R. C. Hoffmann, U. Welzel, J. Bill, F. Aldinger, Advanced Functional Materials 2007, 17, 2151.

[20] N. Stitz, S. Eiben, P. Atanasova, N. Domingo, A. Leineweber, Z. Burghard, J. Bill, Scientific Reports 2016, 6, 26518.

[21] J. Rong, Z. Niu, L. A. Lee, Q. Wang, Current Opinion in Colloid & Interface Science 2011, 16, 441; S. P. Wargacki, B. Pate, R. A. Vaia, Langmuir 2008, 24, 5439; D. M. Kuncicky, R. R. Naik, O. D. Velev, Small 2006, 2, 1462.

[22] W. O. Salivar, H. Tzagoloff, D. Pratt, Virology 1964, 24, 359.

[23] P. Moghimian, S. Kilper, V. Srot, D. Rothenstein, S. J. Facey, B. Hauer, J. Bill, P. A. van Aken, Int J Mater Res 2016, 107, 295.

[24] D. Rothenstein, S. J. Facey, M. Ploss, P. Hans, M. Melcher, V. Srot, P. A. v. Aken, B. Hauer, J. Bill, Bioinspired, Biomimetic and Nanobiomaterials 2013, 2, 173.

[25] L. Chen, Y. Wu, Y. Lin, Q. Wang, Chemical Communications 2015, 51, 10190.

[26] J. S. Koehler, Physical Review B 1970, 2, 547; S. H. Kim, Y. J. Baik, D. Kwon, Surface and Coatings Technology 2004, 187, 47.

[27] Z. Burghard, A. Tucic, L. R. H. Jeurgens, R. C. Hoffmann, J. Bill, F. Aldinger, Advanced Materials 2007, 19, 970.

[28] I. N. Martev, D. A. Dechev, N. P. Ivanov, T. S. D. Uzunov, E. P. Kashchieva, Journal of Physics: Conference Series 2010, 223, 012019.

[29] F. Barthelat, C. M. Li, C. Comi, H. D. Espinosa, J Mater Res 2006, 21, 1977; R. O. Ritchie, Nat Mater 2011, 10, 817.

[30] R. R. Naik, S. J. Stringer, G. Agarwal, S. E. Jones, M. O. Stone, Nature Materials 2002, 1, 169.

[31] D. Qi, K. B. G. Scholthof, J Virol Methods 2008, 149, 85.

[32] G. P. Smith, Vol. 2017.

[33] U. Holzwarth, N. Gibson, Nature Nanotechnology 2011, 6, 534.

[34] W. C. Oliver, G. M. Pharr, J Mater Res 1992, 7, 1564.

[35] X. D. Li, B. Bhushan, Mater Charact 2002, 48, 11.

[36] Z. Xia, W. A. Curtin, B. W. Sheldon, Acta Materialia 2004, 52, 3507.

4 Genetically Induced *In situ*-Poling for Piezo-Active Biohybrid Nanowires

Stefan Kilper, Timotheus Jahnke, Marc Aulich, Zaklina Burghard, Dirk Rothenstein, and Joachim Bill*

Abstract

Polycrystalline piezo-active materials only exhibit a high macroscopic piezo-response, if they consist of particles with oriented crystal directions and aligned intrinsic dipole moments. For ferroelectric materials the post-synthesis alignment of the dipoles generally is achieved by electric poling procedures. However, there are numerous technically interesting non-ferroelectric piezo-active materials like zinc oxide (ZnO). These materials demand the alignment of their intrinsic dipoles during the fabrication process. Therefore, in situ-poling techniques have to be developed. This study utilizes genetically modified M13 phage templates for the generation of force fields, which directly control the ZnO dipole poling. By genetic modification of M13 phage template, the piezoelectric response of the ZnO/M13 phage hybrid nanowire is doubled compared to the hybrid nanowire based on unmodified M13 wild type (wt) phage templates. Thus, the formation of piezo-active domains consisting of oriented ZnO nanocrystals is directly induced by the genetic modification. By the combination of the fiber-like structure of individual M13 phages with the bio-enhanced electromechanical properties of ZnO, hybrid nanowires with a length of ~ 1.1 µm and a thickness of ~ 63.5 nm have been fabricated with a high piezoelectric coefficient of up to $d_{33} = 7.8\ \mathrm{pm\ V^{-1}}$ for genetically modified M13 phage templates.

Kilper *et al.* Adv. Mater. 2019, 31, 1805597, Copyright © 2018 by John Wiley Sons, Inc.
Reprinted with permission of John Wiley & Sons, Inc

4.1 Main Text

Piezoelectric materials are an integral part of various devices, like smartphones, cars or lab-on-a-chip enabling motion[1] and pressure sensing[2] or microfluidic handling[3], respectively. For the development of next-generation electronic devices, a further miniaturization of such systems is aimed. Therefore, novel material systems and fabrication routes are needed.[4]

In piezo-active materials, mechanical energy is directly converted into electrical energy. The mechanical deformation changes the electrical polarization of the material, which generates an electrical current.[5] Polycrystalline piezo-active materials can be classified in (i) ferroelectric and (ii) non-ferroelectric materials. In both classes, a high macroscopic piezoelectric response, which is the average over all crystallites, is connected with the polar axes of the crystallites parallel aligned and with the same force direction.[6, 7] In ferroelectric materials the direction of the polar axes can be permanently aligned post-synthesis by a strong electric field, which is referred as poling.[6] However, the non-ferroelectric piezo-active materials, like zinc oxide (ZnO), gallium nitride (GaN), beryllium oxide (BeO) or cadmium sulfide (CdS), do not allow the reorientation of the polar axes. In such materials, the maximum piezoelectric response of a crystallite is linked to one of its crystallographic axis (**Figure 1 a**), which cannot be aligned post-synthesis.[5, 8] In piezo-active materials the polarization is connected to the ordered alignment of electrical dipoles.[9] In order to synthesize piezo-active non-ferroelectric materials either the direction of crystal growth has to be controlled[10] or the crystallite dipoles have to be aligned in a freely moveable state, e.g. in solution.

To influence the deposition of inorganic materials, template structures inducing a force field were reported. Various template classes, e.g. polyelectrolytes,[11] peptides[12] or biological entities, like viruses[13] and phages,[14] have been applied to control the morphology[15] of the inorganic phase or the mechanical performance of the hybrid material.[16] For such bioinspired synthesis approaches, M13 phage templates are of specific interest. M13 phages are non-pathogenic for humans and provide a nanowire-like structure (6 x 900 nm^2), which is precisely replicated in bacteria. The phage particles are robust and resistant to heat (> 80 °C), mechanical stresses and various solvents.[17] The protein coat, encapsulating the DNA genome, consists of five different proteins (p3, p5, p7, p8 and p9), which can be modified. The major coat protein p8 has dipole character with a positively charged C-terminus, interacting with the phage DNA and a negatively charged N-terminus facing the environment.[18] Due to the non-

centrosymmetric arrangement of the p8 proteins, which are helically arranged around the central DNA strand, the M13 phage template represents a net dipole.[19, 20] Moreover, the dipole strength can be further enhanced by the genetic modification of the major coat protein, which was shown in pure multi-phage assemblies arranged into piezoelectric films or pillar structures.[19, 21] Multi-phage assemblies have also been applied for the deposition of ferrolectric materials, which were calcinated (~1000 °C) and poled in an electrical field (up to 2 kV) for piezoactivity.[22]

Here, we present the in situ-poling of non-ferroelectric ZnO nanocrystallites by a phage template in a bioinspired synthesis approach resulting in a piezo active hybrid nanowire. The phage template was genetically engineered for an enhanced dipole moment in the major coat protein p8 inducing the poling of mineralized ZnO crystallites by the permanent alignment of initially freely movable ZnO dipoles. In the hybrid nanowires, the phage template induced the formation of aligned ZnO domains with piezoelectric properties. In a self-assembling process, individual phages were coated by chemical bath deposition (CBD) with polycrystalline ZnO layers under ambient conditions without any post treatment. The M13 phage template maintained its integrity in the soft biomineralization process, which allows determining the template effect on the material properties of the hybrid wires. Thereby, the M13 phage template controlled the degree of ZnO crystallite alignment. However, only the genetically modified M13-DD template, with the most pronounced dipole moment, efficiently induced the formation of aligned ZnO domains with high piezoelectric activity. A direct correlation of the piezo-activity and the genetic modification of the major coat protein was determined. This general effect of aligning crystallite dipoles with a dipole of an organic template, might also apply for other inorganic systems.

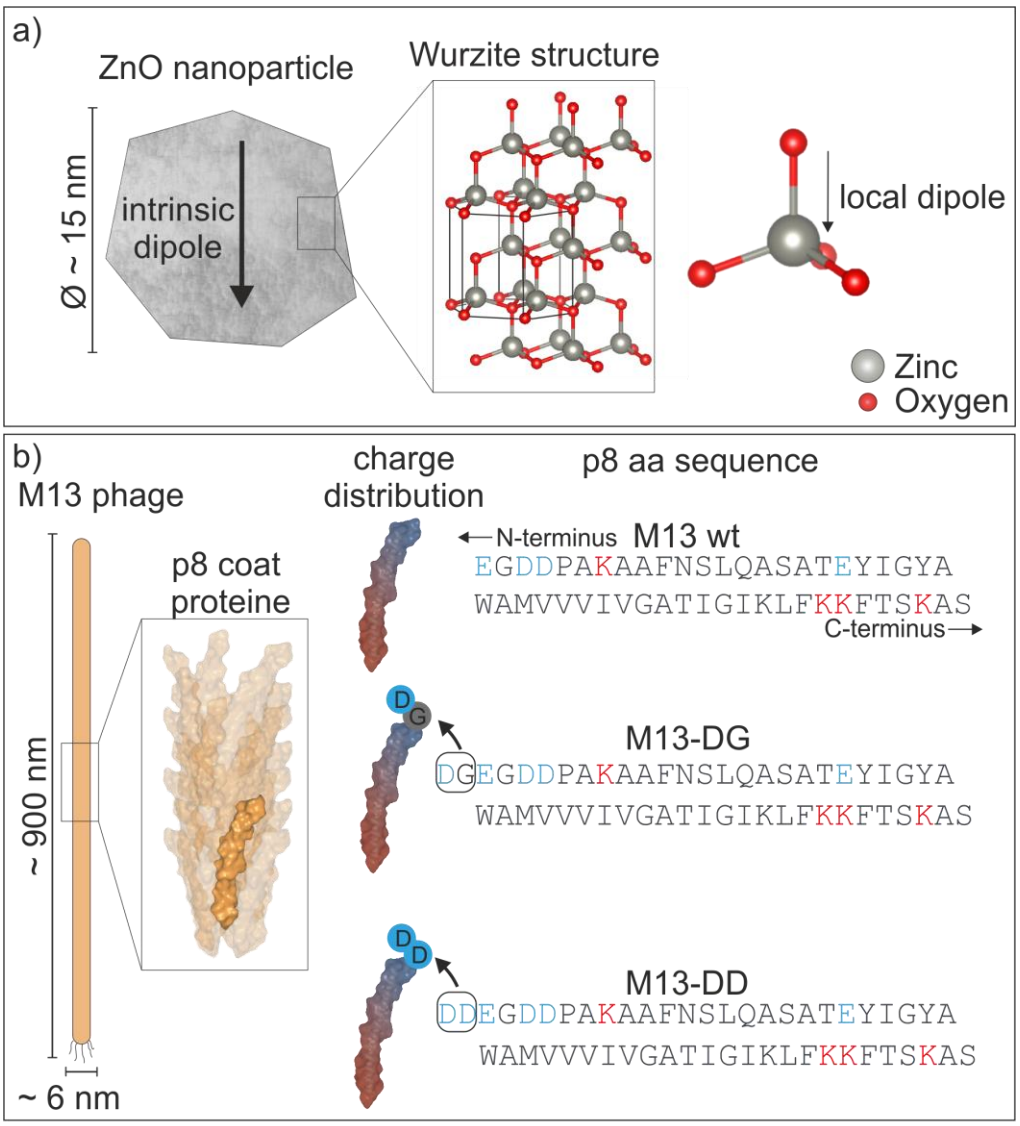

Figure 1 Inorganic and organic components of the biohybrid nanowires. a) Schematic structure of a zinc oxide (ZnO) nanoparticle and ZnO crystal structure ICSD 26170. Due to local dipoles along the c-axis each nanoparticle possess an intrinsic dipole moment. b) Schematic of the genetic engineering of M13 phages. The M13 phage body consist of 2700 copies of the major coat protein p8, due to their primary structure each molecule possess an intrinsic dipole. By addition of negatively charged amino acids the dipole moment is stepwise increased with one negative charge in M13-DG and two negative charges in M13-DD, respectively. In red positively, in blue negatively charged amino acids and protein regions are marked, respectively. (M13 phage subunit and p8 structure generated with Protein Workshop according to PDB reference: 2MJZ).[23]

For the bio-inspired mineralization of piezoelectric hybrid nanowires based on M13 phages, the phage template was genetically engineered for graduated dipole moments. The M13 DNA is encapsulated in a protein body, which is a well-ordered arrangement of approx. 2700 proteins, formed by the major coat protein p8.[24] By the addition of negatively charged amino acid residues at the p8 N-terminus, the natural dipole moment of the major coat protein can be further enhanced.[19, 21] In this report, the M13 phage templates were genetically engineered for a strong dipole moment in the p8 protein by the addition of two aspartic acid (D) residues at the N-terminus resulting in the M13-DD phage template. Moreover, M13-DG phage templates with an intermediate dipole moment were established by the fusion of DG (G = glycine), where glycine is a spacer in order to obtain phage mutants with the same number of added amino acid residues. As a reference, unmodified M13 phages (M13 wild type (wt)) were applied, which had the weakest intrinsic dipole moment in this study (Figure 1 b). The phage structure was not affected by the genetic modification and they specifically templated the deposition of ZnO nanocrystals (Figure 1 a) into a polycrystalline coating.[16] The hybrid wires were synthesized in a two-step procedure (**Figure S1 a**). First, 1-5 phage templates per 10 μm^2 were immobilized on Si-wafers and aligned in a nitrogen stream. In a second step, ZnO nanocrystals were synthesized in a chemical bath deposition (CBD) procedure under mild conditions. The hybrid wires did not need any post-synthesis treatment, like calcination, to enhance its material properties. To ensure a continuous ZnO coating, which was fundamental for an effective piezoelectric response, the CBD process was repeated five times. Hybrid nanowires were prepared with all three M13 phage-variants M13-DD, M13-DG and M13 wt. The ZnO growth rate per cycle of ~ 12 nm/cycle was not affected by the template resulting in an average thickness of ~ 63.5 nm (for details: **Table S1, Figure 2**). This also indicates that the interaction of further components of the mineralization solution i.e. polyvinylpyrrolidone (PVP) is not influenced by the mutation of the phage template. All hybrid nanowires had a length of ~ 1.1 µm, which was determined by the lengths of the M13 phage templates. Transmission electron microscopy (TEM) investigations showed ZnO crystallites with an average size of 14.7 ± 1.4 nm and the electron diffraction patterns revealed the polycrystalline nature of the ZnO coatings (Figure S1). These findings are in agreement with previously published x-ray diffraction (XRD) studies of phage-templated ZnO layers synthesized under the same conditions where the ZnO nanocrystalline layer consisted of the wurtzite modification

and the D_{hkl} coherence lengths of the nanocrystallites indicate a spherical shape, independent of the genetic modification of the phage template.[16]

The piezoelectric properties of the ZnO/M13 phage hybrid wires were determined by piezo force microscopy (PFM) allowing the simultaneous acquisition of (i) the sample topography, (ii) the out of plane piezoelectric response and (iii) the out of plane polarization direction. All hybrid nanowires templated on the M13 phages showed piezoelectric properties, reflected by the linear increase of the piezoelectric response with increasing the applied voltage V_{AC} (**Figure S2**). The slope of the linear regression corresponds to the effective piezoelectric coefficient d_{eff} and describes the out of plane piezoelectric response, which corresponds to $0.5d_{33}$ (**Equation 2**). The maximum piezoelectric response was attained with M13-DD templated nanowires with $d_{33} = 7.8\ \mathrm{pm\ V^{-1}}$ ($d_{\mathrm{eff}} = 3.9\ \mathrm{pm\ V^{-1}}$) for completely unipolar domains with an average area of $2.1 \cdot 10^{-14} \pm 5.8 \cdot 10^{-15}\ \mathrm{m^2}$. The overall piezoelectric responses of each hybrid system was determined as the mean value of at least 5 wires (area: $2.5 \cdot 10^{-13} \pm 3.4 \cdot 10^{-14}\ \mathrm{m^2}$) from two independent experiments. The piezoelectric response of the M13-DD templated hybrid wires was almost doubled compared to the values of the M13-DG and M13 wt templated systems. The overall piezoelectric response of M13-DD templated wires was $d_{33} = 5\ \mathrm{pm\ V^{-1}}$ ($d_{\mathrm{eff}} = 2.5 \pm 0.8\ \mathrm{pm\ V^{-1}}$) (Figure 2 d). The d_{33} values of the M13-DG and M13 wt templates were perceptible lower with $d_{33} = 2.6\ \mathrm{pm\ V^{-1}}$ ($d_{\mathrm{eff}} = 1.3 \pm 0.6\ \mathrm{pm\ V^{-1}}$) for M13-DG and $d_{33} = 2.6\ \mathrm{pm\ V^{-1}}$ ($d_{\mathrm{eff}} = 1.3 \pm 0.3\ \mathrm{pm\ V^{-1}}$) for M13 wt. In pure monolayer phage assemblies on a cysteamine support the piezoelectric coefficient was reported for M13 wt to 0.3 ± 0.03 pm V^{-1} and for the phage with a similar charge distribution in the p8 like the M13-DD mutant to 0.7 ± 0.05 pm V^{-1}.[19] These piezoelectric coefficients of the pure monolayer phage films can be assumed higher compared to single phages because of interactions between phages in the assemblies and the immobilization on polar molecules (cysteamine).[19] Therefore, the piezoelectric coefficient of the hybrid nanowire of this work was mainly governed by the ZnO phase.

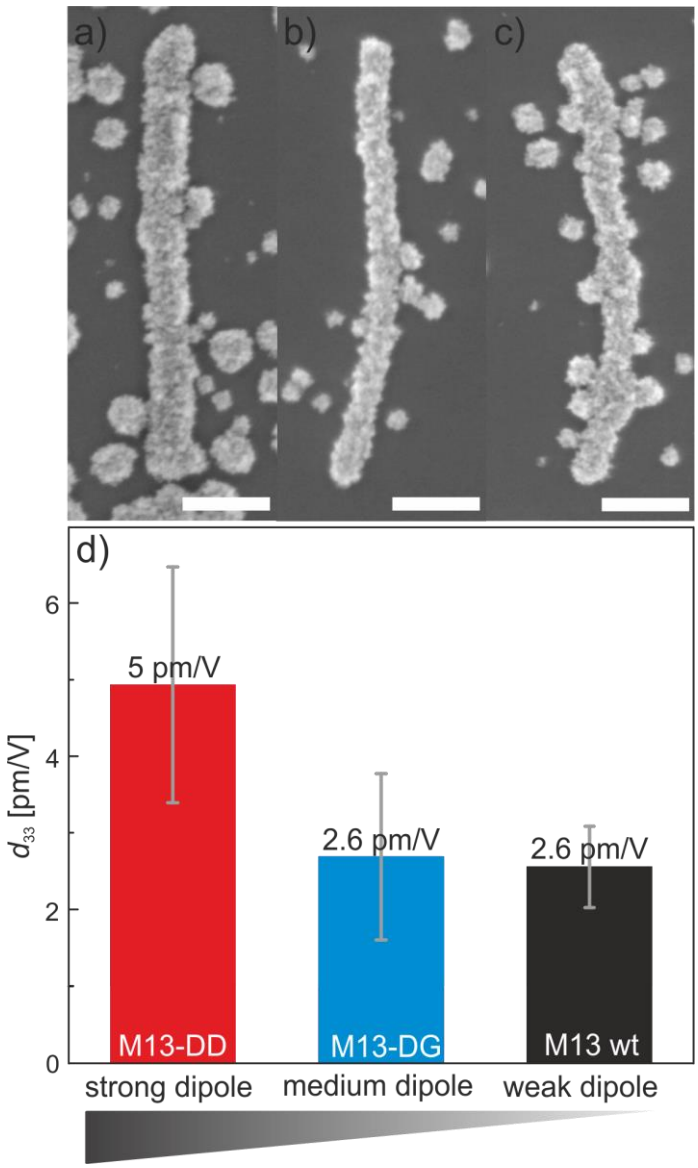

Figure 2 Zinc oxide coated phage templates. High resolution scanning electron microscopy (SEM) images and piezo-activity of the ZnO/M13 hybrid nanowires. a) M13-DD, b) M13-DG, and c) M13 wt. d) The Z-axis piezoelectric coefficients (d_{33}) were determined by piezo force microscopy (PFM) on five different hybrid fibers for each template type. The genetic modification of the M13-DD phage template (red) almost doubles the piezo response compared to the templates M13-DG (blue) and M13 wt (black). Scale bars 200 nm.

For the selective deposition of inorganic materials in templated CBD processes, electrostatic forces are discussed as one of the main driving forces.[25] However, in the CBD process, presented here, the dissociation of functional groups in methanol as solvent is strongly reduced.[13, 26] Furthermore, the zeta potential of non-mineralized M13-DD and M13 wt phage templates in aqueous buffer systems were measured. In the basic pH regime, which refers to the pH of the mineralization solution, the zeta potential showed no significant differences (**Table S3**). Hence, other influencing parameters than the long-range electrostatic interactions are supposed to control the alignment of the ZnO nanocrystals. Due to the crystal structure of hexagonal ZnO the oxygen-zinc bonds along the crystallographic c-axis are slightly elongated compared to the ideal tetrahedron, causing a local dipole moment in this direction (Figure 1 a).[8] Therefore, each ZnO nanocrystal represents a macroscopic dipole moment, which can be aligned on the template by dipole-dipole interactions.[27, 28] The PVP in the mineralization solution may facilitate this dipole alignment and assume various functions. PVP can control the ZnO growth to nanocrystallites[29] but may also act as a "lubricant" generating short-range repulsive forces inhibiting the fusion of nanocrystals and allowing the ZnO particles to achieve relative co-orientation.[28] As before mentioned, the macroscopic piezoelectric response of polycrystalline ZnO thin films is determined by the unipolarity of the ZnO dipole moments.[7, 30] However, the ZnO particle-to-particle interaction energetically favors an antiparallel aggregation of two neighboring intrinsic ZnO dipoles leading to the formation of a domain structure in the ZnO layers. The domain structure was also visualized in the PFM phase signal by bright and dark areas (**Figure 3**). The ratio between positive (z-axis component of the dipoles pointing away from the substrate) and negative domains (z-axis component of the dipoles pointing towards the substrate) can be applied as a measure for the degree of unipolarity.[30] Negative domains lead to negative and positive domains to positive in-phase signals, respectively.[31] The orientation direction of the domains in the hybrid wires was assessed by the average distribution function of the in-phase signal, based on three hybrid wires for each phage template variant (according to [32]). The non-piezoelectric silicon substrate served as an internal reference. ZnO domains with no z-axis piezoelectric response (dipole moment oriented parallel to the substrate surface) correspond to the zero value in the in-phase signal.

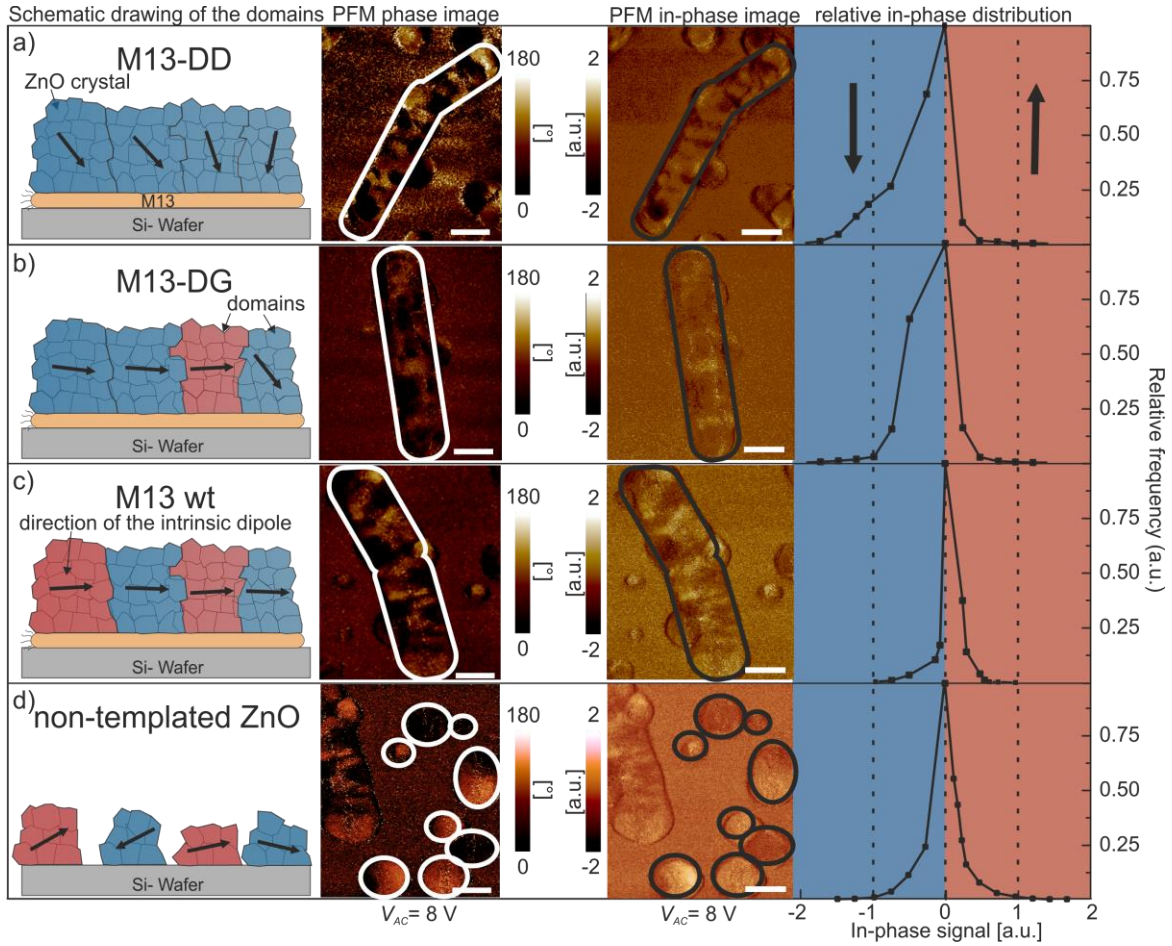

Figure 3 Induction of piezo-active domains in ZnO layers. Schematic drawing, Piezoforce microscopy (PFM) phase / in-phase images and its relative distribution function of a) M13-DD, b) M13-DG, c) M13 wt hybrid nanowires and d) non-templated randomly deposited ZnO particles. The **schematic drawing** indicates the direction of dipole moments in single domains of the ZnO polycrystalline layer. High piezoelectricity is associated with domains oriented orthogonal to the silicon wafer. Dark and bright areas in the **PFM phase** images indicate ZnO domains with different dipole moment directions. **PFM in-phase** images show the direction of the z-component of the intrinsic ZnO dipole moments. Scale bars are 200 nm. **Relative distribution function**. Evaluation of the direction of the dipole moments in a hybrid nanowire. The area below the curve is equivalent to the volume fraction negative (blue) and positive (red) domains, respectively.

The absolute values of the domain signals are a measure for the relative z-axis orientation of the domain dipole moments i.e. the stronger the in-phase signal the better the z-axis orientation. The in-phase signals were plotted over its relative frequency (Figure 3). In this plot, the area under the curve is a measure for the volume of positive (highlighted red) and negative (highlighted blue) domains. With this, the degree of unipolarity ξ can be calculated on the basis of the areas below the curves.[33] With an ideal unipolar single-domain crystal corresponding to ξ = 1 and an ideally random multi-domain crystal corresponding to ξ = 0. The

non-templated ZnO particles showed a symmetric distribution function close to the zero value resulting in a low value for the degree of unipolarity ξ = 0.1, which was close to the value for an ideally random orientation (Figure 3 d). The M13 wt phage template, without any genetic modification, has only a small effect on the alignment of the ZnO particles showing unipolarity degree of ξ = 0.4 (Figure 3 c). In contrast, the hybrid systems with both genetically modified M13 phage templates, M13-DD and M13-DG, display a significant volume fraction of negative domains (Figure 3 a and b) with unipolarity degrees of ξ = 0.6 and ξ = 0.5, respectively (**Table S4**). However, while the M13-DG hybrid system showed only a weak piezoelectric activity, the M13-DD based hybrid system had good piezoelectric properties. A detailed evaluation showed that 9.2 % of the M13-DD domains had an high z-axis orientation, reflected by in-phase signal values smaller than -1 a.u. while only 1.3 % of the M13-DG system showed values below -1 a.u.. This demonstrates that only the strongest intrinsic dipole moment, represented by the M13-DD phage template, is capable of effectively controlling the alignment of ZnO crystals and induce the formation of high piezoelectric ZnO nanowires where a post-synthesis poling is not possible. In contrast, piezo activity in hybrid systems based on phage assemblies and ferroelectric $BaTiO_3$ and PZT was achieved by a post-synthesis poling in an electrical field.[22] The piezoelectric coefficients of the M13-DD hybrid wire systems are remarkably high for polycrystalline structures with such a low thickness (63.5 nm) as the piezoelectric response of ZnO thin films dramatically decreases with decreasing film thickness [34].

M13 phage templates were genetically engineered for the in situ-poling of piezo-active ZnO hybrid nanowires. Hereby, the orientation of the intrinsic dipoles and hence polarization direction of the deposited ZnO nanocrystals was controlled by the genetic constitution of the template. The direct template-particle dipole-dipole interaction allowed a direct control of the degree of unipolarity, resulting in a high piezoelectric response. The unipolarity of the ZnO crystallites was increased by up to 600 % in phage templated nanowires. The overall piezoelectric response of the most effective ZnO nanowire was almost doubled from $d_{33} = 2.6\ \mathrm{pm\ V^{-1}}$ for the non-modified M13 wt phage to $d_{33} = 5.0\ \mathrm{pm\ V^{-1}}$ for the genetically enhanced M13-DD phage.

The genetic modification of the M13-DD phage template increased the intrinsic dipole moment of the major coat protein p8 resulting in a higher degree of unipolarity and z-axis orientation of the deposited ZnO nanocrystals. This effect leads to the strong increase in the piezoelectric response of the hybrid nanowires. The small dimensions of the hybrid wire

systems along with the remarkably piezoelectric properties demonstrate the importance of the in situ-poling process by genetically modified templates on the fabrication of novel piezoelectric biohybrid nanostructures.

4.2 Experimental Section

M13 phage genetic engineering

M13 phages were genetically engineered for the expression of additional aspartic acid (D) residues fused to the N-terminus of the major coat protein p8. The genetic modifications were performed in the M13KE genome background (New England Biolabs, NEB, USA). First, two restriction sites, flanking the N-terminus of the mature p8 coat protein, were created by inverse PCR techniques applying abutting oligonucleotides harboring the nucleotide changes (**Table S2**). The NcoI site at position 1353 – 1358 was introduced by the point mutations G1354C (no effect on amino acid level) and C1358G (leucine to valine exchange). The second restriction site, BamHI, was created at position 1381 – 1386 by the change C1381G, which resulted in the exchange of aspartic acid to glutamic acid. The modifications of the new M13-NB clone were determined by DNA sequencing with the -96 gIII primer (5´- CCC TCA TAG TTA GCG TAA CG – 3´). The M13-NB clone was infective and was amplified to wt M13 levels in E. coli ER2738.

DNA of M13-NB was isolated and purified with Plasmid Miniprep Kit (Peqlab) and digested with NcoI-HF and BamHI-HF (both NEB Biolabs) and gel purified. Two pairs of complementary oligonucleotides were designed introducing either one or two aspartic acid residues, respectively, at position 2 of the mature p8 protein (Table S2). The oligonucleotides had corresponding restriction sites for cloning into the M13-NB vector. Equal amounts of complementary oligonucleotides were mixed and annealed before the oligonucleotides were digested and purified according to the vector DNA. The insert was ligated into M13-NB with T4 DNA ligase (NEB Biolabs) and transformed into chemical competent E. coli ER2738. Single plaques were isolated and amplified in 4 mL LB medium for a phage stock and DNA isolation. The genetic modification of M13 phage was determined by DNA sequencing.

To amplify the phages for further experiments, the phage stocks were used for the infection of a 20 mL culture of a 1:100 diluted overnight E. coli ER2738 culture. Subsequently, the infected cells were grown 4.5 h at 37°C and 250 rpm in LB medium. Afterwards, the E. coli cells were removed by centrifugation at 8000 g for 10 min. The supernatant was mixed with 20% PEG-8000/2.5 M NaCl solution and incubated overnight at 4 °C. To collect the phages, the solution was centrifuged (10000 g, 15 min) and the pellet resuspended in 1 mL Tris buffered saline (TBS, pH 7.4). To increase the purity, the phages were precipitated a second time. The

precipitated phages were resuspended in 200 µL ddH_2O and stored at 4 °C. The phage solution was quantified by UV-vis spectrometry[35] or phage titering according to the manufacturers' recommendations.

M13 phage alignment by molecular combing

As a substrate for the single M13 phage templates 10 x 10 mm pieces of a p-doped silicon (001) wafer (Siltronic AG, Germany) were used. The substrates were cleaned by 10 min ultra-sonication in ddH_2O and ethanol/acetone in a volume ratio of 1:1 followed by 10 min oxygen plasma treatment with 30 W (Plasma Prep2, Gala Instrumente, Germany) and another 10 min ultra-sonication in ddH_2O. After each ultra-sonication step, the samples were dried using a nitrogen stream. For the deposition of single M13 phages a molecular combing approach was adapted. Briefly, 2.5 µl of M13 phage solution (concentration ~ $2.0 \cdot 10^{11}$ pfu/ml) were carefully placed in the middle of the substrate. After an incubation time of 60 s the residual solution was removed with a nitrogen stream. The nitrogen stream was conducted through a 12 mm wide flat nozzle mounted at an angle of 45° around 3 mm above the edge of the substrate with a nitrogen pressure of ~3.5 bar. Afterwards, the substrates were dried 1 h at 37 °C before starting the ZnO deposition.

Bioinspired zinc oxide (ZnO) mineralization

The chemical bath deposition process was conducted as previously described.[16] Briefly, the mineralization solution contained three different stock solutions in a volume ratio of 1:1:1. The previously prepared stock solutions of 37.42 mM zinc acetate dihydrate ($ZnAc_2$, $Zn(CH_3COO)_2{\cdot}2H_2O$ (puriss p.a., ACS reagent, ≥99.0%, Sigma-Aldrich), 25.71 mM polyvinylpyrrolidone (PVP, Mw = 10,000 g·mol−1, LOT# BCBJ4889V, Sigma-Aldrich) and 75 mM tetraethylammonium hydroxide (TEAOH, 1.5 M in methanol, Sigma-Aldrich) in methanol (VLSI Grade, J. T. Baker) were mixed following the hereinafter described procedure. First, the ZnAc2 and the PVP stock solutions were mixed, and then TEAOH was added dropwise at a flow rate of 1.047 ml/min with a peristaltic pump (Ismatec ISM831A, Germany) under continuous stirring. The ZnO deposition was performed in a 15 ml glass vessel with a lid, which was dried at 80°C for at least 2h. First 20µl of ddH_2O were added to the vessel, followed by 980µl of the mineralization solution and afterwards the substrates were placed in the vessel with the template-covered side facing upwards. The vessels were placed in a 60°C oil bath for 1.5 h, subsequently the substrates were washed thoroughly with methanol and dried with a

nitrogen stream. To reach a sufficient thickness of the ZnO layer on top of the organic template the deposition was performed five times per sample.

Structural characterization of the hybrid structures

The height and structure of the M13 phage templates before the deposition was investigated in contact mode with an atomic force microscope (AFM, Digital Instruments MultiMode 8 with a NanoScope 5 controller, Bruker, Germany) on at least 5 different M13 phages.

After ZnO deposition, the samples were investigated in contact mode AFM and additional surface scanning electron micrograph images were obtained with a scanning electron microscope (SEM, Zeiss Merlin, Carl Zeiss Microscopy GmbH, Germany) at an acceleration voltage of 1.5 kV.

Piezo force microscopy

The piezo force microscopy (PFM, Digital Instruments MultiMode 8 with a NanoScope 5 controller, Bruker, Germany) was performed in contact mode using electrical conductive AFM probes (SCM-PIT-V2, Bruker, Germany). The measurement is based on the reverse piezoelectric effect and therefore an AC electric field V_{AC}(20 kHz) with different amplitudes ranging from 0V to 8V in 2V steps was applied to the tip whilst scanning over the surface. The first Δz_ωharmonic signal of the vertical piezoelectric response signal was measured:[36]

$$\Delta z_\omega = d_{\text{eff}} V_{\text{AC}}$$

where d_{eff} is the effective piezoelectric coefficient. To convert the obtained AFM signals from mV to a height change in pm, the deflection sensitivity (nm V^{-1}) of each cantilever was determined before every measurement set. By plotting Δz_ω against the applied V_{AC} amplitudes the piezoelectric response can be derived according to the equation 1.

Due to the nanosized tip, which acts as top electrode, the applied AC electric field is inhomogeneous, thus Kalinin and Bonell[37] found that the correlation of d_{eff} piezoelectric coefficient d_{33} can be approximately described with:

$$d_{33} = 2d_{\text{eff}}.$$

X-cut quartz crystals ($d_{11} = 2.3\ \text{pm V}^{-1}$)[36] have been used as reference for the measured d_{eff} values. A value of 2.5 ± 0.5 pm V^{-1} was determined with three different AFM probes of the same batch at 5 measurement areas (10 μm^2), which is well in accordance to the given literature data.[36]

No significant charging effects of the silicon substrate were observed for the different applied voltages prove the effectiveness of the substrate as a bottom electrode. Additional information concerning the size and orientation of piezoelectric domains were obtained by recording the “phase” signal and “in-phase” signal, the latter corresponds to the real part of the complex lock-in-amplifier signal. Here, additionally periodically poled lithium (PPLN) was used as reference according to literature[31].

4.3 Supporting Information

Transmission electron microscopy of the hybrid wire system Transmission electron microscopy (TEM) investigations were performed at 200 kV (Philips Electronic CM200 Microscope) after cutting a lamella longitudinal to the ZnO/M13 hybrid wire axis using a focused ion beam (FIB).

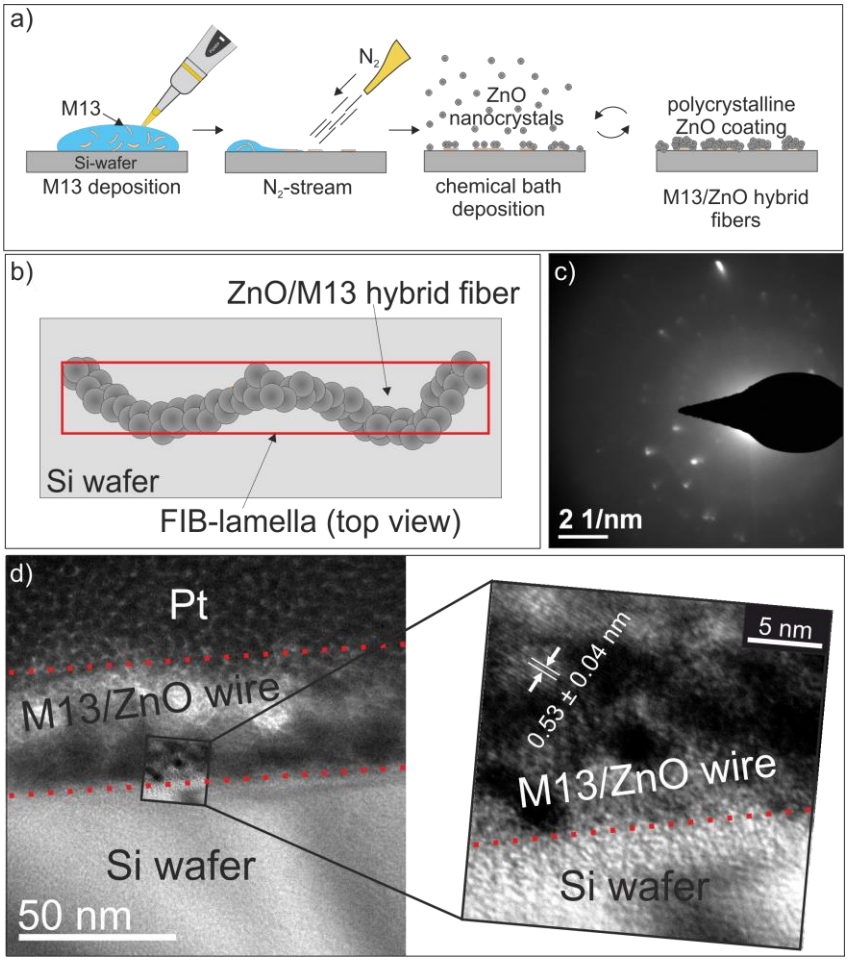

Figure S1 a) Schematic drawing of the nanowire fabrication process b) Schematic drawing of the cut FIB lamella. c) The SAED diffraction pattern displays the crystallinity of the ZnO layer. d) TEM cross section investigation along, the inset shows a higher magnification of a bottom part of the ZnO/M13 hybrid fiber. Not the complete height of the ZnO/M13 hybrid fiber is visible due to partial coverage with Pt. In the inset the determined lamella spacing of 0.53 ± 0.04 nm corresponds well with the c-axis of the wurtzite unit cell 0.521 nm (ICSD card no. 34477).

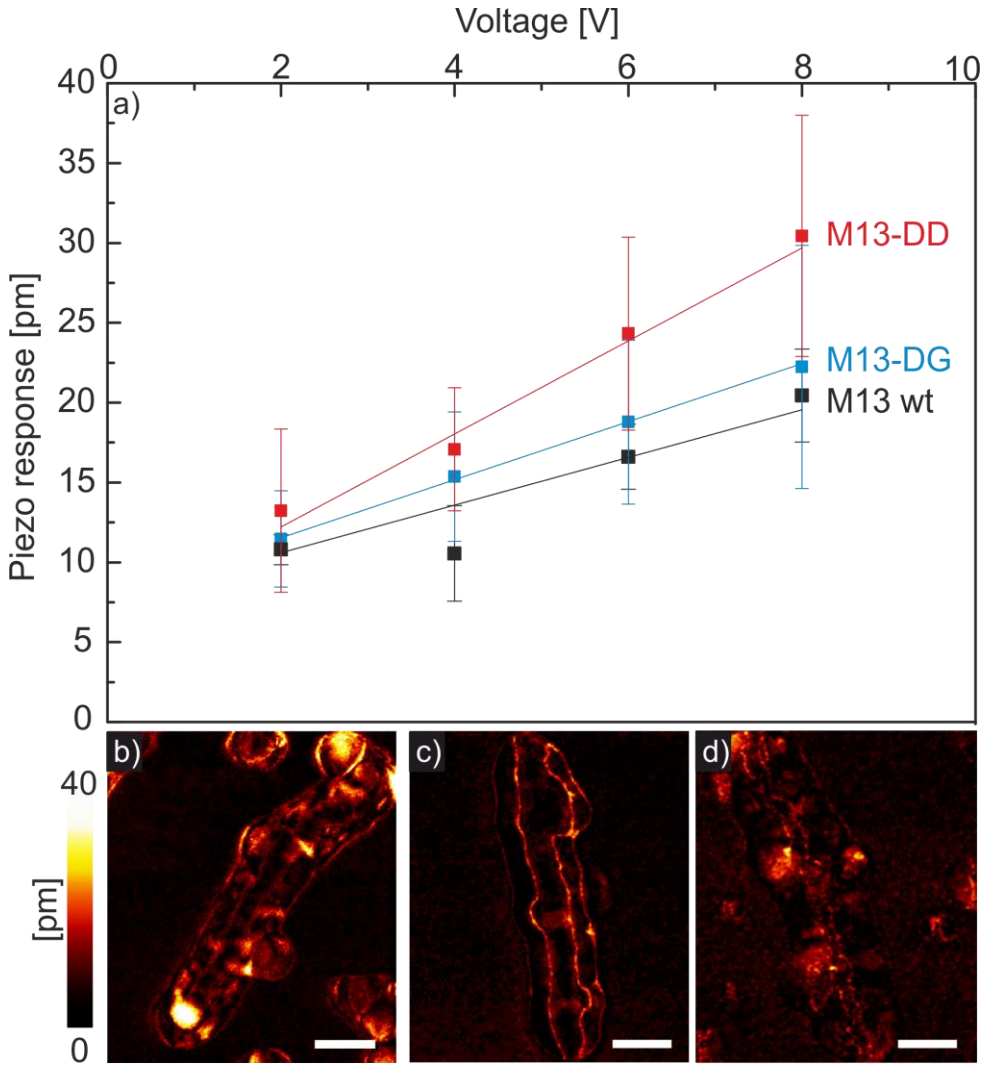

Figure S2 Piezo-activity in phage-templated nanowires. a) Piezo response in pm for 2 V, 4 V, 6 V and 8 V applied V_{AC}. The values of M13-DD are presented in red, of M13-DG in blue and of M13 wt in black color, respectively. Amplitude signals (V_{AC} = 8V) of b) M13-DD, c) M13-DG and d) M13 wt hybrid fibers. Scale bars 200 nm.

Piezo force microscopy signal description

In piezo force microscopy the calibration of the system with respect to the room coordinates is crucial for optimum measurement conditions. To identify the polarization direction of piezoelectric materials two preliminary considerations have to be taken into account. First the system inherent background has to be corrected by measuring a non-piezoelectric material (e.g. silicon or quartz glass) and second the signal coordinate system of the lock-in-amplifier has to be matched to the room-coordinates. In optimum measurement conditions, the in-phase signal of the lock-in-amplifier (real part) contains the complete z-axis piezo response. In reality there is always a small misalignment leading to a reduced in-phase signal. ZnO domains with the same color-coding as the substrate own polarization vectors, which are oriented parallel to the substrate surface. Domains, which display a negative or positive value in the in-phase signal, own polarization vectors oriented downwards or upwards,[31] respectively (**Figure S3**).

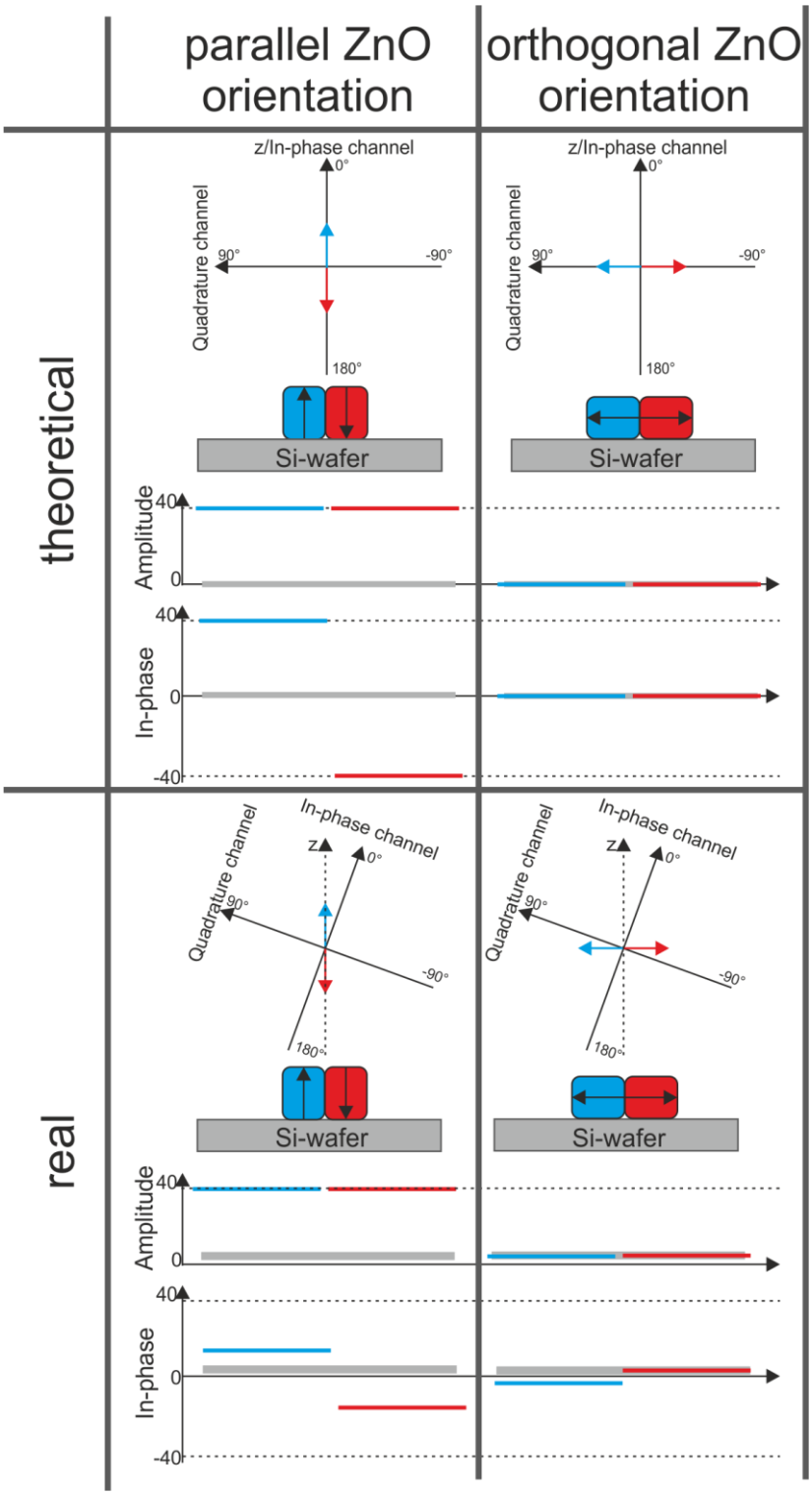

Figure S3 Schematic illustration of the signal coordinate-crystallite orientation alignment and the resulting amplitude and in-phase signal responses, respectively. The depicted conditions are idealized and already corrected for non-piezoelectric background contributions.

Table S1 Structural characterization of the zinc oxide / M13 phage (ZnO/M13) hybrid fibers. The fiber length and height after 5 mineralization cycles were determined by contact mode atomic force microscopy (AFM).

Biotemplate	Fiber length [nm]	height [nm]	Growth rate [nm/cycle]*
M13-DD	1183 ± 174	62.3 ± 3.1	11.8 ± 0.6
M13-DG	1112 ± 88	63.8 ± 6.19	12.1 ± 1.2
M13 wt	1095 ± 75	64.5 ± 3.8	12.2 ± 0.8

*the height of immobilized M13 phage templates before ZnO deposition is 3-4 nm (determined by AFM on 10 different templates) and was subtracted before calculation of the ZnO growth rate

Table S2 Oligonucleotides for the construction of genetically engineered M13 phage templates. Oligonucleotides were applied for inverse PCR (p8 Nco for/rev and p8 BamHI for/rev) or directly as insert for the N-terminal fusion of aspartic acid residues to the major coat protein (p8-DD and p8-DG). Restriction sites are underlined; codons for additional aspartic acids residues are bold.

Oligo	Sequence	Modificat
p8 NcoI for	5´-TTCCCATGGTGTCTTTCGCTGCTGAGGGTG-3´	*Nco*I
p8 NcoI rev	5´-ACACCATGGGAACGAGGGTAGCAACGGCTA-3´	restriction
p8 BamHI for	5´-TGAGGATCCCGCAAAAGCGGCCTTTAACTC-3´	*Bam*HI
p8 BamHI rev	5´-GCGGGATCCACACCCTCAGCAGCGAAAGAC-3´	restriction
p8-DD-NB-f	5´-TTCCCATGGTGTCTTTCGCTGCT**GATGAC**GAGGGTGAGGATCCCGC-3´	Fusion M1
p8-DD-NB-r	5´-GCGGGATCCTCACCCTC**GTCATC**AGCAGCGAAAGACACCATGGGAA-3´	p8-DD
p8-DG-NB-f	5´-TTCCCATGGTGTCTTTCGCTGCT**GATGGC**GAGGGTGAGGATCCCGC-3´	Fusion M1
p8-DG-NB-r	5´-GCGGGATCCTCACCCTC**GCCATC**AGCAGCGAAAGACACCATGGGAA-3´	p8-DG

Zeta-potential investigation of phage surface charge

Measurements were performed with a ZetaSizer Nano ZS in DTS 1060 Cells at room temperature. The zeta potential was evaluated according to the Smoluchowski equation. Nine measurements with 35 - 100 sub-runs (automatic mode) were performed. The presented values are the average values over all measurements and their standard deviation. The M13 phage concentration was $2.2 \cdot 10^8$ pfu/ml in 10 mM Tris-HCl buffer at pH 8.32 which is close to the pH during the ZnO deposition.[38]

Table S3 Zeta potential measurements of the M13-DD and M13 wt phages in solution.

Biotemplate	Buffer	pH	Zetapotenial [mV]
M13-DD	Tris-HCl	8.32	-45.8 ± 3.2
M13 wt	Tris-HCl	8.32	-42.5 ± 6.9

PFM degree of unipolarity

Based on the relative signal distribution of the in-phase signal, which is the mean distribution over three ZnO/M13 hybrid wires, the degree of unipolarity ξ was calculated.[24] With an ideal unipolar single-domain crystal corresponding to ξ = 1 and an ideally random multi-domain crystal corresponding to ξ = 0. The statistical error was calculated on the degree of unipolarity of individual hybrid wires, describing the differences between individual wires. The statistical error of non-templated ZnO nanocrystallites was not determined, since the particles are nanometer sized harboring only one or two domains, which would result in random scattering of the deviation, in this case the degree of unipolarity is an average over 20 individual particles.

Table S4 Degree of unipolarity *ξ*.

Biotemplate	ξ
M13-DD	0.6 ± 0.1
M13-DG	0.5 ± 0.15
M13 wt	0.4 ± 0.11
Non-templated ZnO	0.1

4.4 Acknowledgements

The authors are grateful to the Nanostructuring Lab Weis (MPI FKF, Stuttgart) for the possibility to use SEM equipment, the Department Spatz (MPI IS, Stuttgart) for access to AFM equipment, the Department Fischer (MPI IS, Stuttgart) for access to Zetasizer equipment and the Chair of Materials Physics (Prof. Schmitz, IMW, University of Stuttgart) for TEM equipment. The authors want to thank Efi Hadjixenophontos (Chair of Materials Physics IMW, University of Stuttgart) for the FIB sample preparation and support during the TEM investigations. Financial support by the Baden-Württemberg (BW) Stiftung and the Deutsche Forschungsgemeinschaft (DFG) is highly appreciated.

4.5 References

[1] C. D. O'Loughlin, C. Gaudin, J. P. Morton, D. J. White, International Journal of Physical Modelling in Geotechnics 2014, 14, 31.

[2] A. Pohl, G. Ostermayer, L. Reindl, F. Seifert, "Monitoring the tire pressure at cars using passive SAW sensors", presented at *1997 IEEE Ultrasonics Symposium Proceedings. An International Symposium (Cat. No.97CH36118)*, 5-8 Oct 1997, 1997.

[3] S. Haeberle, R. Zengerle, Lab on a Chip 2007, 7, 1094.

[4] G. A. Ozin, I. Manners, S. Fournier-Bidoz, A. Arsenault, Advanced Materials 2005, 17, 3011.

[5] C. R. Bowen, H. A. Kim, P. M. Weaver, S. Dunn, Energy & Environmental Science 2014, 7, 25.

[6] S. Trolier-McKinstry, P. Muralt, Journal of Electroceramics 2004, 12, 7.

[7] C. P. Y. Li, B.H., Journal of Electronic Materials 2011, 40, 253.

[8] A. Dal Corso, M. Posternak, R. Resta, A. Baldereschi, Physical Review B 1994, 50, 10715.

[9] A. von Hippel, Zeitschrift für Physik A Hadrons and nuclei 1952, 133, 158.

[10] L. B. Francesca, D. Timothy, D. Anuja, A. W. Richard, S. Suman-Lata, K.-N. Sohini, Nanotechnology 2016, 27, 28LT02; S. Stassi, V. Cauda, C. Ottone, A. Chiodoni, C. F. Pirri, G. Canavese, Nano Energy 2015, 13, 474; C. Ou, P. E. Sanchez-Jimenez, A. Datta, F. L. Boughey, R. A. Whiter, S.-L. Sahonta, S. Kar-Narayan, ACS Applied Materials & Interfaces 2016, 8, 13678.

[11] Z. Burghard, L. Zini, V. Srot, P. Bellina, P. A. van Aken, J. Bill, Nano Lett 2009, 9, 4103.

[12] S. Borg, D. Rothenstein, J. Bill, D. Schüler, Small 2015, 11, 4209.

[13] N. Stitz, S. Eiben, P. Atanasova, N. Domingo, A. Leineweber, Z. Burghard, J. Bill, Scientific reports 2016, 6, 26518.

[14] D. Rothenstein, S. J. Facey, M. Ploss, P. Hans, M. Melcher, V. Srot, P. A. v. Aken, B. Hauer, J. Bill, Bioinspired, Biomimetic and Nanobiomaterials 2013, 2, 173.

[15] Y.-H. Tseng, H.-Y. Lin, M.-H. Liu, Y.-F. Chen, C.-Y. Mou, The Journal of Physical Chemistry C 2009, 113, 18053.

[16] S. Kilper, S. J. Facey, Z. Burghard, B. Hauer, D. Rothenstein, J. Bill, Advanced Functional Materials 2018, 28, 1705842.

[17] W. O. Salivar, H. Tzagoloff, D. Pratt, Virology 1964, 24, 359.

[18] D. A. Marvin, Current Opinion in Structural Biology 1998, 8, 150.

[19] B. Y. Lee, J. Zhang, C. Zueger, W.-J. Chung, S. Y. Yoo, E. Wang, J. Meyer, R. Ramesh, S.-W. Lee, Nature nanotechnology 2012, 7, 351.

[20] S. S. Panda, H. E. Katz, J. D. Tovar, Chemical Society Reviews 2018, 47, 3640.

[21] D.-M. Shin, H. J. Han, W.-G. Kim, E. Kim, C. Kim, S. W. Hong, H. K. Kim, J.-W. Oh, Y.-H. Hwang, Energy & Environmental Science 2015, 8, 3198.

[22] K. Cung, B. J. Han, T. D. Nguyen, S. Mao, Y. W. Yeh, S. Xu, R. R. Naik, G. Poirier, N. Yao, P. K. Purohit, M. C. McAlpine, Nano Lett 2013, 13, 6197; C. K. Jeong, I. Kim, K.-I. Park, M. H. Oh, H. Paik, G.-T. Hwang, K. No, Y. S. Nam, K. J. Lee, ACS Nano 2013, 7, 11016.

[23] J. L. Moreland, A. Gramada, O. V. Buzko, Q. Zhang, P. E. Bourne, BMC Bioinformatics 2005, 6, 21.

[24] D. A. Marvin, R. D. Hale, C. Nave, M. H. Citterich, Journal of Molecular Biology 1994, 235, 260.

[25] N. Korkmaz, Colloids and Surfaces B: Biointerfaces 2013, 112, 219; K. N. Avery, J. E. Schaak, R. E. Schaak, Chemistry of Materials 2009, 21, 2176; F. Baneyx, D. T. Schwartz, Current Opinion in Biotechnology 2007, 18, 312.

[26] P. Lipowsky, N. Hedin, J. Bill, R. C. Hoffmann, A. Ahniyaz, F. Aldinger, L. Bergström, The Journal of Physical Chemistry C 2008, 112, 5373.

[27] M. Grzelczak, J. Vermant, E. M. Furst, L. M. Liz-Marzán, Acs Nano 2010, 4, 3591; Z. Tang, N. A. Kotov, M. Giersig, Science 2002, 297, 237; K.-S. Cho, D. V. Talapin, W. Gaschler, C. B. Murray, Journal of the American Chemical Society 2005, 127, 7140; Z. Liu, X. D. Wen, X. L. Wu, Y. J. Gao, H. T. Chen, J. Zhu, P. K. Chu, Journal of the American Chemical Society 2009, 131, 9405.

[28] A. Rao, H. Cölfen, The Chemical Record 2018, 18, 1203.

[29] R. Viswanatha, S. Sapra, B. Satpati, P. V. Satyam, B. N. Dev, D. D. Sarma, Journal of Materials Chemistry 2004, 14, 661.

[30] I. Bdikin, J. Gracio, R. Ayouchi, R. Schwarz, A. Kholkin, Nanotechnology 2010, 21, 235703.

[31] E. Soergel, Journal of Physics D: Applied Physics 2011, 44, 464003.

[32] V. V. Osipov, D. A. Kiselev, E. Y. Kaptelov, S. V. Senkevich, I. P. Pronin, Physics of the Solid State 2015, 57, 1793.

[33] M. N. Palatnikov, V. A. Sandler, N. V. Sidorov, O. V. Makarova, Inorganic Materials 2016, 52, 147.

[34] M. Laurenti, S. Stassi, M. Lorenzoni, M. Fontana, G. Canavese, V. Cauda, C. F. Pirri, Nanotechnology 2015, 26, 215704.

[35] G. P. Smith, Vol. 2017.

[36] A. L. Kholkin, S. V. Kalinin, A. Roelofs, A. Gruverman, in *Scanning Probe Microscopy: Electrical and Electromechanical Phenomena at the Nanoscale*, (Eds: S. Kalinin, A. Gruverman), Springer New York, New York, NY 2007, 173.

[37] S. V. Kalinin, D. A. Bonnell, Physical Review B 2002, 65, 125408.

[38] N. Stitz, OPUS, Stuttgart 2017.

5 Summary

Functional metal oxides possess material properties such as piezoelectricity, thermoelectricity, electrical conductivity or serve as host material for energy storage. Conventional production processes to obtain such materials are often connected with high energy consumption and require elaborated equipment.

In contrast, nature forms highly structured inorganic materials at ambient synthesis conditions. This so-called biomineralization is controlled by organic molecules, e.g. peptides, which serve as template and inducer / controller of for the formation process. Natural role models such as bone or nacre serve as inspiration for the detailed investigation of organic-inorganic interactions and the fabrication of novel hybrid materials systems. However, technically relevant metal oxides were so far not discovered in living nature, hence, there are no natural peptides controlling the bioinspired synthesis of such materials. Furthermore, for the adaption of the biomineralization process to technical inorganic materials, viruses like the filamentous M13 phage are a particularly interesting group of bio-templates. By genetic modification of the phage genome, specific surface functionalities (amino acid sequences) for the interaction with technical materials, like e.g. zinc oxide (ZnO) or tin oxide (SnO), can be selected.

This work addresses the interface design of M13/ZnO- and M13/SnO-hybrid materials to control the materials structure and properties. Hereby, the M13 phage serve as carrier for different amino acid sequences (peptides). Peptides that specifically interact with a metal oxide surface were selected from a peptide library by phage display technique, in order to identify peptide-based binding motifs. The tin(II) oxide (SnO) binding peptide SnBP01 with the amino acid sequence LPPWKLK was identified and applied for the morphology control in the synthesis of SnO microstructures. The peptide increased the aspect ratio of mineralized SnO platelets accompanied by a change of the morphology from cross-like to flower-like particles.

To integrate effectively such binding peptides into hybrid materials, M13 phages are used as carriers because they possess a highly ordered structure and with e.g. convective assembly a large number of M13 phages can be ordered to form template layers for the deposition of metal oxides. In a layer-by-layer approach convective assembly and chemical bath deposition were combined to form multi-layered thin films based on ZnO and intercalated M13 phage layers. By genetic modification of the phage-template a ZnO binding motif (HSSHH) was

expressed on the template surface. The binding strength of the ZnO binding motif was tuned by the exchange of a single amino acid in the sequence (DSSHH), resulting in an enormous change of the mechanical properties of the hybrid material. The tailoring of the interface by molecular recognition of the inorganic phase allows major improvements and the precise control of specific mechanical properties.

Studies on the physicochemical properties of biological hybrid materials showed, that these materials possess not solely interesting surface properties but also interesting bulk properties such as piezoelectricity. Therefore, the piezoelectric properties of the organic-inorganic hybrids are in the focus of this work. Due to the protein structure of the phage major coat protein p8, the M13 phages possess an intrinsic dipole moment. By addition of negatively charged amino acids (e.g. aspartic acid) to the N-terminus of p8 this intrinsic dipole moment was increased. Hereby, the orientation of the intrinsic dipoles and hence polarization direction of the deposited ZnO nanocrystals was controlled. The overall piezoelectric response of the most effective ZnO nanowire was almost doubled from $d_{33} = 2.6\ \mathrm{pm\ V^{-1}}$ for the non-modified M13 wt phage to $d_{33} = 5.0\ \mathrm{pm\ V^{-1}}$ for the genetically enhanced M13-DD phage.

It could be successfully demonstrated how complex structured and highly functional metal oxide hybrid materials can be synthesized by use of an organic template and bioinspired chemical synthesis methods at ambient conditions. By genetic modification of the organic component, a precise control of the materials structure and properties was achieved. This thesis utilized basic methods and design principles which might be easily adapted for a large number of inorganic materials.

6 Zusammenfassung

Funktionelle Metalloxide zeigen interessante Materialeigenschaften wie beispielsweise Piezoelektrizität, Thermoelektrizität, elektrische Leitfähigkeit oder können als Speichermaterialien in Energiespeichern eingesetzt werden. Konventionelle Produktionsverfahren zur Herstellung solcher Materialien sind oft mit einem hohen Energieverbrauch und großem technischem Aufwand verbunden.

Im Gegensatz dazu stellt die Natur komplexstrukturierte, anorganische Materialien in energiesparenden Niedrigtemperatursynthesen her. Dieser Prozess wird Biomineralisation genannt und durch organische Moleküle, z.B. Peptide, gesteuert, die als Templat, Induktor und zur Kontrolle des Bildungsprozesses dienen.

Natürliche Vorbilder wie Knochen oder Perlmutt dienen als Inspiration für die detaillierte Untersuchung organisch-anorganischer Wechselwirkungen und für die Herstellung neuartiger Hybridmaterialsysteme. Da technisch relevante Metalloxide jedoch bisher nicht in der belebten Natur entdeckt wurden gibt es keine natürlichen Peptide, die die bioinspirierte Synthese solcher Materialien steuern könnte. Viren wie M13 Phagen können als Biotemplate bei der technologischen Umsetzung von Biomineralisationsprozessen helfen. Durch genetische Modifikation des Phagengenoms können spezifische Oberflächenfunktionalitäten (Aminosäuresequenzen) für die Wechselwirkung mit technischen Materialien, wie z. Zinkoxid (ZnO) oder Zinnoxid (SnO) erzeugt werden.

Diese Arbeit befasst sich mit dem Grenzflächendesign von M13 / ZnO- und M13 / SnO-Hybridmaterialien zur Steuerung der Materialstruktur und -eigenschaften. Dabei dienen die M13-Phagen als Träger für verschiedene Aminosäuresequenzen (Peptide). Peptide, die spezifisch mit einer Metalloxidoberfläche in Wechselwirkung treten, wurden aus einer Peptidbibliothek mittels Phagen Display selektiert und bei der Synthese von SnO-Mikrostrukturen zur Kontrolle der Partikelmorphologie verwendet. Durch die Erhöhung des Aspekt-Verhältnis von mineralisierten SnO-Plättchen änderte sich die Morphologie von kreuzähnlichen zu blütenartigen Partikeln

Um identifizierte Bindungspeptide effektiv in Hybridmaterialien zu integrieren, wurden M13-Phagen als Templat verwendet, da diese eine hochgeordnete Struktur besitzen und es möglich ist durch Verfahren wie „Convective Assembly“ eine große Zahl von M13 Phagen auszurichten,

um so Templatschichten für die flächige Abscheidung von Metalloxiden zu bilden. In einem Schicht-für-Schicht Herstellungsprozess wurden „Convective Assembly“ und chemische Badabscheidung kombiniert um geschichtete Dünnfilme auf der Basis von ZnO und interkalierten M13 Phagenschichten synthetisiert. Durch genetische Modifikation des Phagen-Templates wurde ein ZnO-Bindungsmotiv (HSSHH) auf der Templatoberfläche exprimiert. Die Bindungsstärke des ZnO-Bindungsmotivs wurde durch den Austausch einer einzelnen Aminosäure in der Sequenz (DSSHH) modifiziert, was zu einer drastischen Änderung der mechanischen Eigenschaften führte. Die Anpassung der Grenzfläche durch molekulare Erkennung der anorganischen Phase ermöglicht hierbei wesentliche Verbesserungen und die genaue Kontrolle spezifischer mechanischer Eigenschaften.

Studien zu den physikalisch-chemischen Eigenschaften biologischer Hybridmaterialien haben gezeigt, dass diese Materialien nicht nur interessante Oberflächeneigenschaften besitzen, sondern auch Volumeneffekte wie Piezoelektrizität zeigen. Daher stehen außerdem die piezoelektrischen Eigenschaften der organisch-anorganischen Hybridmaterialien im Fokus dieser Arbeit. Aufgrund der Proteinstruktur des Hüllproteins p8 besitzt die M13 Phage ein intrinsisches Dipolmoment. Durch die Expression negativ geladener Aminosäuren (z. B. Asparaginsäure) am N-Terminus des p8 wurde das intrinsische Dipolmoment des Hüllproteins erhöht. Somit konnte die Orientierung der intrinsischen Dipole und damit die Polarisationsrichtung der abgeschiedenen ZnO-Nanokristalle kontrolliert werden. Die piezoelektrische Gesamtantwort der hergestellten ZnO-Nanodrahts wurde von $d_{33} = 2.6\ \mathrm{pm\,V^{-1}}$ für nicht modifizierte M13 wt Phagen auf $d_{33} = 5.0\ \mathrm{pm\,V^{-1}}$ für genetisch modifizierte M13-DD Phagentemplate nahezu verdoppelt.

In dieser Arbeit konnte erfolgreich gezeigt werden, wie komplex strukturierte und hochfunktionelle Metalloxid-Hybridmaterialien unter Verwendung eines organischen Templats und bioinspirierter chemischer Synthesemethoden bei Umgebungsbedingungen synthetisiert werden können. Durch genetische Modifikation der organischen Komponente wurde eine präzise Kontrolle der Materialstruktur und -eigenschaften erreicht. Die verwendeten grundlegenden Methoden und Entwurfsprinzipien können leicht für eine Vielzahl anorganischer Materialien angepasst werden.

7 Danksagung

An dieser Stelle möchte ich mich bei allen bedanken, die mich während meiner Arbeit unterstützt haben.

Zuerst möchte ich mich bei meinem Doktorvater Herrn Prof. Dr. Joachim Bill bedanken dafür, dass er mir die Möglichkeit gab in seiner Gruppe diese Arbeit anzufertigen und für die viele Zeit, Unterstützung und Geduld, die er mir und meiner Arbeit entgegenbrachte. Herrn Prof. Dr. Siegfried Schmauder danke ich für die freundliche Übernahme des Mitberichtes und Herrn Prof. Dr. Peer Fischer danke ich für die Übernahme des Prüfungsvorsitzes sowie dem Zugang zu Messgeräten.

Mein größter Dank geht an Dr. Dirk Rothenstein, der bereits meine Masterarbeit und nun auch meine Dissertation betreut hat. Nur durch seine außerordentliche Unterstützung konnte diese Arbeit zu dem werden, was sie nun ist. Über die Jahre wurde er mir nicht nur zu einem Vorbild, sondern auch zur wichtigen persönlichen Bezugsperson. Ich danke ihm für die tolle gemeinsame Zeit, schöne gemeinsame Konferenzen und Workshops, für unzählige wissenschaftliche Diskussionen, dafür, dass ich immer auf seinen Beistand zählen konnte und nicht zuletzt für alles was ich von ihm gelernt habe.

Darüber hinaus gilt ein besonderer Dank Dr. Žaklina Burghard die mich immer unterstützt hat und auch viel Zeit und Engagement in mich und meine Arbeit investierte. Die gemeinsame Zeit und insbesondere die Konferenz in Belgrad werden mir immer in bester Erinnerung bleiben.

Es ist nicht selbstverständlich, dass man auf Kollegen trifft, die einen durch tolles Teamwork unterstützen und darüber hinaus zu guten Freunden werden, mit denen man gerne auch Zeit außerhalb der Institutswände verbringt. Cora Bubeck danke ich für Hilfe am XRD, tolle Gespräche und dafür, dass sie mich beim Klettern bis jetzt immer sicher aufgefangen hat. Besonders herzlich bedanke ich mich bei Dr. Andrea Knöller, Achim Diem und Timotheus Jahnke für super Teamwork, dafür, dass ich immer auf eure Unterstützung zählen konnte und die schöne Zeit auf Konferenzen und an so einigen Abenden. Letzterem danke ich darüber hinaus, dass er zusammen mit mir das Wagnis eingegangen ist und wir ein spannendes Forschungsprojekt zusammen leiten konnten.

In diesem Zusammenhang danke ich auch Katharina Wiegers, Kevin Hildenbrand, Jonathan Link, Alexandros Georgiadis, Tamara Krauß und Vera Grohe die uns als Hilfswissenschaftlerinnen und Hilfswissenschaftler in diesem Projekt unterstützt haben.

So vielzählig wie die gezeigten Experimente und Methoden ist auch die Zahl an weiteren Kollegen und Kollaborationspartnern, die mich während dieser Arbeit unterstützt haben, wenngleich nicht alle Experimente hier gezeigt wurden. Dr. Marc Widenmeyer danke ich für die Hilfe bei XRD Untersuchungen. Bei Dr. Nina Blumenstein, Dr. Petia Atanasova, Dr. Rahel Eisele und Mirjam Stein bedanke ich mich für die super Zusammenarbeit im Labor, bei Dr. Susanne Ott für die gemeinsame Zeit am AFM und viele tolle Gespräch, bei Sven Fecher für Hilfe bei der Elektronenstrahllithografie und bei Dr. Guilia Santomauro für interessante Diskussionen und wissenschaftliche Einblicke. Dr. Nina Stitz Danke ich für die Unterstützung bei der Bruchzähigkeitsuntersuchung. Prof. Dr. Joachim Spatz, Prof. Dr. Jürgen Weis, Prof. Dr. Eric Mittemeijer, Prof. Dr. Guido Schmitz und Prof. Dr. Metin Sitti bin ich dankbar für Zugang zu Ihren Messgeräten. Ich danke Dr. Ajay Vikram Singh für die Einweisung in FTIR Spektroskopie, Dr. Sandra Facey zusammen mit Jan Klenk and Tina Strobel für die Unterstützung bei der genetischen Modifikation, Dr. Efi Hadjixenophontos für die FIB Probenherstellung, Prof. Dr. Thomas Schimmel zusammen mit Dr. Stefan Walheim und Dr. Gerald Göring für gute Diskussionen, Dr. Lars Jeurgens und Dr. Patrik Schmutz für die Möglichkeit zwei Wochen an der Empa in Dübendorf die KPFM Methode kennenzulernen. Frank Hack, Martin Schweizer, Bernhard Fenk, Ioanis Grigoridis, Peter Engelhardt, Ulrike Waizmann, Marion Hagel, Samir Hammoud, Ivan Kozmon, Maritta Dudek und Traugott Wörner danke ich für Ihre technische Unterstützung und auch darüberhinausgehende Hilfe. Bei Juliane Kränzl und Lukas Fink möchte ich mich für die organisatorische und administrative Unterstützung bedanken.

Das Leben besteht nicht nur aus Arbeit, daher möchte ich meinen Freunden und besonders meinen Eltern danken, dass sich mich in all den Jahren immer unterstützt haben und für mich da waren.